BIOENERGETIC NEUROPROTECTION

IN EXPERIMENTAL GLAUCOMA.

A thesis submitted in fulfilment of the

DEGREE OF MASTER OF PHILOSOPHY

in

The Discipline of Ophthalmology and Visual Sciences

School of Medicine

Faculty of Health Sciences

The University of Adelaide

Chelsea Suzanne Guymer

MBBS, DCH, FRACGP

November 2020

Table of Contents

Achievements

Publications:

Guymer C, Wood J, Chidlow G, Casson R. **Neuroprotection in glaucoma: recent advances and clinical translation.** Clinical and Experimental Ophthalmology. 2019;47(1):88-105.

Guymer C, Damp L, Chidlow G, Wood J, Tang YF, Casson R. **Software for quantifying and batch processing images of Brn3a and RBPMS immunolabelled retinal ganglion cells in retinal wholemounts.** Trans Vis Sci Tech. 2020;9(6):28.

Paper Presentations:

Oral pyruvate supplementation protects against neurodegeneration in a rat model of glaucoma.
Guymer, C; Wood, J; Chidlow, G; Casson, R.
RANZCO Annual Congress 2017 – Perth, WA

Oral pyruvate supplementation protects against neurodegeneration in a rat model of glaucoma.
Guymer, C; Wood, J; Chidlow, G; Casson, R.
ARVO Annual Meeting 2018 – Hawaii, USA

Improve your research productivity whilst on your coffee break: highly accurate fully automated batch processing to quantify retinal ganglion cells in retinal flatmounts.
Guymer, C; Damp, L; Tang, E; Chidlow, G; Wood, J; Casson, R.
RANZCO Annual Congress 2018 – Adelaide, SA

Poster Presentations:
Oral pyruvate supplementation protects against neurodegeneration in a rat model of glaucoma.
Guymer, C; Wood, J; Chidlow, G; Casson, R.
Florey Postgraduate Research Conference 2018 – Adelaide, SA

Highly Accurate, Fully Automated Batch Processing of Retinal Ganglion Cell Counts from Retinal Flatmounts.
Casson, R; Guymer, C; Damp, L; Tang, E; Wood, J; Chidlow, G.
ARVO Annual Meeting 2019 – Vancouver, Canada

Awards:
Best Paper – Gerard Crock Trophy
RANZCO Annual Congress 2017 – Perth, WA

International Travel Grant ($1100 USD)
ARVO Annual Meeting 2018 – Hawaii, USA

Florey Medical Research Foundation Prize ($700)
Adelaide Medical School Prize ($200)
Florey Postgraduate Research Conference 2018 - University of Adelaide, SA

Abstract

Glaucoma refers to a group of ocular conditions united by a clinically characteristic intraocular pressure optic neuropathy and associated degeneration of the retinal ganglion cells (RGCs). It is a leading cause of blindness worldwide. Although the pathogenesis of the most common variant, primary open-angle glaucoma, remains poorly understood, there is considerable evidence that energy insufficiency plays a pathogenic role. Currently, the only proven strategy to treat glaucoma is intraocular pressure (IOP) reduction by medical, laser or surgical modalities. Whilst these IOP lowering therapies have been proven to retard glaucomatous progression, there is inter-individual responsiveness and a significant proportion of individuals progress to visual impairment. Additional neuroprotective strategies that augment IOP-lowering therapy would be highly clinically desirable and likely to reduce the burden of glaucomatous visual impairment at the individual and society levels. This thesis investigates bioenergetic neuroprotection in experimental glaucoma and specifically the effects of pyruvate supplementation in facilitating neuroprotection or recovery of compromised, but not dead, RGCs.

The thesis consists of two related but independent sections. The first section describes a novel automated cell counting program, conceived to facilitate highly accurate automated counts of immunolabelled RGCs on retinal wholemounts. Quantifying RGCs on retinal wholemounts remains one of the key histopathological end points in pre-clinical glaucoma neuroprotection studies, yet manual or semi-automated methods are labour intensive, monotonous, time consuming and subject to inter and intra-observer variability. Limited software is available to expedite counting of immunolabelled RGCs on wholemounts. Their use is restricted due to cost constraints with purchasing licences for commercially available software, limited

applicability to a variety of RGC / neuronal specific immunolabels, inability to distinguish cells in cluster, and heavy manual image pre-processing steps. We have overcome these barriers with our innovative software and validated its use against a variety of RGC specific immunolabels (Brn3a and RBPMS). Our results demonstrate excellent accuracy and a 40-fold reduction in time compared to manual counting. Ultimately this software promises to expedite data acquisition and statistical analysis in pre-clinical glaucoma neuroprotection research, potentially accelerating translation to clinical trials.

The second section demonstrates the highly significant neuroprotective effects of oral pyruvate supplementation in our experimental rat model of glaucoma. Experimental glaucoma was induced unilaterally by laser photocoagulation of the trabecular meshwork and episcleral veins, in control and pyruvate-supplemented rats. At two weeks, the retina and optic nerves were processed for quantification of the number of surviving RGCs and axonal injury, respectively. The combined results clearly demonstrate RGC preservation, decreased axonal loss and degeneration, and attenuated microglial proliferation and phagocytic activity in the retinal nerve fibre layer and optic nerves of pyruvate-supplemented glaucomatous rats. Retinal cell cultures demonstrated that the presence of pyruvate counteracted the loss of both glia and neurons when subjected to either glucose deprivation or oxidative stress, suggesting that pyruvate supplementation has multimodal mechanisms of neuroprotection. These results unveil a potential new therapy for glaucoma with promise of translation into clinical trials.

Declaration

I certify that this work contains no material which has been accepted for the award of any other degree or diploma in my name, in any university or other tertiary institution and, to the best of my knowledge and belief, contains no material previously published or written by another person, except where due reference has been made in the text. In addition, I certify that no part of this work will, in the future, be used in a submission in my name, for any other degree or diploma in any university or other tertiary institution without the prior approval of the University of Adelaide and where applicable, any partner institution responsible for the joint-award of this degree.

I acknowledge that copyright of published works contained within this thesis resides with the copyright holder(s) of those works.

I also give permission for the digital version of my thesis to be made available on the web, via the University's digital research repository, the Library Search and also through web search engines, unless permission has been granted by the University to restrict access for a period of time.

Chelsea Guymer   August 2020

Acknowledgements

I am truly grateful for the wealth of experiences gained throughout this research degree. As a clinician I have gained much insight into understanding the scientific principles that underpin clinical advances in medicine, chartered by the meticulous and diligent work of scientists navigating unexplored territory. I have certainly gained a deeper respect and appreciation for pre-clinical research, without which progress in medicine would be slow, albeit imposing unacceptable risk.

Prof Robert Casson, thank you for providing me with the opportunity to join the Ophthalmic Research Laboratory and undertake this research degree. You have knack of knowing how to motivate and enthuse your students and peers alike, gently probing our inquiring minds and teaching us to enjoy the acquisition of knowledge. Dr John Wood and Dr Glyn Chidlow, thank you for your patience as I grappled with scientific concepts and laboratory skills which pushed me outside my comfort zone after years of experience with clinical medicine. You have instilled in me the value of scientific excellence, attention to detail, research integrity and lateral thinking. I am truly grateful for the opportunity to be guided by your wisdom, which has enabled me to contribute to new frontiers in glaucoma research.

Teresa Mammone and Mark Daymon, thank you for all you have taught me in the laboratory and your invaluable technical assistance. I very much enjoyed your company and good humour, which made the lab more enjoyable.

To my colleague Dr Jack Ao, with whom I rode the rollercoaster of trials and tribulations of our laboratory research experience.

To my husband, Lloyd Damp, who rejoiced in my successes, remained empathetic to my struggles and was the mastermind behind engineering the cell counting software.

To my parents, children, siblings and grandparents, thank you being my lifelong cheerleaders, celebrating my strengths, tolerating my flaws and providing unconditional love and support.

"The more that you read, the more things you will know.

The more that you learn, the more places you'll go…

You're off to great places! Today is your day!

Your mountain is waiting, so get on your way!"

Dr Seuss

Abbreviations

ATP	Adenosine Triphosphate
CoQ10	Coenzyme Q10
GCL	Ganglion Cell Layer
LDH	Lactate Dehydrogenase
IOP	Intraocular Pressure
NAD	Nicotinamide adenine dinucleotide
NAM	Nicotinamide
NMDA	N-methyl-D-aspartate
ON	Optic Nerve
ONH	Optic Nerve Head
OPP	Ocular Perfusion Pressure
OXPHOS	Oxidative Phosphorylation
PACG	Primary Angle Closure Glaucoma
POAG	Primary Open Angle Glaucoma
PPP	Pentose Phosphate Pathway
RGC	Retinal Ganglion Cell
RNFL	Retinal Nerve Fibre Layer
ROS	Reactive Oxygen Species
RT PCR	Real Time Polymerase Chain Reaction
VF	Visual Fields

1. Background and Review of the Literature

1.1. Glaucoma and its significance

Glaucoma is the world's leading cause of irreversible blindness[1,2], currently affecting more than 64 million people worldwide with speculations that this will exponentially increase to 76 million by 2020 and 111 million in 2040[3]. The prevalence of glaucoma is estimated to affect 1.2% to 3% of Australian residents aged 40 and over[4,5] and is expected to rise by at least 80% over the next 20 years with our aging population[1]. Consequently this is expected to increase health system costs over the same period by $AU429 million[1]. Whilst reduction of intraocular pressure (IOP) is the mainstay of therapy for glaucoma, this can prove challenging and is often inadequate as approximately 1 in 6 individuals with primary open-angle glaucoma (POAG) will progress to bilateral blindness within 20 years of being diagnosed despite treatment[6,7]. Apart from significant vision-related disability, glaucoma can also contribute to substantial loss of quality of life[8].

1.1.1. Formal classification of glaucoma

Glaucoma refers to a group of ocular conditions united by a clinically characteristic optic neuropathy and associated degeneration of the retinal ganglion cells (RGCs). It is sometimes, arguably more aptly, referred to in the plural as "the glaucomas" (but in this thesis we refer to the set of conditions as "glaucoma"). Glaucoma can be classified into primary or secondary forms. In primary glaucoma the IOP may either be elevated above statistically normal population levels or may always be recorded within the normal range. Regardless of the IOP, glaucoma is present if the optic nerve manifests the typical clinical features. So-called normal tension glaucoma refers to a type of open-angle glaucoma in which the IOP is never recorded as elevated. There is controversy within the ophthalmic community as to whether this subtype represents a category in its own right or should be conceived as a subtype of POAG.

Conversely, ocular hypertension (OHT) is a clinical entity comprising an elevated IOP in the absence of glaucomatous optic neuropathy. The clinical entity known as "glaucoma suspect" refers to the situation where there are possible features of glaucomatous optic neuropathy, but the evidence is insufficient for the clinician to commit to a diagnosis of definite glaucoma. In secondary glaucoma, the IOP is always elevated at some point in the disease process due to a variety of pathological processes and is presumably responsible for the RGC degeneration and associated glaucomatous optic neuropathy.

An additional, clinically important classification divides glaucoma into open-angle or closed-angle subtypes[9]. The most common subtype of glaucoma is primary open-angle glaucoma (POAG). As the name suggests, the angle in POAG is gonoscopically normal, but there is resistance to aqueous humour drainage at or beyond the trabecular meshwork[10]. In primary angle-closure glaucoma (PACG) there is irido-trabecular contact that may be appositional or synechial with acute, intermittent or chronic IOP elevation. Primary congenital glaucoma is an inherited congenital anomaly of the trabecular meshwork and anterior chamber angle which leads to obstruction of aqueous outflow, increased IOP, and optic nerve damage[11].

1.1.2. Clinical and histopathological features

Glaucomatous RGC loss is associated with characteristic visual field (VF) defects, including nasal steps progressing to an accurate scotoma, typically associated with excavation ('cupping') of the optic nerve head[12]. Glaucoma is associated with elevated IOP in approximately 60-70% of cases[13]. Elevated IOP is a leading risk factor for progression of glaucomatous optic nerve damage; however, there is considerable inter-individual variation in vulnerability to IOP-related damage[14].

Histologically glaucoma is characterised by RGC loss, including degeneration of their somata, dendrites, and axons (the nerve fibres of the optic nerve). This neuronal compartment degeneration is also accompanied by typical excavation of the optic nerve head (ONH), with compression and remodelling of the connective tissue at the ONH[15]. Clinical and histopathological evidence together indicate that the primary site of pathology in glaucoma is the ONH [16–18]. Hence, glaucoma is primarily an axonopathy, with subsequent Wallerian degradation of the distal axon and retrograde loss of RGC somata and dendrites in the RGC layer[18–20]. Therefore, RGC preservation remains fundamental to circumventing visual loss in glaucoma.

1.2. Current treatment of glaucoma, limitations and recent advances

Lowering of IOP ("baroprotection") with medical, laser, or surgical modalities remains the only proven treatment strategy for glaucoma. There are a number of classes of topical pharmacological agents that are used therapeutically for lowering IOP in glaucoma, including cholinergic agents, prostaglandin F receptor analogues, beta-adrenergic receptor blockers, carbonic anhydrase inhibitors, alpha agonists, and rho-kinase inhibitors[2]. Yet their side effects, inconvenience, expense, and discipline required for use markedly affect compliance and adherence. Selective laser trabeculoplasty is a form of laser treatment that increases outflow facility[21]. Although understanding its mechanism of action has received relatively little attention, it is clinically remarkably safe and has recent robust evidence favouring its use over medication as a first line therapy for open-angle glaucoma[22,23]. Surgical intervention has traditionally been reserved for patients who are progressing despite medical and/or laser therapy; however, evidence suggests that early surgery may be a preferable option for patients presenting with advanced disease[24]. In addition the recent emergence of micro-invasive glaucoma surgery (MIGS) is revolutionizing the surgical management of glaucoma[25].

Regardless of the type of intervention, a series of randomised clinical trials (Collaborative Normal Tension Glaucoma Study (CNTGS), Ocular Hypertension Study (OHTS), Early Manifest Glaucoma Trail (EMGT)) have demonstrated that lowering of IOP delays glaucomatous optic nerve damage and visual field loss in patients with advanced glaucoma, raised intraocular pressure, and normal tension glaucoma(26–30). Yet despite adequately achieving IOP lowering, some patients still deteriorate with progressive glaucomatous disc changes and / or visual field loss(26).

1.3. Neuroprotection

In the broadest sense, neuroprotection refers to the relative preservation of neuronal structure and/or function(31). For a chronic neurodegenerative disease such as POAG, neuroprotection is conceptualized as a reduction in the rate of neurodegeneration. Lowering of IOP essentially acts to remove a stressor for glaucomatous neuropathy, rather than making neurons more resilient to stress, and is arguably a form of neuroprotection. In fact, it is currently the only clinically proven strategy for successful neuroprotection. However, it is more common to consider IOP reduction as a distinct strategy with the notion of neuroprotection referring to a non-IOP related treatment modality that effectively reduces the rate of glaucomatous neurodegeneration independent of the IOP.

Whilst the pathogenesis of glaucoma remains incompletely understood, a spectrum of possible mechanisms to explain RGC pathology have been proposed, including genetic determinants, trophic factor withdrawal and loss of electrical activity, defective axon transport, chronic intermittent ischaemia, metabolic / bioenergetic failure, exposure to reactive oxygen species, and excitotoxicity(26,32,33). Laboratory studies continue to advance our understanding of these underlying pathogenic contributors in glaucoma, which ultimately pave the way to the

development of improved neuroprotective strategies and subsequent clinical translation (Figure 1).

Therefore neuroprotection, the ability to augment the survival of RGCs and their axons in the face of neurodegenerative disease(31), is receiving considerable attention as a viable therapeutic strategy to combat progressive blindness in glaucoma.
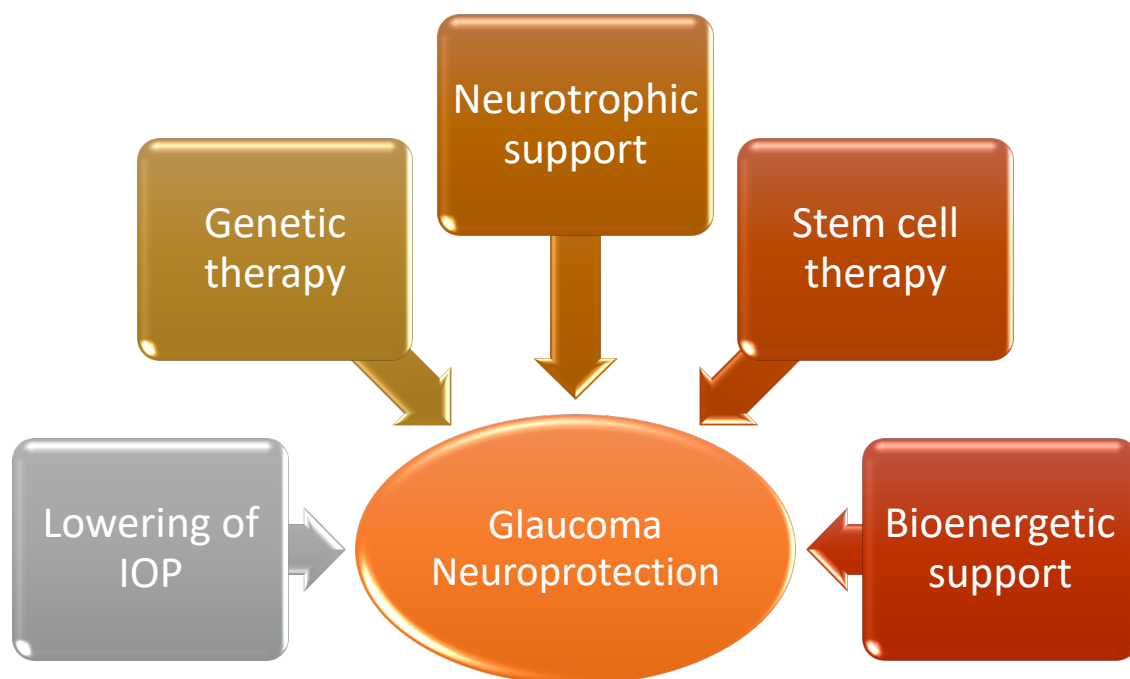
Figure 1. Neuroprotective Strategies in Glaucoma

1.3.1. Possible neuroprotection from existing drugs

1.3.1.1. β-adrenergic antagonist, Betaxolol

Betaxolol, a β-1 adrenoceptor antagonist, is used for the treatment of glaucoma. Whilst primarily acting to lower IOP, betaxolol also exerts neuroprotective actions in the paradigms of ischaemia / excitotoxicity(34–36). This neuroprotective effect is thought to be elicited by its ability to reduce the influx of sodium and calcium through voltage-sensitive calcium and sodium channels(34,37,38). The non-selective β-adrenoceptor antagonists, metipranolol and

timolol, have been shown to behave similarly, yet with reduced neuroprotective efficacy compared with betaxolol(37). Clinically it has been observed that the treatment effect on visual fields of glaucoma patients treated with betaxolol is superior to those treated with timolol(39–42). This is despite the fact that timolol is known to reduce the IOP more effectively than betaxolol in humans(43), supporting that betaxolol must exert a greater non-IOP dependent neuroprotective role.

1.3.1.2. Calcium channel blockers

The use of calcium channel blockers (CCB) as a potential therapy for glaucoma remains controversial. Whilst animal studies have indicated that topical CCB application caused significant IOP reductions, in humans the ocular hypotensive effects were not substantial(44). The CCBs, iganidipine, nimodipine and lomerizine, have demonstrated *in vitro* direct neuroprotective effect against RGC damage related to hypoxia(45). *In vivo* retinal ischaemia / ischaemia-reperfusion models have demonstrated favourable outcomes of CCBs morphologically on the inner retinal layers (including RGCs) and functionally evaluated via electroretinogram(46–50). The neuroprotective effect of CCBs is thought not only to be from vasodilation and restoration of impaired blood low in the local ischaemic tissue, but also via its antioxidant effect and inhibition of calcium influx on neurons undergoing apoptotic and necrotic processes(44). Several single-centered hospital-based prospective studies have demonstrated beneficial effects on visual function in patients with POAG, but these findings were not supported by population-based and case-controlled studies(44,51–56).

1.3.1.3. Angiotensin II type 1 receptor (AT1-R) antagonists, Olmesartan, Candesartan and Irbesartan®

AT1-R antagonists are widely used for the management of systemic hypertension, with well-established safety and side effect profiles, yet only recently has their use been extrapolated as a potential therapy in glaucoma. White *et al.* (2015) demonstrated the neuroprotective effect of Irbesartan in an *ex vivo* retinal explant model, with doubling of retinal ganglion survival after four days and reduced modulation of intracellular generation of free radical formation[57]. In a mouse model of normal tension glaucoma (EAAC1 KO mice), candesartan prevented progressive RGC loss, thinning of the inner retinal layer and visual disturbances without affecting IOP[58]. Likewise, Yang *et al.*(2009) found that continuous treatment using Candesartan resulted in significant neuroprotection against RGC loss and that AT1-R up-regulation was associated with chronic elevation of IOP in a rat model of glaucoma[59]. In a monkey model of unilateral laser-induced glaucoma, topical application of AT1-R antagonist CS-088 reduced IOP in a dose-dependent manner[60]. This suggests that the use of AT1-R antagonists in glaucoma may have both a neuroprotective effect on RGC survival whilst synergistically reducing IOP.

1.3.1.4 Brimonidine

Brimonidine, an α2-adrenergic receptor agonist, is commonly used to lower IOP in glaucoma and is Food and Drug Administration (FDA) approved for systemic administration. It has been demonstrated to protect RGCs in animal models of optic nerve damage independent of its effect on IOP by up-regulating anti-apoptotic factors and by blocking cellular toxicity induced by mitochondrial oxidative stress[2,8,14,16,107,108]. This is thought to be achieved through the modulation of glutamate-induced excitotoxicity, vascular regulation via inhibition of nitric

oxide synthase or the endothelin pathway, oxidative stress, and inhibition of glial activity(62). It has been demonstrated in clinical trials that brimonidine monotherapy lowered the incidence of visual field progression compared with timolol in treated patients (9 vs 30%) in the Low Pressure Glaucoma Study Group over a period of 30 months despite similar IOP lowering effects(2,26,62,63). Yet this study was limited by its small sample size and considerable dropout rate in the brimonidine group(2,63). Topical brimonidine 0.2% applied over 3 months has also been found to improve contrast sensitivity, in comparison to no improvement with timolol therapy, despite similar IOP lowering effects(64). A meta-analysis comparing timolol to brimonidine also confirmed no significant difference in IOP lowering effect(65). Tsai *et al.*(2005) described a statistically significant reduction in retinal nerve fibre layer damage following the use of brimonidine 0.2% compared with timolol 0.5% in ocular hypertensive patients over one year, independent of IOP reduction(66). These results suggest that brimonidine provides a non-IOP related neuroprotective effect.

1.3.1.5 The failure of memantine and lessons learned

Memantine is a non-competitive NMDA receptor antagonist which blocks glutamate excitotoxicity and is commonly used in the treatment of moderate to severe Alzheimer's disease(67). Several animal glaucoma models have shown that memantine is protective against RGC loss, independent to changes in IOP(67,68). Whilst these results suggest that memantine may provide a safe and effective treatment for reduction of any NMDA-type glutamatergic contribution to glaucomatous injury of RGCs, glaucoma remains a complex and multifactorial disease of which glutamate excitotoxicity may only play a small, yet important, part. It could be hypothesised that memantine, when used in conjunction with IOP lowering, could provide synergistic benefit in glaucoma neuroprotection.

Unfortunately, animal models do not perfectly recapitulate human disease thereby making translation to clinical trials difficult. Large-scale multicentre, randomised double-masked placebo-controlled Phase III clinical trials conducted to test the efficacy of oral memantine for glaucoma failed to show any statistical benefit compared to placebo in reducing visual field progression(69). This was particularly disappointing given this trial took over 5 years and cost approximately $100 million USD to complete(62). The primary endpoint in this trial was visual field progression and there are of course inherent challenges in achieving reproducible visual fields, which requires multiple tests over a long follow up period. This highlighted the need for better clinical trial design in glaucoma neuroprotection trials, perhaps aided by more judicious patient recruitment (such as selecting 'rapid progressors' or patients progressing at a pre-defined rate prior to trial entry), more frequent sampling of outcome measures, and, clustering of measurements at the beginning and end of studies to expedite the attainment of relevant trial endpoints, reduce the required sample size and shorten the duration of clinical trials (as was demonstrated in the UK Glaucoma Treatment Study(UKGTS)(27)).

1.3.2. Bioenergetic Neuroprotection

Bioenergetic neuroprotection refers to supporting the neuronal energy requirements at a cellular level, which includes protecting cells against downstream metabolic failure to circumvent apoptosis, which causes consequent neurodegeneration. This approach is gaining momentum in pre-clinical glaucoma research with promising therapeutic translation on the horizon and is the focus of this thesis. This is discussed in greater detail in section '1.8 Targeting Energy Metabolism'.

1.4. Animal models of glaucoma

A large number of models for glaucoma research have been developed over a number of decades to mimic the characteristic pattern of RGC soma and axonal degeneration seen in human glaucoma (70–72). *In vitro* models include immortalised RGC lines, primary RGCs cultures and more recently RGCs developed from induced pluripotent stem cells. Primate models in the 1970s and 80s have largely been replaced by inherited (transgenic) and induced (non-transgenic) rodent models(72,73). Almost all models focus on elevation of the IOP with a plethora of techniques utilized to increase resistance of aqueous outflow or increase episcleral venous pressure. Other models of optic nerve injury (including optic nerve crush and transection) have been used in glaucoma-related research, as have models of acute elevation of the IOP. An ideal animal model should be easy to maintain in a laboratory environment, exhibit a predictable onset and clinical course, and the pathology should have a reasonably long time course to mimic that in the human eye. Whilst these animal glaucoma models enable investigation of pathogenic mechanisms or testing of novel therapeutics in glaucoma, unfortunately no single model emulates all aspects of human glaucoma and these models are not without their limitations(71).

1.4.1. Transgenic Glaucoma Models

Genetic mouse models are more popular than rat strains, as they are inexpensive to breed, have one of the best characterized mammalian genomes and are amenable to conducting complex genetic manipulations(74). Genetic mouse glaucoma models can be generated by specific manipulation of distinct gene loci (such as mutated myocilin gene and overexpression of an adrenomedullin-receptor in the pupillary sphincter)(75–77) or have spontaneous IOP elevation secondary to pigment dispersion (such as DBA/2J, DBA/2Nnia, AKXD-28/Ty strains)(78–80). The DBA/2J mouse model is frequently used and well characterised. Transgenic mice models

generally are able to produce an acceptable degree of RGC loss and axonal degeneration of the optic nerve yet tend not to develop these changes until approximately 8 months of age(71). Apart from needing to age animals and using experiments over longer time frames (i.e. 12 to 18 months), these mice exhibit a high degree of individual variability and asymmetry in the disease development(71). Introducing the genetic mutations can also be a lengthy and difficult process(71).

1.4.2. Non-transgenic Glaucoma Models

1.4.2.1. IOP dependent models

Acute Models

Cannulation of the anterior chamber with infusion of the intraocular space with saline causes an acute rise in IOP which can be sustained for variable time periods (typically 60 to 120 minutes)(81,82). This type of injury causes a transient ischaemia of the inner retinal layers with RGCs consequently undergoing ischaemia-mediated apoptosis(83). The proportion of RGC loss in this model is proportional to the duration of ischaemia and the length of reperfusion survival period, with a substantial portion of RGCs undergoing delayed death following the ischaemic insult(82). One of the issues with this model is that other non-RGC retinal neurons are also affected by complete transient ischemia of the retina(84,85), which may contribute to transneuronal degeneration of RGCs(82).

Subacute/chronic Models

Translimbal laser photocoagulation to the trabecular meshwork in rats can induce IOP elevation for at least 3 weeks, with consequent RGC and axonal loss reported up to 9 weeks(86). This model essentially blocks the aqueous outflow at the trabecular meshwork, thereby increasing IOP and triggering preferential RGC loss. Pressures tend to peak up to 49.0

+/- 6.1 mm Hg, with a mean IOP after 6 weeks of 25.5 +/- 2.9 mm Hg in glaucomatous eyes(86). This results in RGC loss of 33% at 3 weeks and up to almost 60% at 6 weeks(86,87). The significant damage is confined to the RGC layer, nerve fiber layer, and optic nerve axons and therefore serves as a relatively simple, inexpensive and reproducible model of experimental glaucoma. This model is generally only used in non-pigmented animals. Unfortunately this model can be complicated by anterior segment inflammation, corneal opacification preventing a clear view of the posterior segment (up to 20%), and hyphema (up to 40% depending on the technique used, most of which resolved within 48 hours)(86). Another difficulty lies in the absence of a repeatable internal control and large inter-animal variability in terms of IOP profiles and RGC / axonal injury(70,71,86). Similar techniques have been successfully validated in mouse models(88–90).

The occlusion of Schlemm's canal by the injection of either autologous red blood cells or microbeads into the anterior chamber can achieve short term IOP elevation and consequent RGC / axonal loss. IOP can remain elevated up to 4 weeks following a single injection(91,92). Injections can be repeatedly performed for studies of longer duration, to ensure satisfactory IOP elevation. Chen *et al.* (2011) demonstrated approximately 50% reduction in RGC bodies and axons at 8 weeks(91,92). Challenges may arise whereby microbeads can be difficult to retain in the anterior chamber, which can be overcome by the use of paramagnetic microbeads, which can be directed to the iridocorneal angle using a handheld magnet(93). IOP elevation is demonstrated to be highly consistent using the microbead model, both in duration and magnitude, with inter-animal variability of approximately 5% of the mean(71). This makes it an attractive model for the assessment of IOP-induced pathology.

Episcleral vein injection of hypertonic saline in rats causes sclerosis of the trabecular meshwork, thus obstructing the flow of acqueous humour. This model can induce an extended period of ocular hypertension in rodents of up to 200 days(94,95). RGC loss and optic nerve degeneration have been shown to correlate with IOP(96). However, a major challenge with this model is the magnitude of variation in IOP response between animals and sometimes repeat injections are required if an inadequate IOP response occurs(71). It is also technically challenging to perform, requiring a considerable degree of expertise(70,71).

A novel circumlimbal suture model has recently been developed by Lui *et al.* (2015), which, following an initially IOP spike, demonstrates promise with moderate IOP elevation sustained for up to 15 weeks(97). RGC dysfunction evident on electroretinogram was associated with retinal nerve fiber layer thinning and cell loss in the ganglion cell layer(97). This model reportedly substantially limits intraocular inflammation, is reversible, and cost effective(97). This model can be quite technically challenging requiring a degree of microsurgical expertise. However, in our hands, reproducible sustained IOP elevation and resultant RGC death with this model was not achieved.

1.4.2.2. Non-IOP Dependent Models

Optic nerve crush and axotomy models induce retrograde RGC death via Wallerian degeneration and can mimic at least some of the features of glaucoma(98). In the rat model of optic nerve axotomy, after a 5 day lag period, there is abrupt progressive RGC death of up to 50% of normal by day 7 and to less than 10% survival by day 14(99). In comparison, the mouse crush model detailed by Levkovitch-Verbin *et al.* (2000) death of RGCs occurred more gradually with a reduction in RGC population to 47% by day 7 post injury and 27% at 2 weeks(100). The delay in and magnitude of RGC death is greater with cut rather than crush of

the optic nerve(99). Acute alterations in cellular homeostasis, excitotoxicity, the local production of free radicals, and a loss of trophic support all contribute to neurodegeneration and RGC death in this model(99). Crush injury may additionally cause nerve ischaemia(101). These procedures are relatively rapid and simple to perform, highly reproducible and can be particularly useful for studies examining neuroprotection from the secondary degeneration of spared fibres or regeneration of partially damaged ON fibres(100,101).

Whilst some controversy exists, excitotoxicity has been proposed to contribute to RGC death in glaucoma(102). NMDA-induced excitotoxicity is a well-established method of induced RGC apoptosis in a dose-dependent fashion in animal models(103). Intravitreal injections of excitatory amino acids (e.g. glutamate or aspartate) or their analogues (e.g. N-Methyl-D aspartate (NMDA) or 2-amino-3-(5-methyl-3-oxo-1,2- oxazol-4-yl)propanoic acid (AMPA)) in rodents can induce degeneration of the inner retinal layers at low dose(103,104). Whilst relatively easy to perform, one major drawback is that excitotoxicity models only mimic one pathogenic aspect of glaucoma. Despite being widely used in neuroprotection experiments, these models do not necessarily reflect the human disease and could thereby limit clinical translation.

1.4.3. Limitations of Glaucoma Models in Neuroprotection Research

All the glaucoma models have strengths and limitations. Cell culture systems provide an opportunity to rapidly assess potential neuroprotectant agents and investigate mechanisms but are severely limited in their ability to represent the human condition. The primate models with laser induced IOP elevation were perhaps the most realistic of all glaucoma models but ethical considerations and costs have limited their use. The most common genetic rodent model, the DBA/2J mouse has the advantage that large numbers can be utilized but suffers from a variety

of non-glaucomatous pathology(105). The induced rodent models vary in their reproducibility and degree of variance in the RGC injury produced.

The serious limitations of glaucoma models and uncertain relevance to human glaucoma suggest that an optimal strategy in glaucoma neuroprotection research may be to target relatively safe neuroprotectants that can rapidly progress to human trials, avoiding extensive and possibly fruitless animal research.

1.4.4. General approach to quantifying RGC loss/survival in animal models of glaucoma

To assess the damage induced and / or the effectiveness of a therapeutic intervention in animal glaucoma models, RGCs must be both reliably identified and quantified. Typically, RGCs are identified by means of immunohistochemistry staining with RGC-specific (e.g. Brn3a, RNA-binding protein with multiple splicing (RBPMS), gamma synuclein) or neuronal (e.g. NeuN, Neurotrace, or β_3-tubulin) markers(91,106–111). Generally reserved for *in vivo* imaging (with the exception of fluorogold which is commonly also used for RGC detection on wholemounts), fluorescently labelled RGC techniques include the injection of retrograde tracers (e.g. fluorogold) into the superior colliculus, lateral geniculate body, or optic nerve, or intravitreal injection of viral vectors (e.g. adeno-associated viral (AAV) vectors) or annexin 5 (used to detect cells undergoing apoptosis)(112,113).

Fluorogold (FG) specifically and accurately labels RGCs in healthy retina, yet also labels microglia that have phagocytosed dying RGCs(114–116). It has also been suggested that axonal transport of retrograde labels can be slowed by retinal disease processes or elevated IOP, thereby tending to underestimate RGC counts(117). FG is technically challenging and more invasive given that it is performed in vivo by injection into the superior colliculus, which

can limit its use(91,106,117). Neuronal markers NeuN and β_3-tubulin can be used as a marker of RGCs, but have a tendency to stain displaced amacrine cells and can overrepresent RGC counts unless appropriate corrections are made(91,106,118). Whilst Brn3a exclusively stains RGC (with the exception of a small subpopulation of photosensitive RGCs) it is down regulated prior to RGC death and can thus underrepresent counts in diseased retina(107,108,119,120). RBPMS has been characterised as a reliable and specific RGC marker(109,110), yet expression can be affected in a minority of RGC (<4%) by the nature of injury(110). Gamma synuclein is a protein highly expressed in cytoplasm of RGCs, adjacent to the RGC-specific nuclear marker Brn3a, and quite fittingly demonstrates coincident expression with Brn3a(111). Axons of RGCs have also been found to be immunopositive for gamma synuclein, although this appears to vary between disease processes(111). Given this, quantifying RGC counts in retinal wholemounts can be technically challenging with highlighted axon fibres obscuring underlying RGCs. Studies have demonstrated equivalent labelling of RGCs stained by FG with Brn3a, RBPMS, NeuN and β_3-tubulin(91,106–108,110).

RGC loss is typically evaluated with histological section of the retina, retinal wholemounts, or nerve fiber counting in optic nerve cross sections(121–126). These methods can provide spatial information on the distribution of damage but tend to underestimate the degree of neuronal injury(112). Usually pre-defined retinal sectoral regions or optic nerve slices are examined, as analysing the entire retina or optic nerve would be too arduous using these methods. As such, estimated rather than true RGC counts are obtained which can permit sampling bias(107). These techniques are also limited to providing a static measure of RGC populations, at the time of animal death. Counting of RGC or axons following tissue processing and sectioning is invariable performed by manual or semi-automated techniques, which are time-consuming and prone to inter and intra-observer variability. Thus, there has been increasing interest in

developing automated scripts to accurately quantify RGCs(108,117,119,121,127,128), particularly in retinal wholemounts, to expedite data acquisition and statistical analysis.

Molecular analysis quantifying mRNA by use of real-time polymerase chain reaction (RT-PCR) of RGC-specific markers (e.g. Thy-1 and neurofilament) can provide accurate and complimentary measurements of RGC injury and death(129–133). Flow cytometry can also be used to quantify fluorogold-labelled RGCs in the entire retina(134). Whilst these methods do not provide information on spatial distribution of RGC damage in the retina, they can provide a semiquantitative measure of RGC loss/survival in the whole retina(129,134).

Technological advances in *in vivo* imaging can permit real-time non-invasive detection of RGCs with longitudinal analysis if performed at repeated intervals. *In vivo* imaging also has the advantage of providing information about the distribution of any sectoral retinal damage, rate of RGC loss and can progressively measure the response to any treatment. As RGCs are transparent, RGC fluorescent labelling techniques are first employed so that RGCs can be detected with *in vivo* imaging. *In vivo* imaging techniques include confocal laser scanning microscopy, fluorescent microscopy, or confocal scanning laser ophthalmoscopy(112,113,135). Optical coherence tomography (OCT) can provide a cross sectional view of the retina to enable the RNFL to be measured, however studies have demonstrated RGC loss tends to precede thinning of the RNFL and so this may be a late sign(136). Elastic light backscattering spectroscopy can also be employed to detect ultrastructural neuronal damage in RGCs, which can be evident prior to anatomical alterations in the nerve fiber and ganglion cell layers(137). *In vivo* imaging has the potential to expedite the research of neurodegenerative diseases and neuroprotective treatments with repeated sampling in real-time(112).

1.5. Pathogenic mechanisms of RGC injury in glaucoma

Glaucoma has a complex and multifactorial pathogenesis, and despite many decades of research the exact mechanisms have not been clearly elucidated. Traditional hypotheses about pathogenesis are broadly categorised into vascular (i.e. axonal ischaemia) and mechanical theories (i.e. physical compression of axons caused by deformations of the lamina cribrosa), which drives progressive optic neurodegeneration and consequent blindness(138,139). Another proposed contributor is spontaneous compression mediated by tissue pressure differences through the uncompromised lamina cribrosa(139). However, these mechanisms are intimately interconnected, and it is likely that individual susceptibility to glaucomatous insults exist. This is clinically apparent as glaucoma can manifest even with normal pressures, those with elevated IOP may never develop glaucomatous optic neuropathy, and those with ocular hypertension may still progress despite optimal treatment with pressure lowering therapies(140).

1.5.1. Vascular theory

The vascular theory proposes that a compromised blood supply contributes to glaucomatous optic neuropathy. This may be due to insufficient perfusion from increased IOP or other pathologic changes such as alterations in choroidal blood flow, failure of regulation of blood flow or the delivery of injurious vasoactive substances to the blood vessels of the optic nerve(141). This is hypothesized to be a driving pathology in normal pressure glaucoma, where lowering the IOP in these patients can still help to reduce the risk of optic nerve damage and visual field loss(29).

The blood supply of the ONH is primarily derived from the choroid, with the inner (RNFL) and outermost (retrolaminar) regions also receiving input from retinal arteries(142). The

relative contributions of each source is debatable with likely significant inter-individual variation(141). The choroidal circulation is a relatively high flow, low pressure system whereby blood flow diminishes as IOP is elevated and has little or no auto-regulation(141). Particularly in the region of the lamina cribrosa, the optic nerve head can be a watershed area as anastomoses between the posterior ciliary arteries (PCAs) are scant, and can consequently contribute to ischaemia of the ONH(141,142). This may, in part, explain why the lamina cribrosa is the putative site of RGC axonal injury in glaucoma.

Ocular perfusion pressure (OPP) is the difference between arterial and venous blood pressure in the eye. Since the venous pressure almost equals IOP, OPP can be thought of as the difference between arterial pressure and IOP(143). A delicate balance between these two pressure differentials is required to ensure adequate perfusion to the retina. This is achieved through autoregulation – the ability of the vascular bed to maintain its blood flow despite changes in OPP and varied metabolic demand(143,144). Whilst the mechanisms of autoregulation are incompletely understood, autoregulation in the retina and ONH appear to be dependent on myogenic, neurogenic, metabolic mechanisms and sudden changes in OPP(143,144). Studies have demonstrated abnormal autoregulation of ocular blood flow in glaucoma(145–148). Abnormal autoregulation in glaucoma can arise from vascular endothelial dysfunction(149,150) or perhaps activation of astrocytes(151,152).

It is well known that microvascular diseases such as diabetes, hypertension, and migraine headaches, are associated with an increased prevalence of glaucoma(141,153–155). More recently it has been demonstrated through magnetic resonance imaging (MRI) that glaucoma is strongly associated with biomarkers of cerebral small vessel disease(156). It has thus been postulated that systemic microvascular abnormalities increase the susceptibility of the optic

nerve to damage. Excitotoxic damage from glutamate and related excitatory amino acids, secondary to ischaemia, can further perpetuate injury to the optic nerve(141,157).

1.5.2. Mechanical theory

The lamina cribrosa, situated in the posterior sclera and supporting up to 1.5 million RGC axons at the ONH, helps to preserve a pressure gradient between the intraocular and extraocular spaces in glaucoma(158). It is thought that RGC axon integrity at this site can be compromised by either mechanical compression or indirectly from impaired nutritional support from glial cells and supporting vasculature(159). Structural differences in the lamina cribrosa and inter-individual variation in the blood supply to the ONH may also explain individual susceptibility to IOP-mediated damage, and the difference in rates of progression between individuals with glaucoma(159,160).

In response to raised IOP, the configuration of the lamina cribrosa has been shown to change. In human subjects there is posterior displacement and bowing of the lamina cribrosa in response to IOP changes(161,162). Park *et al.*(2011) observed this finding *in vivo* using OCT and found that the regions of laminar deformation showed good spatial correlation to regions of RNFL and visual field defects(162). This deformation of the lamina cribrosa can cause thinning, which becomes more pronounced as the disease progresses(163). This results in a steeper pressure gradient between the cerebrospinal fluid pressure and IOP (i.e. the trans-laminar pressure gradient)(17,164–166), which may in turn increase the susceptibility of optic nerve fibres to mechanical injury. This may in part explain why eyes with advanced glaucoma have a higher risk for progression than eyes at a moderate stage of glaucoma(167).

IOP-mediated connective tissue remodelling of the lamina cribrosa and peripapillary sclera has been demonstrated in experimental primate glaucoma models(168,169). It is hypothesised that laminar remodelling represents a biomechanical feedback mechanism, through which cells modify their environment in an attempt to achieve mechanical homeostasis(170). It is plausible that this biomechanics-driven connective tissue remodelling at the lamina cribrosa and peripapillary sclera is the mechanism by which the ONH forms a cupped, excavated appearance in glaucoma(170).

Numerous studies have also demonstrated that lamina pore area is significantly larger in glaucomatous subjects than in normal subjects(171–174). Further to this Radius *et al.*(1981) demonstrated regional anatomical variations of the lamina cribrosa pores in a morphological study of human optic nerve cross sections, with larger pores located in the superior and inferior parts of the lamina cribrosa(175). Mechanical deformation and tissue remodelling may contribute to laminar pore dimensions in glaucomatous eyes(159). Larger pore size has been hypothesised to cause inherent structural weakness in the connective tissue of the lamina cribrosa, rendering these regions more susceptible to mechanical stress and deformation(158,176). These microarchitectural changes of the lamina cribrosa can explain the specific patterns of visual field loss and neuronal rim changes in human glaucoma(164).

1.6. RGC structure and susceptibility to metabolic injury

Converging evidence has indicated that RGCs are the primary site of energy failure resulting in glaucomatous neurodegeneration(16,32,61,73,140,177–179). Significant loss of visual function can occur with only minor changes in the number of RGC bodies in the retina(140). RGC bodies are located in the ganglion cell layer (GCL) of the inner retina with their axonal projections comprising the retinal nerve fibre layer (RNFL) (Figure 2). Unmyelinated RGC

axons in the prelaminar region converge at the ONH and pass through the lamina cribrosa to form the optic nerve (ON) (Figure 2). The lamina cribrosa is a well-circumscribed region of the sclera specially organised to provide structural support for the axons as they pass through this connective tissue(180). The optic nerve is myelinated upon exciting the ONH and is formed by over one million RGC axons(32).
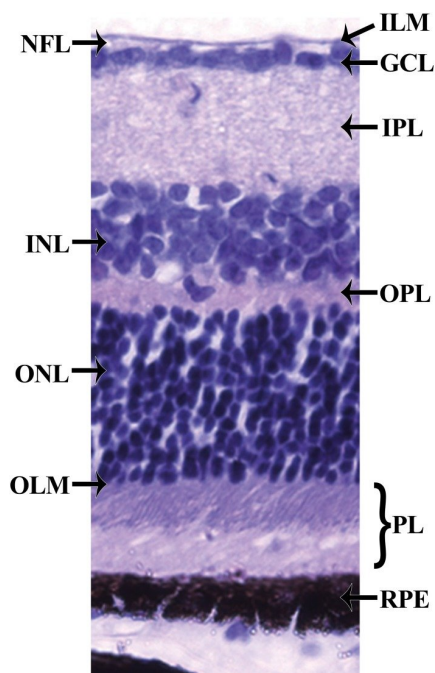
Figure 2. Histology of the retina. The retina can be divided into 10 layers including (1) the inner limiting membrane (ILM); (2) the nerve fiber layer (NFL); (3) the ganglion cell layer (GCL); (4) the inner plexiform layer (IPL); (5) the inner nuclear layer (INL); (6) the outer plexiform layer (OPL); (7) the outer nuclear layer (ONL); (8) the outer limiting membrane (OLM); (9) the photoreceptor layer (PL), and (10) the retinal pigmented epithelium (RPE) monolayer.(181)

The RGC axon has a tremendously long trajectory relative to the size of the cell body, upon which neuronal shuttling of cellular cargo occurs, ultimately compounding the energy demands placed upon RGCs(32). Emerging evidence has strongly associated RGC mitochondrial

dysfunction with retinal and optic nerve damage(182). Impaired axonal transport of mitochondria has been linked to RGC death and, given that the unmyelinated axons of RGCs in the pre-laminar RNFL require a higher energy input, this may in part explain their vulnerability to metabolic injury(183,184).

1.6.1. Visual metabolic demands

Visual processing is metabolically expensive, which makes retinal cells exquisitely sensitive to bioenergetic disturbance. The metabolic cost for the processing of sensory information by mammalian photoreceptors has been estimated at 10^6-10^7 adenosine triphosphate (ATP) molecules for graded signals(185). Thus, the process of phototransduction places intense energy demands upon photoreceptors, which derive nutrients and oxygen from the choroidal circulation. Light must pass through the entire thickness of the vertebrate retina to reach the photoreceptors, hence, the retina needs to be as transparent as possible. This means that within the retina the numbers of blood vessels are minimized because these structures are relatively opaque. This optical requirement for relatively limiting vasculature, coupled with the large energy demands of the retina make it particularly vulnerable to insults involving alterations in the available blood supply(186).

1.6.2. RGC bioenergetics

The brain and retina are both dependent upon glucose metabolism to produce ATP, but there are fundamental differences between retinal and cerebral energy metabolism(187). Akin to the brain, much of the energy required for visual functioning is derived from oxidative metabolism coupled to ATP synthesis(61,188). Yet unlike the brain, the isolated mammalian retina also derives a considerable amount of ATP from the conversion of glucose to lactate, even in the presence of oxygen (the Warburg effect)(32,187). The retinal Warburg effect is likely to be

predominately a feature of the photoreceptors rather than the other retinal neurons. This has the advantage that in the absence of oxygen, the mammalian retina has the remarkable ability to maintain most of its ATP requirements via glycolysis (the Pasteur effect)(32,187). However, the precise contribution of both glycolysis and oxidative phosphorylation to energy metabolism in RGCs and their axons remains unclear and is likely to be both species dependent and dependent upon the level of retinal vasculature(32). Our laboratory has recently estimated that the ATP requirement of RGCs to barely maintain visual function in humans exceeds that of mammalian photoreceptors with approximately 4.7×10^8 molecules of ATP required per second(189).

RGC survival and function are highly dependent on energy supply and given the high metabolic demands of the retina, are exquisitely sensitive to homeostatic disruptions such as anoxia or substrate decline(32,61). Visual processes demand high energy supplies and much of the energy is derived from oxidative metabolism coupled to ATP synthesis(61,188). In a classic experiment, Noell concluded that the RGCs were particularly susceptible to hypoxia and were the "weakest link in the chain" of visual perception(190). An increased density of mitochondria and voltage gated sodium channels have been demonstrated in the optic nerve head (the primary site of glaucomatous axonal injury), suggesting higher functional energy requirements to maintain conduction in the unmyelinated axon(191).

POAG lymphoblasts have exhibited a defect in complex-I of the oxidative phosphorylation pathway, with resultant decreased ATP synthesis, which may contribute to the sensitivity of RGCs to stress(192). Elevated hydrostatic pressure in cultured RGCs for 3 days has been shown to induce mitochondrial fission and disruption of the mitochondrial network, with associated

impairment in ATP production(193). These findings may explain why, with additional stresses such as age and elevated IOP, RGCs are susceptible to metabolic failure in glaucoma.

Extending upon previous studies(177,194), Williams *et al.* (2017) recently demonstrated that mitochondrial abnormalities are an early driver of retinal ganglion cell neuronal dysfunction in glaucomatous mice, occurring before detectable degeneration(182). Consequently, mitochondrial bioenergetic failure culminates in the generation of reactive oxygen species, which further augments RGC death and neurotoxicity(61). Clinical studies have also found an association between mitochondrial dysfunction and glaucoma. An increase in mitochondrial DNA mutations and a 20% reduction in mitochondrial respiratory function were observed in the peripheral blood of POAG patients compared with age matched controls(195). Conversely patients with enhanced mitochondrial function demonstrated resistance to neurodegeneration, whereby they were able to tolerate high IOP for many years without optic nerve degeneration(196). Mitochondrial function in the optic nerve head must then, in at least some patients, play a critical role in the pathogenesis of glaucoma. Congenital or acquired mitochondrial dysfunction may also explain why some patients are more vulnerable to RGC damage than others with glaucoma.

1.7. Consequences of Retinal Energy Failure

1.7.1. Reactive Oxygen Species

As a downstream consequence of mitochondrial bioenergetic failure, oxidative stress has received considerable attention related to its contribution to RGC injury. Generation of reactive oxygen species (ROS), a series of intracellular by-products derived from mitochondrial respiration, is a process which is usually tightly regulated under normal physiological conditions. The antioxidant response is typically carried out by enzymes such as superoxide

dismutase, catalase, glutathione peroxidase, thioredoxin, peroxiredoxin as well as non-enzymatic compounds such as retinol and carotenoids (together comprising vitamin A), ascorbic acid (vitamin C), tocopherols (vitamin E) and melatonin(61). The increased production of ROS from dysfunctional mitochondria in disease conditions, however, leads to chronic oxidative damage which can contribute to cellular dysfunction and consequent neurotoxicity(61,177). Apart from production via mitochondrial respiratory chain reactions, there is also a simultaneous increase in extra-mitochondrial production of ROS in the cytosol(197). This leads to oxidative deactivation of many enzymes involved in, for example, regulation of glycolysis, in particular glyceraldehyde-3-phosphate dehydrogenase (GAPDH) and pyruvate kinase(197). Rhodopsin and other photosensitizers also augment the production of ROS in the retina during photopic vision, which, by definition, involves exposure of the retina to light(197).

The retina is exquisitely sensitive to oxidative damage given its relatively high level of oxygen consumption(197,198). Consequently, oxidative stress is a pathogenic feature of many vision-impairing diseases, including glaucoma, age-related macular degeneration, diabetic retinopathy, and uveoretinitis(103,104). However, dysfunctional, but not dead, RGCs may be amenable to recovery with early intervention that targets potential mitochondrial dysfunction and elevated oxidative stress, via minimising the generation or accumulation of ROS(31,61).

1.7.2. Excitotoxicity

The pivotal role of excitotoxicity in neurodegenerative disease, including glaucoma, is being revisited, and understanding its role in the treatment of optic neuropathies is receiving increasing attention. Excitotoxicity refers to cell death resulting from the toxic actions of excitatory amino acids(157,199). The stimulation of glutamate receptors, interleukin-1

receptors (IL-1Rs), JUN-linked receptors, and tumour necrosis factor receptors (TNFRs) triggers retinal neurons to undergo apoptosis through a cascade of cellular signalling events which in turn promote the release of cytochrome c and which activate the caspase pathways(2). Glutamate is the major excitatory neurotransmitter in the mammalian central nervous system and through prolonged exposure contributes substantially to the injury and death of neurons with the associated excessive influx of ions into the cell(199). The major ionotropic receptors activated by glutamate are N-methyl-D-aspartic acid (NMDA), α-amino-3-hydroxy-5-methylisoxazole-4-propionate (AMPA) and kainic acid (KA) receptors(199). Sustained activation ("overactivation") of glutamate receptors impairs cellular calcium homeostasis and activates nitric oxide synthesis, generation of free radicals and programmed cell death (Figure 3B)(157,199). Therapies targeting excitotoxicity, such as memantine and brominidine, have thus been explored for their therapeutic application in glaucoma.

1.8. Targeting Energy Metabolism

1.8.1. Glycolysis

Glycolysis is the oxygen independent metabolic pathway, which takes place in the cytosol of cells, to convert glucose into pyruvate to generate two ATP molecules per starting glucose. In the presence of oxygen, pyruvate is able to then enter the Kreb's cycle to generate 32-36 net ATP molecules within mitochondria, or in anaerobic conditions is instead converted to lactate in the presence of nicotinamide adenine dinucleotide (NAD+ or NADH)(Figure 3A). Whilst still in its infancy, experimental trials have demonstrated that through the manipulation of the glycoloytic pathway via substrate supplementation, RGC function and survival can be prolonged thereby affording a degree of neuroprotection in glaucoma(182,197,198,200).

1.8.1.1. Glucose

Using rat retinal explants Winkler *et al.* (1981) demonstrated that the majority of retinal ATP production can be maintained under conditions of oxygen deprivation provided that there is an abundance of glucose(201). *In vitro,* the neuroprotective effect of glucose administration is predominantly due to glycolytic ATP production which suggests that RGCs can up-regulate glycolysis during ischaemia to generate ATP(202). Studies have demonstrated that elevated vitreous glucose levels provide robust neuroprotection of RGC somata and axons against experimental retinal ischaemic injury (temporary unilateral pressure induced ischaemia and permanent ligation of both common carotids, respectively)(187,203) and experimental glaucoma (laser photocoagulation of the limbal plexus) in rats(200).

It was subsequently shown in clinical trials that contrast sensitivity was temporarily recovered in pseudophakic individuals with severe POAG after topical glucose application(204). Whilst glucose may provide a considerable degree of neuroprotection or recovery to damaged but not yet dead RGCs in the short term, long-term elevated vitreous glucose levels would possibly cause deleterious ocular complications such as cataract or diabetic-type retinal disease.

1.8.1.2. Pyruvate

Pyruvate is an endogenous alpha keto acid synthesised during the metabolism of glucose (Figure 3). Under normal circumstances, when oxygen is abundant, pyruvate is converted to acetyl CoA, which then enters the Kreb's cycle to contribute to the formation of substrates and electron donors for oxidative phosphorylation (OXPHOS) generating about 32 ATP molecules(202). In the face of oxygen deprivation (Figure 4), pyruvate is instead converted to lactate by lactate dehydrogenase (LDH) to regenerate nicotinamide adenine dinucleotide (NAD+)(202,205). It has been proposed that pyruvate can protect against oxidative stress,

whilst simultaneously providing energy substrate support(197,198,205) (Figure 5). Pyruvate could facilitate glycolysis by recycling of NAD+ required for the continued activity of the glycolytic pathway(197). Moreover, by scavenging various ROS species, pyruvate would also inhibit oxidative stress. This would prevent the toxic reactions of lipid peroxidation and loss of tissue thiols, thereby protecting the retina against further insult whilst supporting glycolysis(197,205). Pyruvate has also been shown to reduce the blood glutamate level, thereby potentially reducing glutamate-induced neurotoxicity, preventing neuronal network hyperexcitability, and reducing inflammation (205). In theory, therefore, pyruvate displays ideal credentials to provide therapeutic neuroprotection in glaucoma.
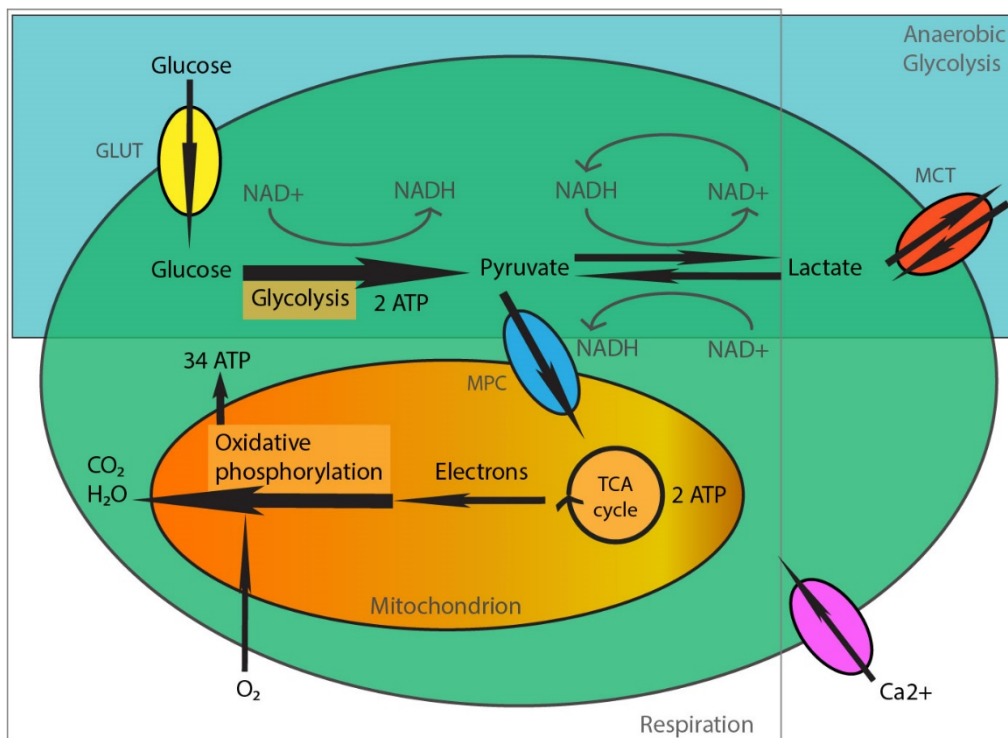
Figure 3. Normal cellular respiration. Under normal conditions glucose enters the cell through the transmembrane glucose transporter (GLUT) and is metabolised to pyruvate via glycolysis. If oxygen is abundant, pyruvate enters the tricarboxylate acid (TCA or 'Kreb's') cycle where it is metabolised via oxidative phosphorylation to form an abundance of ATP. Under anaerobic conditions pyruvate is instead preferentially converted to lactate, by lactate dehydrogenase

(LDH), in the presence of NADH. Conversely, lactate can also enter cells through the monocarboxylate transporter (MCT) and can be converted to pyruvate by LDH in the presence of NAD+.

Adapted from: Zilberter, Y. et al.(2015) A unique array of neuroprotective effects of pyruvate in neuropathology. Front. Neurosci; 9:17.
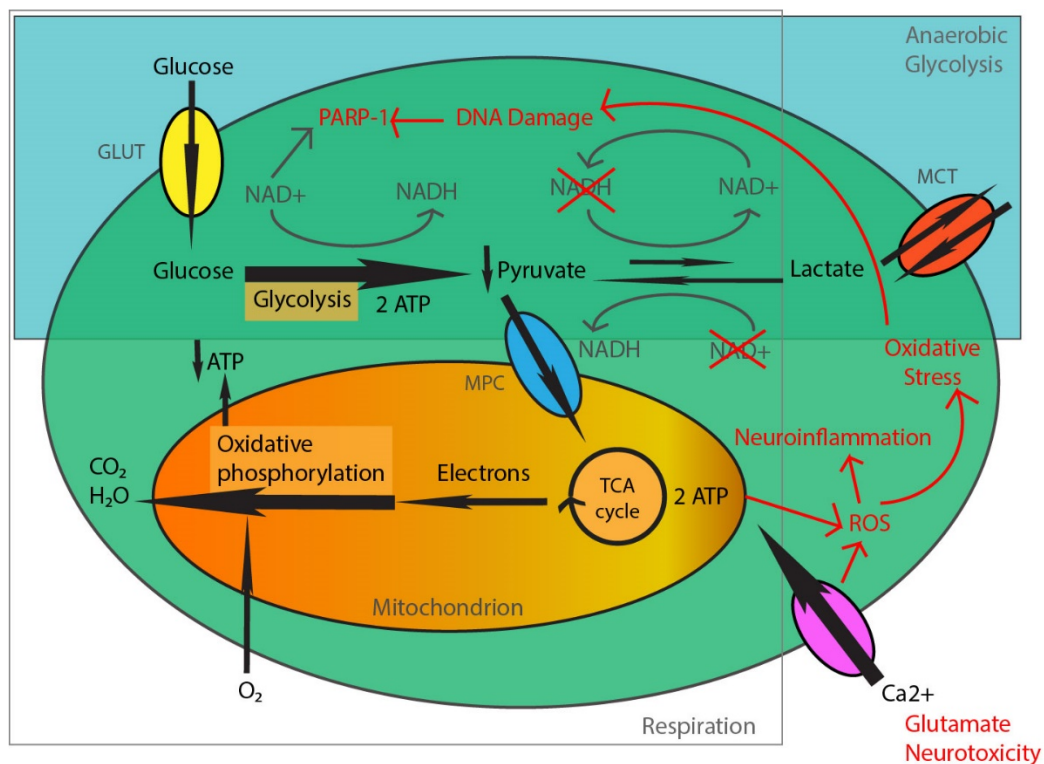
Figure 4. Pathology of cellular respiration during neurodegeneration. Both oxidative stress and extracellular glutamate trigger excitotoxicity, which contributes to neuronal degeneration. Glutamate accumulation triggers an influx of excessive calcium into cells. Reactive oxygen species accumulate and contribute to neuroinflammation and oxidative stress. DNA damage is induced by ROS leading to the overactivation of poly-ADP ribose polymerase-1 (PARP-1) causing depletion of cytostolic NAD+. Reduced NAD+ inhibits glycolysis with subsequent decline in mitochondrial ATP production, as well as limiting the conversion of lactate to

pyruvate. GLUT, Glucose Transporter; MCT, Monocarboxylate Transporter; MPC, Mitochondrial Pyruvate Carrier.

Adapted from: Zilberter, Y. et al.(2015) A unique array of neuroprotective effects of pyruvate in neuropathology. Front. Neurosci; 9:17.
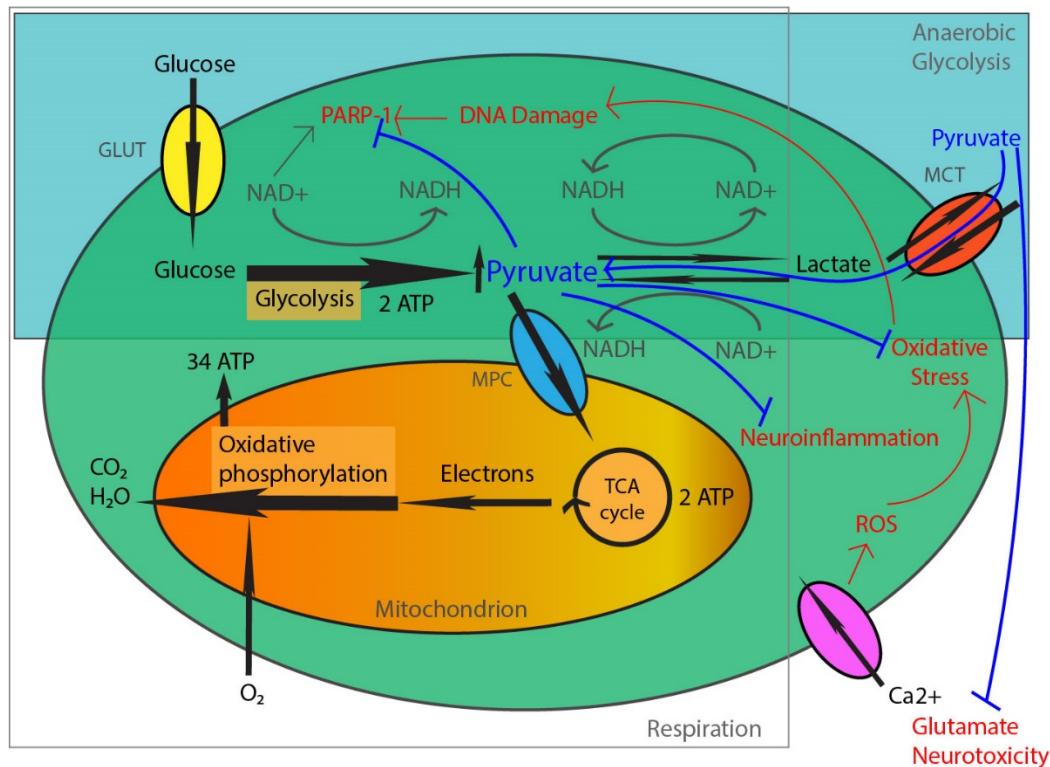
**Figure 5.** Cellular mechanism of pyruvate neuroprotection. Pyruvate is able to counteract substrate decline and support mitochondrial ATP production in conditions of neuronal stress (only when O2 is present). It also serves as a potent scavenger of reactive oxygen species, reduces neuroinflammation and subsequent oxidative stress. Pyruvate directly acts within the blood stream to lower glutamate levels, thereby reducing neuronal calcium (Ca2+) overload. Pyruvate promotes glycolysis by inhibiting PARP-1 overactivation, which effectively restores NAD+ levels. GLUT, Glucose Transporter; MCT, Monocarboxylate Transporter; MPC, Mitochondrial Pyruvate Carrier.

Adapted from: Zilberter, Y. et al.(2015) A unique array of neuroprotective effects of pyruvate in neuropathology. Front. Neurosci; 9:17.

1.8.1.3. Nicotinamide

Nicotinamide adenine dinucleotide (NAD) is a key molecule for mitochondrial health and nicotinamide (NAM) is a major precursor in the formation of NAD in mammals *in vivo*(206,207). NAM is unique among NAD precursors because it is a physiological inhibitor of the major NAD catabolic enzymes, namely CD38, PARPs (Poly (ADP-ribose) polymerase), and SIRTs (sirtuin)(206,208,209). Its physiological efficacy in glaucoma is supported by its favourable effects on calcium channel and calcium signalling (important in axon degeneration) (44,210,211), its vasoactive properties (with vascular dysfunction implicated in glaucoma) (150,212) and its ability to improve endothelial function and stabilising blood flow by reversing endothelin-mediated vasoconstriction (with endothelin receptor blockers shown to protect against glaucoma)(206,213).

The retinal level of NAD has recently been discovered to decline in an age-dependent manner(206,214), rendering RGC mitochondria vulnerable to IOP-dependent stresses(182,215). In a mouse model of hereditary glaucoma (DBA/2J (D2) mice) Williams *et al.*(2017) demonstrated that oral administration of nicotinamide and/or gene therapy (driving expression of *Nmnat1*, a key NAD+ -producing enzyme) was protective prophylactically and as an intervention, both histologically and functionally on pattern electroretinogram(182). More pertinently, up to 93% of eyes did not develop RGC soma loss and optic nerve degeneration with high dose nicotinamide supplementation, which also had an IOP lowering effect(182). The neuroprotective effect of nicotinamide is not necessarily IOP-dependent. Lower doses of nicotinamide also afforded protection against optic nerve degeneration, yet had

no effect on IOP(182). Nicotinamide was demonstrated to inhibit the formation of dysfunctional mitochondria(182), which suggests that it can protect against neuronal vulnerability to stress by supporting neuronal metabolism.

The Wallerian degeneration slow allele, Wld^s, decreases the vulnerability of RGCs subjected to elevated IOP by increasing retinal NAD levels(215). This extends on the finding that a mouse strain called Wallerian degeneration slow mice (Wld^s) contains a spontaneous dominant mutation that protects against neuronal insults, such as Parkinson's disease, hypoxic-ischemic injury, toxic neuropathy (taxol), and others(214,216). Williams *et al.*(2017) demonstrated that when coupled with nicotinamide administration, 94% of eyes were protected against glaucomatous neurodegeneration in a mouse glaucoma model (DBA/2J (D2) mice)(215). The Centre for Eye Research Australia has recently published the first clinical trial (prospective, double-masked, randomized, crossover clinical trial) to investigate the short-term effect of nicotinamide supplementation in patients with glaucoma (Trial ID ACTRN12617000809336). After 12 weeks of nicotinamide supplementation significant improvements in inner retinal function (assessed by photopic negative response (PhNR) on ERG) and a trend for improved visual field mean deviation were observed in the treatment group(217). This did not, however, translate to any significant difference in IOP, mean arterial pressure or RNFL thickness(217). Certainly, this preliminary evidence advocates for the use of nicotinamide and/or gene therapy in glaucoma and other neurodegenerative disease, with further studies required exploring its safety and efficacy in human disease.

1.8.1.4. Lactate and other Glycolytic Intermediates

It widely accepted that this intercellular lactate movement, via monocarboxylate transporters (MCTs), performs an essential function in the metabolic interaction between neurons and glia

via the astrocyte-neuronal lactate shuttle. In the central nervous system (CNS) it has recently been demonstrated that lactate has neuroprotective effects in models of excitotoxicity and energy depletion(218). It appears to constitute an alternative energy substrate for neurons lacking standard nutrients. This has been demonstrated in both *in vitro* and *in vivo* models of cerebral ischaemia(218). It has also been proposed that both the L- and D- forms of lactate play a role in intercellular communication via interaction with the HCA1 receptor(219). Studies performed by Tekkök *et al.* (2005) further support the hypothesis that L-lactate is released from astrocytes and taken up by axons as an energy source for sustaining their excitability(220).

These findings support the theory that should the metabolic astrocyte-neuronal lactate shuttle function within the retina then lactate administration could hold promise for future glaucoma neuroprotection studies. The existence of this shuttle in the retina, however, is, as yet unclear. Pioneering studies by the group of Tsacopoulos (221,222) using *in vitro* guinea pig retina preparations suggested that activity-dependent shuttling of glucose-derived lactate from Müller cells to photoreceptors does indeed occur. The interpretation of data reported in these studies, however, has been questioned (223), particularly in relation to both the actual cell preparations used and the fact that the guinea pig has a retina which lacks vasculature. It is possible that some shuttling of lactate does normally occur in the outer retina. For example, it has recently been proposed that lactate is released by photoreceptors to fuel RPE cells, thus allowing blood-borne glucose to pass straight to the former cells (224). However, the exact metabolic inter-relationships between cells in the outer retina remain elusive. The situation in the inner retina differs in vascular versus avascular retinas (223) where oxygen and glucose availability obviously differ. It is possible though, that in vascular retinas such as those of the primate, the presence of astrocytes closely associated with vessels in the inner regions of this tissue (225)

does indicate that, like in the brain, glucose and/or lactate shuttling can occur between different cells.

1.8.2. Oxidative Phosphorylation

Mitochondrial aerobic respiration through oxidative phosphorylation (OXPHOS) generates the majority of ATP in neurons and their axons. Given that OXPHOS, by definition, is dependent on oxygen and knowing that ischaemia likely plays a role in the pathogenesis of glaucoma, erythropoietin (EPO) has been proposed as a possible neuroprotective candidate. EPO is a glycoprotein cytokine secreted by the kidney in response to hypoxia, which in turn stimulates red blood cell production to improve the blood stream's oxygen carrying capacity. EPO and its receptors are distributed within the human retinal tissue and RPE[226], and Szabo *et al.* (2008) demonstrated that RGCs principally produce and secrete EPO[227]. Exogenous EPO administration has been demonstrated in *in vivo* glaucoma and optic nerve transection models to improve RGC survival and restore mitochondrial structure[228–230]. Yet a significant draw-back of EPO therapy is its promotion of angiogenesis causing pathological neovascularisation[226]. Whilst promising pilot studies have been performed looking at neuroprotection in optic neuritis in humans[231–234], no trials to date have been undertaken to assess the clinical utility of EPO in glaucoma.

Neuroglobin (Ngb) is linked to oxidative metabolism and is hypothesised to have a myoglobin-like role in supplying oxygen to the respiratory chain of neurons whilst also protecting them from ROS[235]. Both Ngb and Cytoglobin are present in distinct nerve cell populations, including human retinal neurons and RPE[236]. In fact, the Ngb concentration in the retina is 100-fold higher than any other nervous tissues with this protein being especially abundant (~10-fold higher) in the RGC layer and optic nerves than in the other layers of the retina[237].

Ngb has shown a promising neuroprotectant property in murine cerebral and retinal ischaemia(235,238), and has also been found to prevent RGC damage induced by glutamate cytotoxicity in vitro and/or by chronic IOP elevation *in vivo*(239,240). Ngb has not only been demonstrated to improve the survival of RGCs after optic nerve injury, but in mouse retinas showing enhanced Ngb expression was found to regenerate central optic axon outgrowth(241). Ngb may modulate RGC susceptibility to glaucomatous neural damage and may therefore represent a novel neuroprotective and neuroregenerative therapy for this disease.

The general aim of pharmacological therapy in targeting mitochondrial dysfunction in glaucoma is to improve energy production and protect cells from ROS toxicity(61). A review of experimental mitochondrial therapies in neurodegenerative disease with possible translation to optic neuropathies is comprehensively detailed by Lopez *et.al.*(2016)(61). Those compounds/therapies targeted against oxidative damage include mitoquinone mesylate (Mito-Q), co-enzyme Q10 (CoQ10), carotenoids, idebenone, exogenous glutathione, and methylene blue(61). However, to date there are no clinically trialled drugs with definitive therapeutic efficacy for the treatment of mitochondrial dysfunction in glaucoma.

1.8.3. Pentose Phosphate Pathway (PPP)

Parallel to the glycolytic pathway is the pentose phosphate pathway (PPP), taking place in the cytosol of cells. Using glucose as its primary substrate, the PPP generates NADPH and pentose sugars as well as ribose 5-phosphate (a precursor for the synthesis of nucleotides)(242). The production of cellular reducing equivalents can in turn be used in reductive biosynthesis reactions within cells. NADPH also functions to prevent oxidative stress thereby preventing apoptotic cell death(243) and in photoreceptors, this compound is further involved in the recycling of photopigments(221,244). It has been hypothesised that glucose can directly

provide cytoprotection through its oxidation via the PPP by maintaining cellular reducing power(242,243).

Using rat retinal cultures, Han *et al.* (2013) demonstrated that administration of the 6-phosphogluconate dehydrogenase inhibitor, 6-AN, inhibited the PPP and reduced the protective effect of glucose against rotenone-induced retinal cell toxicity(245). Contrary to this, Winkler *et al.* (1997) showed that the portion of total glucose metabolised via the PPP did not increase significantly in the isolated retina when glucose was elevated from 5mM to 30mM(246). This suggests that PPP-derived NADPH may only play a minor role in neuronal functioning. It further supports previous findings that ATP production from glycolysis constitutes the most important glucose-induced neuroprotective mechanism in retinal ischaemia(245).

2. Aims and rationale

The overriding aim of this project was to further our understanding of RGC energy metabolism, and, to manipulate RGC energy metabolism for clinical advantage using an *in vivo* experimental model of glaucoma. The thesis is divided into two studies.

In the first study, we developed a new methodology for quantifying RGCs. Quantification of RGC survival from immunolabelled wholemounts is one of the most widely used and critical measures to inform the success or failure of neuroprotection in experimental glaucoma studies. Yet, quantifying RGCs is a time-consuming and laborious task prone to sampling bias and inter / intra-observer variability. Thus, we sought to develop an automated cell counting algorithm and validate it against an array of immunolabelled RGC wholemounts. This would ultimately expedite data acquisition for statistical analysis, permit entire RGC populations on wholemounts to be quantified (rather than sectoral analysis, which is prone to sampling bias), and inform researchers about the success or failure of putative neuroprotective agents in a timelier and more objective manner. These data are documented in chapter three.

In the second study, we explored the neuroprotective efficacy of the energy substrate pyruvate. Our therapeutic-based study was conducted to assess: (1) whether oral pyruvate supplementation increases the bioavailability of pyruvate to the retina; (2) the effects of pyruvate as a potential neuroprotective agent for RGCs and the optic nerve in experimental glaucoma; (3) the mechanism(s) of pyruvate neuroprotection using mixed retinal cell cultures. The rationale for the study stemmed from earlier published studies by our laboratory demonstrating bioenergetic neuroprotection with glucose in both an experimental model of glaucoma and in the clinic(200,204,247). Given the serious limitations of long-term glucose administration, such as diabetic retinopathy and cataract formation, the goal was to assess the

neuroprotective effectiveness of an alternative energy substrate for RGCs that is both safe and easily deliverable. This study was undertaken as an international collaborative effort with researchers at The Jackson Laboratory (Bar Harbour, ME, USA). The Jackson Laboratory studied the neuroprotective effects of oral pyruvate administration in their chronic rodent model of glaucoma (using the DBA/2J mouse model of hereditary glaucoma over 12 months). Our subacute model of induced experimental glaucoma in rats (using the laser photocoagulation model to achieve acute IOP elevation over 2 weeks) would provide complimentary data, investigating the neuroprotective effects of oral pyruvate in a different species, in a different disease model, and over a different time frame. The combined results would thereby provide more robust data to inform translation to the clinic. Chapter four documents the data from this study.

3. Published Paper - Software for Quantifying and Batch Processing Images of Brn3a and RBPMS Immunolabelled Retinal Ganglion Cells in Retinal Wholemounts

Statement of Authorship

Title of Paper	Software for Quantifying and Batch Processing Images of Brn3a and RBPMS Immunolabelled Retinal Ganglion Cells in Retinal Wholemounts
Publication Status	☑ Published ☐ Accepted for Publication ☐ Submitted for Publication ☐ Unpublished and Unsubmitted work written in manuscript style
Publication Details	Guymer C, Damp L, Chidlow G, Wood J, Tang YF, Casson R. Software for quantifying and batch processing images of Brn3a and RBPMS immunolabelled retinal ganglion cells in retinal wholemounts. Trans Vis Sci Tech. 2020;9(6):28

Principal Author

Name of Principal Author (Candidate)	Dr Chelsea Guymer
Contribution to the Paper	Performed analysis on all samples, interpreted data, wrote the manuscript.
Overall percentage (%)	75%
Certification:	This paper reports on original research I conducted during the period of my Higher Degree by Research candidature and is not subject to any obligations or contractual agreements with a third party that would constrain its inclusion in this thesis. I am the primary author of this paper.
Signature		Date	08.06.2020

Co-Author Contributions

By signing the Statement of Authorship, each author certifies that:

    i.   the candidate's stated contribution to the publication is accurate (as detailed above);

    ii.   permission is granted for the candidate in include the publication in the thesis; and

    iii.   the sum of all co-author contributions is equal to 100% less the candidate's stated contribution.

Name of Co-Author	Mr Lloyd Damp
Contribution to the Paper	Developed the software, assisted in writing the manuscript (detailing technical aspects of software development and supplement 1).
Signature		Date	08.06.2020

Name of Co-Author	Dr Glyn Chidlow
Contribution to the Paper	Supervised development of work, helped in data interpretation and manuscript evaluation.
Signature		Date	9/6/2020

Name of Co-Author	Dr John Wood		
Contribution to the Paper	Helped to evaluate and edit the manuscript.		
Signature		Date	10-06-20

Name of Co-Author	Dr Yi Fan Tang		
Contribution to the Paper	Assisted with data collection.		
Signature		Date	9/6/2020

Name of Co-Author	Prof Robert Casson		
Contribution to the Paper	Helped to evaluate and edit the manuscript.		
Signature		Date	8 June 2020

Article

Software for Quantifying and Batch Processing Images of Brn3a and RBPMS Immunolabelled Retinal Ganglion Cells in Retinal Wholemounts

Chelsea Guymer[1], Lloyd Damp[2], Glyn Chidlow[1], John Wood[1], Yi Fan Tang[3], and Robert Casson[1,3]

[1] Ophthalmic Research Laboratories, Discipline of Ophthalmology and Visual Sciences, University of Adelaide, Adelaide Health and Medical Sciences Building, North Terrace, Adelaide, Australia
[2] Southern Launch, Adelaide, Australia
[3] Department of Ophthalmology, Royal Adelaide Hospital, Adelaide, Australia

Correspondence: Robert Casson, Ophthalmic Research Laboratories, Level 7 Adelaide Health and Medical Sciences Building, The University of Adelaide, North Terrace, Adelaide SA 5000, Australia. e-mail: robert.casson@adelaide.edu.au

Purpose: The ability to accurately quantify immunohistochemically labeled retinal ganglion cells (RGCs) on wholemounts is an important histopathological determinant in experimental retinal research. Traditionally, this has been performed by manual or semi-automated counting of RGCs. Here, we describe an automated software that accurately and efficiently counts immunolabeled RGCs with the ability to batch process images and perform whole-retinal analysis to permit isodensity map generation.

Methods: Retinal wholemounts from control rat eyes, and eyes subjected to either chronic ocular hypertension or N-methyl-D-aspartate (NMDA)-induced excitotoxicity, were labeled by immunohistochemistry for two different RGC-specific markers, Brn3a and RNA-binding protein with multiple splicing (RBPMS). For feasibility of manual counting, images were sampled from predefined retinal sectors, totaling 160 images for Brn3a and 144 images for RBPMS. The automated program was initially calibrated for each antibody prior to batch analysis to ensure adequate cell capture. Blinded manual RGC counts were performed by three independent observers.

Results: The automated counts of RGCs labeled for Brn3a and RBPMS closely matched manual counts. The automated script accurately quantified both physiological and damaged retinas. Efficiency in counting labeled RGC wholemount images is accelerated 40-fold with the automated software. Whole-retinal analysis was demonstrated with integrated retinal isodensity map generation.

Conclusions: This automated cell counting software dramatically accelerates data acquisition while maintaining accurate RGC counts across different immunolabels, methods of injury, and spatial heterogeneity of RGC loss. This software likely has potential for wider application.

Translational Relevance: This study provides a valuable tool for preclinical RGC neuroprotection studies that facilitates the translation of neuroprotection to the clinic.

Introduction

Glaucoma describes a group of ocular conditions united by a clinically characteristic intraocular pressure (IOP)-associated optic neuropathy with associated loss of retinal ganglion cells (RGCs).[1] Currently, IOP reduction is the only proven treatment; however, additional neuroprotective strategies that attenuate RGC loss would be highly clinically desirable.

Quantification of RGCs on retinal wholemounts is a commonly used outcome measure in preclinical

1

studies investigating potential efficacy of neuroprotectants to RGCs in animal models. A variety of labeling techniques can be used to assess RGC survival, including the use of retrograde tracers, such as Fluorogold; labeling with neuronal markers, such as NeuN, Neurotrace, or βIII-tubulin; or immunolabeling with RGC specific markers, including Brn3a, RNA-binding protein with multiple splicing (RBPMS), and gamma (γ)-synuclein.[2–16] Each marker provides a different methodological challenge. For example, quantifying RGCs using markers, such as γ-synuclein, that stain axons as well as somas is problematic from a technical perspective, because labeled axon fibers often obscure underlying RGCs.[7]

RGC quantification is typically approached by selectively imaging predefined sectoral regions of the retina at set distances from the optic nerve and counting the number of RGCs within each region.[14] Semi-automated or manual counting methods are normally used, and these are labor-intensive, time-consuming, and open to subjective bias. Sectoral differences in RGC density can also produce bias in the results, unless the entire retina is imaged.[17] Rapid automation of RGC quantification on retinal wholemounts, therefore, has the potential to accelerate data collection and reduce bias. It could also potentially be applied to the whole retina, enabling the generation of RGC isodensity maps.[10,16]

A limited variety of software packages have been developed to expedite cell counting in rodent retinal wholemounts. These include commercially available software, such as MetaMorph,[18] StereoInvestigator,[19] and IPlab;[20] novel programs created by individual laboratories[10,21]; and open-source programs, such as ImageJ and CellProfiler, with macros providing automated cell counting functionality (see Table 4). However, the wider adoption of these programs has been limited, perhaps due to the limited applicability to different immunolabels or tissue mediums.

Here, we present an automated, freely available software validated for RGC-specific labels Brn3a and RBPMS in rodent retinal wholemounts. It has the capacity to differentiate individual cells in a cluster, batch process images with the same immunolabel, and export the results in tabular format to a spreadsheet to expedite data analysis. This program has been validated on RGC-specific immunolabels on confocal low magnification ($\times$10) images, can tolerate both naïve and injured retina interchangeably, and has the added feature of automatically subtracting dirt or artifacts in the case of imperfect immunostaining. It also has the ability to provide whole-retinal analysis and integrated retinal isodensity map generation.

Materials and Methods

Animals and Procedures

This project was approved by the Animal Ethics Committees of SA Pathology/Central Adelaide Local Health Network and the University of Adelaide (Adelaide, Australia) and conformed with the Australian Code of Practice for the Care and Use of Animals for Scientific Purposes, 2013, and with the ARVO Statement for the use of animals in vision and ophthalmic research. Adult Sprague-Dawley rats (aged 10 weeks+, <230 g; $n = 18$) were housed in a temperature- and humidity-controlled room with 12-hour light and dark cycles. Food and water were provided ad libitum.

The experimental plan comprised three cohorts of animals (groups 1 to 3) that were immunolabeled and analyzed as discrete batches. For group 1, experimental glaucoma was induced in the right eye, leaving the untouched left eye to serve as a control. This group comprised $n = 10$ injured eyes and $n = 10$ naïve eyes and all eyes were analyzed for Brn3a. Glaucoma was induced using a slightly modified protocol of the method described by Levkovitch-Verbin et al.[22] Rats were humanely euthanized after two weeks. Elevated IOP over the course of two weeks using this model causes measurable loss of RGCs and their axons.[23,24] Group 2 comprised $n = 4$ untreated rats of which one eye per rat was analyzed for RBPMS. For group 3, an intravitreal injection of 40 nmol of NMDA (5 µl in sterile saline) was performed in the right eye, leaving the untouched left eye to serve as a control. Group 3 comprised $n = 4$ injured eyes and $n = 4$ naïve eyes and all eyes were analyzed for RBPMS. Rats were humanely euthanized after one week, because NMDA causes a marked loss of RGCs at this time point.[25,26]

Tissue Processing and Immunohistochemistry

All rats were terminally anesthetized by transcardial perfusion using physiological saline. Whole eyes were removed and placed in 10% neutral buffered formalin for one hour. Posterior eye-cups were carefully dissected and each retina was prepared as a flattened wholemount via four relaxing incisions. Retinas were permeabilized with phosphate buffered saline (PBS; 137 mM NaCl, 5.4 mM KCl, 1.28 mM NaH_2PO_4, 7 mM Na_2HPO_4; and pH 7.4) containing 1% Triton X-100 (PBST-1%), blocked in PBST-1% containing 3% (v/v) normal horse serum, then incubated for three days at 4°C in the same solution containing either goat
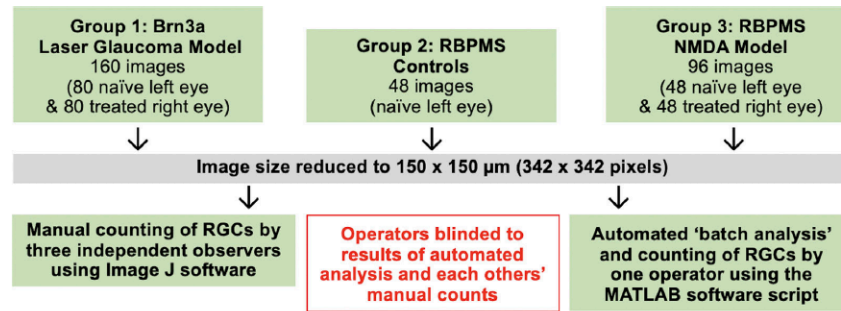
Figure 1. Flowchart summarizing the protocol followed for manual and automated analysis of immunolabeled images.

anti-Brn3a primary antibody (1:600; SC-31984; Santa Cruz Biotechnology, Santa Cruz, CA) or rabbit anti-RBPMS primary antibody (1:500; ABN1362; Merck Millipore, Bayswater, Victoria, Australia).

After multiple washes with PBST, wholemounts were incubated overnight at 4°C with alexa fluor 488 or 594-conjugated donkey anti-goat secondary antibody (for Brn3a) or alexa fluor 488 or 594-conjugated donkey anti-rabbit secondary antibody (for RBPMS; 1:500; Invitrogen, Mulgrave, Victoria, Australia), before rinsing in PBS and mounting using anti-fade mounting medium.

Imaging of Retinal Wholemounts

Wholemounts were examined under a confocal microscope with images captured at 10× magnification, corresponding to a sampling region of 700 × 525 μm. For feasibility of manual counting, of this sampled region the image was cropped to 150 × 150 μm and these fames were manually and automatically quantified. For Brn3a (group 1), images were sampled from both central and peripheral regions of each of the superior, inferior, nasal, and temporal quadrants, corresponding to eight images per sampled retina. For RBPMS (groups 2 and 3), images were sampled from central, middle, and peripheral regions of each superior, inferior, nasal, and temporal quadrants, corresponding to 12 images per sampled retina (Fig. 1). The primary aim of this study was to compare the accuracy of manual counts to corresponding automated cell counts in each sampled image for each immunolabel rather than measuring the effect of any intervention on RGC density. Therefore, the manual cell count was directly compared with the corresponding automated cell count of each immunolabeled image and results collated for each RGC marker.

To demonstrate RGC quantification of entire retinal wholemounts with corresponding retinal isodensity map generation, high resolution images of two naïve entire retinal wholemounts immunolabelled with Brn3a were captured on Hamamatsu NanoZoomer 2.0-HT fluorescence module at 20× magnification. These images were viewed using the Hamamatsu NanoZoomer Digital Pathology system and exported as a TIFF.

Algorithm Development

The code steps through five procedures that "de-clump" and count "circular" cells within an image. The first three steps are designed to intensify the boundary between cells. Existing programs can count cells when the images are well structured with clear boundaries between cells but are often compromised by: (1) cell clumping or overlapping; (2) nonuniform illumination; (3) artifacts; (4) markers camouflaged by background noise; and (5) irregularity of shape.

The fourth step undertakes an analysis of the prepared image and identifies areas of circular patterns using an efficient Hough transform. An optional fifth step checks the validity of the cell count generated in the fourth step by comparing the integrated image intensity within the proposed cell to a user specified threshold, the degree to which the cell is filled as well as the overlap between neighboring cells. An optional heat map can be generated from the output from steps 4 and 5 based on the industry standard Kernel Density Function using a gaussian Kernel. Please refer to Supplementary Material S1 for a more detailed explanation of the algorithm development. A graphic user interface (GUI) for the algorithm was developed to facilitate ease of use, with an example and explanation of its functions demonstrated in Figure 2.

Batch Processing

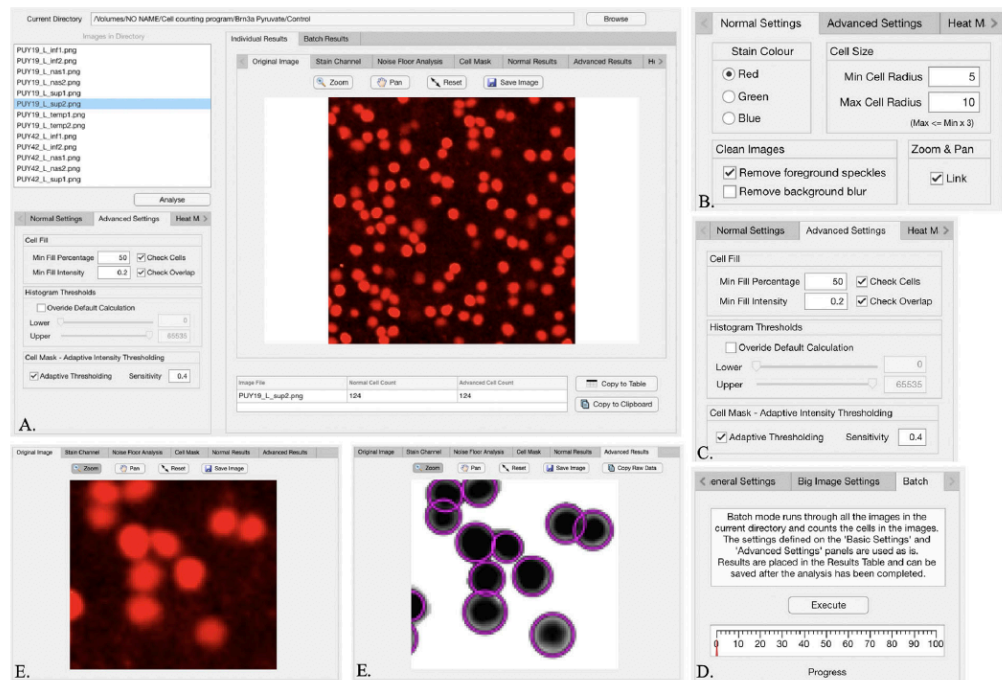The user has the option to batch-process a directory of images using either a set of parameters

translational vision science & technology

Figure 2. Interface of the Automated Cell Counting Program Software. (A) The "browse" option allows the user to access image folders and files, as listed in the upper left window titled "Images in Directory." (B, C) Images can be individually analyzed with user-defined parameters calibrated to accurately capture and quantify cells, or (D) a "batch" analysis can be performed of all images in that directory using the highlighted tab in the bottom left window. In this window, the user can select the settings necessary to direct automated cell capture and quantification by the algorithm, such as (B) stain color, cell size (setting the radius of the circular sample, which defines the immunolabeled cell), "clean images" option to remove foreground speckles (i.e. artifact) or background blur (background noise), (C) "cell fill" defining the minimum threshold by which the immunolabel should occupy the circular sample (expressed as a percentage), and minimal fill intensity (i.e. brightness / intensity of stain color taken up by the cell). The "check cell" option will circumscribe the cells identified by these parameters in the "advanced results" tab to allow the user to check automated cell capture against the original image. The "normal results" tab circumscribes cells based on all user-defined parameters other than the "cell fill" and "minimal fill intensity" options. (B, E) The "link zoom" feature allows a zoomed-in area of interest from the original image to be mirrored in the "normal results" and "advanced results" tabs to allow the user to manually check the accuracy of automated cell capture and adjust the settings to optimize the result. Tabulated results can be exported to Excel for ease of data analysis.

determined in advance by the user or by letting the program automatically threshold a number of images stored together using the above method. Processed images are annotated to indicate the number of cells counted, along with the estimated cell boundaries. Results are provided in tabular format for further statistical analysis with user controls simplifying the data export to comma separated value (CSV) format.

Data Acquisition

The program was initially calibrated for each respective immunohistochemical label prior to batch analysis

(i.e. all images of that label were seamlessly analyzed using the same objective parameters set by the user to ensure adequate cell capture). Calibrations taken into account were as follows: (1) stain color channel (red, green, and blue), (2) cell size (pixels), (3) option to remove foreground speckles (artifact) or background blur for imperfect immunostaining, (4) cell fill (i.e. the minimum fill percentage was set to 50%, indicating that for cells abutting the border of an image at least 50% of its sphere must be visible for it to be counted, and minimum fill intensity was set to 0.2 (20%), to exclude background artifact and poorly visible background cells without clear border definition), and (5) adaptive
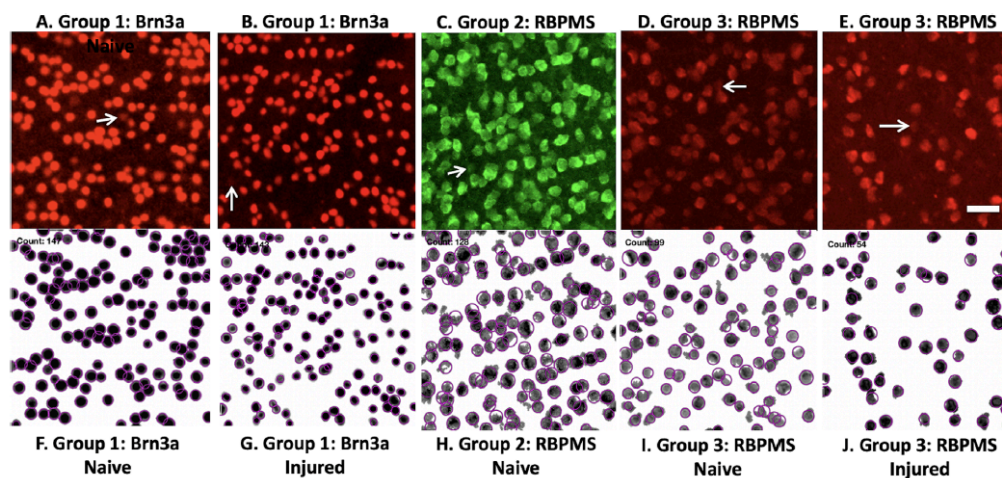
56

Figure 3. Representative immunolabeled images for Brn3a and RBPMS (A–E) and the corresponding processed images ready for automated counting (F–J). Scale bar = 25 μm, 10 × magnification immunolabeled confocal photomicrographs, 150 × 150 μm cropped frames. Arrows demonstrate faintly visible cells in the background with poor border definition, which were excluded from both manual and automated counts.
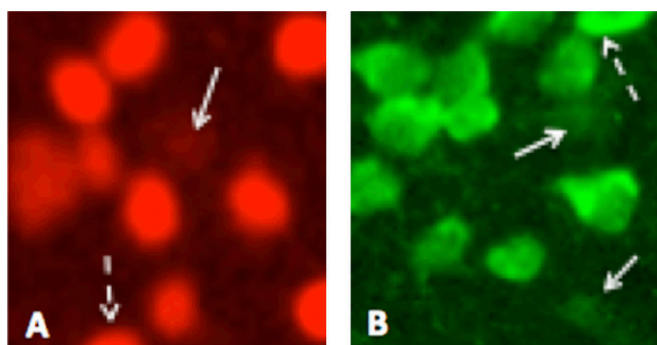

Figure 4. Examples of counting rules followed by manual observers (please note zoomed-in images are not to scale). (A) Brn3a immunolabelled RGCs. (B) RBPMS immunolabelled RGCs. Arrows (→) highlight faintly visible cells with poor border definition and dashed arrows; (–>) demarcate cells of which <50% of the cell was visualized on the image border, both of which were excluded from manual counts.

thresholding of 0.4 that calculates a locally adaptive lighting threshold with a sensitivity toward thresholding more pixels as background than foreground. These parameters were in keeping with manual "counting rules," as described below. Apart from being aware of which particular label was being quantified, automated analyses were performed in a blinded fashion (i.e. the operator remained unaware of the corresponding manual count for each image). An example of the end point of processing to produce automated counts of RGCs for each particular label and group is shown in Figure 3.

Manual RGC counts were acquired by three independent observers using the "point tool" counter with ImageJ software (imagej.net, version 2.0.0-rc-43/1.51q). Observers were provided with "counting rules" to follow, namely: (1) cells that were abutting the boundary of the image were only to be counted if at least 50% of the cell was visualized (i.e. forming a semicircle, but no less), and (2) poorly visible cells in the background were to be excluded if their cell boundaries were not clearly evident (Fig. 4). Observers were blinded both to counts from other observers and to that of the automated cell counting software.

Table 1. ICC (95% CI) of Immunohistochemical Labels (Correlation Between all Three Observers)

	Group 1: Brn3a (OHT model)	Group 2: RBPMS (Controls only)	Group 3: RBPMS (NMDA model)
Naïve retina	0.876 (0.826 to 0.914)	0.924 (0.882 to 0.954)	0.977 (0.964 to 0.986)
Injured retina	0.991 (0.987 to 0.994)	N/A	0.917 (0.871 to 0.950)

CI, confidence interval; ICC, intraclass correlation coefficient; N/A, not applicable; NMDA, *N*-methyl-D-aspartate; OHT, ocular hypertension.

Table 2. Bland-Altman Tests - Bias (95% Limits of Agreement) (GT versus Automated Counts)

	Group 1: Brn3a (OHT model)	Group 2: RBPMS (Controls only)	Group 3: RBPMS (NMDA model)
Naïve retina	−0.231 (−7.209 to 6.747)	−0.314 (−12.054 to 11.426)	−0.058 (−12.130 to 12.014)
Injured retina	−3.03 (−18.553 to 12.493)	N/A	5.18 (−4.700 to 15.060)

GT, ground truth (average of manual counts of three independent observers); NMDA, *N*-methyl-D-aspartate; N/A, not applicable; OHT, ocular hypertension.

Table 3. Linear Regression Analysis – Slope of Best Fit (R2) (GT vs Automated Counts)

	Group 1: Brn3a (OHT model)	Group 2: RBPMS (Controls only)	Group 3: RBPMS (NMDA model)
Naïve retina	0.909 (0.979)	0.801 (0.875)	0.962 (0.979)
Injured retina	0.949 (0.991)	N/A	0.945 (0.978)

GT, ground truth (average of manual counts of three independent observers); NMDA, *N*-methyl-D-aspartate; N/A, not applicable; OHT, ocular hypertension.

Results

The average manual count of the three independent observers was set as the ground truth (GT). Agreement among the observers was quantified using the intraclass correlation coefficient (ICC; Table 1). Agreement between the GT and the automated cell count was investigated using Bland-Altman plots (Table 2, Fig. 5), and linear regression analysis (R2; Table 3, Fig. 6) was used to model the relationship between these two variables. To obtain accurate estimates of the SDs in the Bland-Altman plots, which accounted for the correlated nature of the data (multiple images from each rat retina), a linear mixed model was constructed and the variance components analyzed.[27,28] Statistical analyses were performed by using statistical software GraphPad Prism 8 and R statistical Software. Integrated whole retinal analysis and retinal isodensity map generation are demonstrated (Fig. 7).

Overall Performance of Automated versus Manual Counts on Brn3a and RBPMS Immunolabeled Retina

There was excellent agreement among the three experienced observers performing the manual cell counts (Table 1) and the automated script performed equally well for both healthy and damaged retinas (Table 2, Table 3, Fig. 5, Fig. 6). Each immunolabeled image took a manual observer approximately 2 minutes to count, whereas the automated program was able to batch process 40 immunolabelled images within 2 minutes. Hence, efficiency in counting immunolabeled
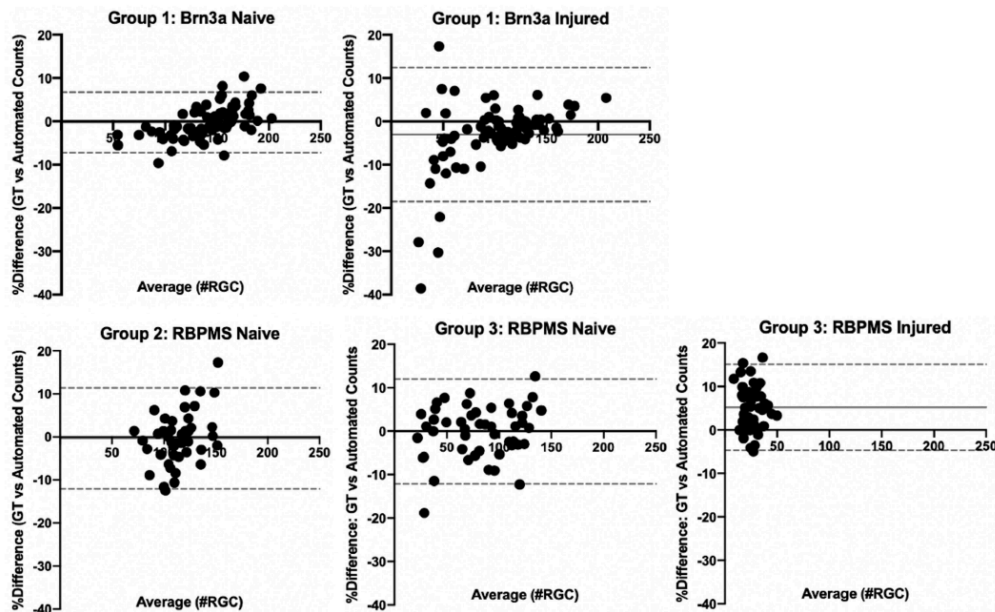
58

Figure 5. Bland-Altman Plots of Ground Truth (GT) versus Automated Counts in both naive and injured retina. The uninterrupted line (___) indicates the bias. The dashed lines (—) indicate the 95% limits of agreement. Group 1, Brn3a OHT model ($n = 80$ frames for both naïve and injured retinas); group 2, RBPMS naïve cohort ($n = 48$ frames for naïve retinas only); group 3, RBPMS NMDA model ($n = 48$ frames for both naïve and injured retinas).

RGC wholemount images can be accelerated by 40-fold using the automated script.

Bland-Altman tests (Table 2, Fig. 5) in Brn3a and RBPMS immunolabeled retinal images taken from naïve retina across all groups (1-3) calculated a bias close to zero (-0.314 to -0.058). This indicates that, on average, there was almost no difference between manual and automated counts. There was more ambiguity in the average difference in manual and automated counts for group 1 Brn3a immunolabeled injured retinal images and group 3 RBPMS immunolabeled injured retinal images, given the larger bias (-3.03 and 5.18, respectively) and 95% limits of agreement (-18.553 to 12.493, and -4.700 to 15.060, respectively). The quality of immunohistochemistry was varied both within and between sampled groups, for naïve and injured retina, and the quality of immunohistochemistry labeling can influence the accuracy of the automated cell counts. Injured retinas generally exhibited poorer quality immunolabeling, with increased background staining and artifact, which may account for the difference.

Linear regression analysis (Table 4, Fig. 6) of automated versus manual counting for group 1 (ocular hypertension model) Brn3a-labeled RGCs demonstrated a slope of best fit of 0.909 (naïve retina) and 0.949 (injured retina) with R^2 of 0.979 and 0.991, respectively. Similarly, group 3 (NMDA model) RBPMS-labeled RGCs demonstrated a slope of best fit of 0.962 (naïve retina) and 0.945 (injured retina) with R^2 of 0.979 and 0.978, respectively. Given that the slope was almost 1, this indicates that essentially no underestimation occurred. For group 2 naïve RBPMS-labeled RGCs, linear regression analysis of automated versus manual counting demonstrated a slope of best linear fit of 0.801 with R^2 of 0.875, indicating a slight underestimation of RGC using the automated method.

Whole Retinal Analysis and Retinal Isodensity Map Generation

The program has the integrated ability to efficiently provide whole-retinal RGC quantification and generate a corresponding retinal isodensity map ("heat map"; Fig. 7). The script is able to automatically delineate the retinal wholemount borders and is able to exclude small areas of artifact. Retinal wholemount
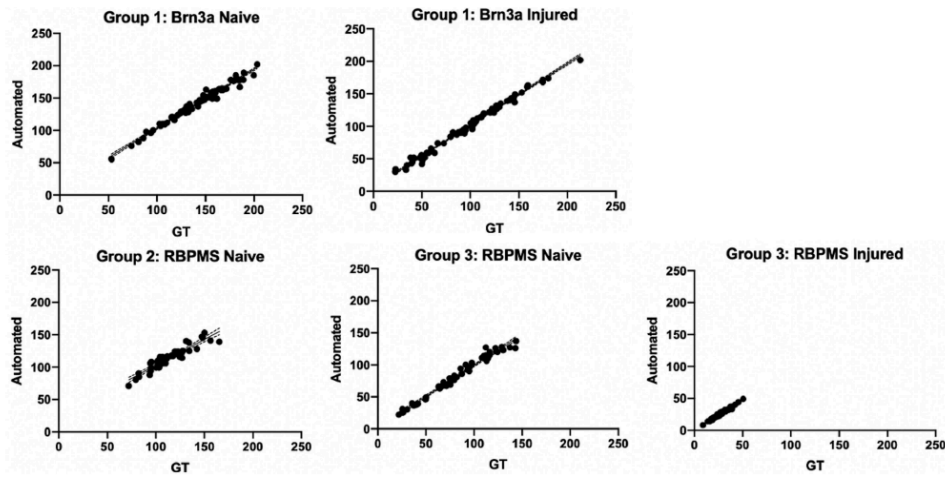
Figure 6. Linear regression analysis in naïve and injured retina demonstrated a strong linear correlation between the averaged manual counts of three observers (Ground Truth [GT]) and automated cell counts. Group 1, Brn3a OHT model ($n = 80$ frames for both naïve and injured retinas); group 2, RBPMS naïve cohort ($n = 48$ frames for naïve retinas only); group 3, RBPMS NMDA model ($n = 48$ frames for both naïve and injured retinas).

Table 4. Reported Automated Methods for RGC Counting in the Rodent Retina

Author	Immunostain	Free to use?	Accuracy
Guymer et.al. (2020)	Brn3a	Yes	
	- Naïve retina		$R2 = 0.979$
	- Injured retina		$R2 = 0.991$
	RBPMS		
	- Naïve retina		$R2 = 0.875 – 0.979$
	- Injured retina		$R2 = 0.978$
Nadal Nicholás et al. (2009)[15]	Brn3a	No	$R2 = 0.98$
Geeraerts et al. (2016)[16]	Brn3a	Yes	$R2 = 0.96$ (widefield images) $R2 = 0.99$ (confocal images)
Salinas-Navarro et al. (2009)[21]	Fluorogold	No	$R2 = 0.99$
Denias et al. (2002)[17]	Fluorogold	Yes	$R2 = 0.94$
Danias et al. (2003)[10]	Fluorogold	Yes	$R2 = 0.95$
Dordea et al. (2016)[30]	DAPI and βIII Tubulin	Yes	$R2 = 0.64$ (optimal quality images) $R2 = 0.22$ (poorer quality images)

RGC automated counts are displayed in a summary table, which can be exported into an Excel (Microsoft Office) spreadsheet, and the counted image with corresponding heat map can be saved as a high-resolution JPEG or PNG file. Retinal wholemount RGC automated counts can be visually checked against the original immunolabeled image by zooming in on any area of interest. The density of cells across the image is calculated using a Kernal Density Estimate (KDE) to generate the heat map. Please refer to Supplementary Material S1 (Heat Map Generation section) for a more detailed explanation.
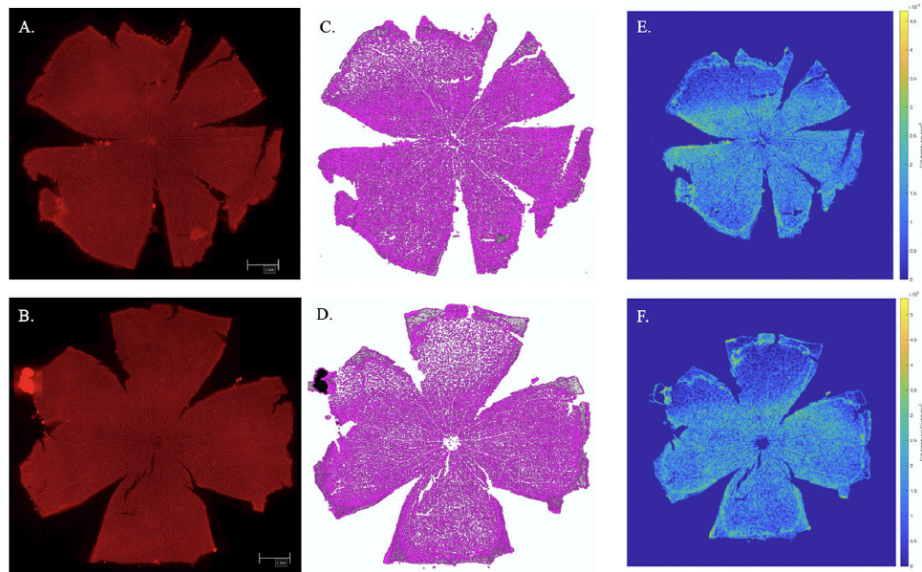
translational vision science & technology

60

Figure 7. Representative images of (A, B) original image of two naïve retinal wholemounts immunolabeled with Brn3a (captured on Hamamatsu NanoZoomer 2.0-HT fluorescence module, 20 × magnification, viewed using the Hamamatsu NanoZoomer Digital Pathology system, exported as a TIFF), (C, D) respective whole-retinal RGC quantification and (E, F) corresponding retinal isodensity maps ("heat maps"). Scale bar = 1 mm.

Discussion

Manual counting has traditionally represented the standard way to accurately quantify RGC populations on immunohistochemically labeled retinal wholemounts. This procedure, however, is a labor intensive and time-consuming task prone to subjectivity relating to sampling bias and inter/intra-observer variability. This, in turn, has motivated us to develop software built on the MathWorks product to perform automated cell counts. Our program, which we intend to make freely available, has the versatility of being able to analyze RGC-specific labels (Brn3a and RBPMS) and can handle both naïve and diseased retinas. We have validated this software against the manual counting of three independent observers and proven that it possesses an accuracy is at least comparable to quoted data in the recent literature[10,15–17,29,30] (Table 4). We have also demonstrated this script's ability to provide efficient automated RGC counts of entire retinal wholemounts, permitting the generation of retinal isodensity maps to allow the detection of regional differences in RGC density. These features have been seamlessly integrated into the script, thereby avoiding use of commercially available software packages.

The only limiting "human factor" in quantifying cells with our software is the definition of the critical objective parameters, such as pixel diameter based on cell size and percentage fill within each circular rim, color channel, and histogram thresholds. Once calibrated to ensure adequate cell capture for each respective label, then an automated batch analysis of a series of images can be efficiently performed. Although there may be a slight over- or under-representation of true RGC counts, automated cell counting using fixed objective parameters is more likely to generate consistent RGC counts upon repeated sampling than using a manual method with considerable potential subjectivity, and, therefore, variability.[31]

Our program provides a useful research tool with a number of attractive features: (1) wide spectrum of automation, including both image optimization and RGC quantification; (2) applicability to a variety of different antigens (validated to date for the RGC-specific labels Brn3a and RBPMS) with accuracy comparable to manual counting and the existing literature; (3) interchangeability in handling both naive and injured retinal wholemounts; (4) ability to differentiate clusters or clumps of cells with acceptable accuracy; (5) "batch processing" function with seamless transfer of tabulated results to a spread sheet application for

translational vision science & technology

61

ease of statistical analysis; and (6) automated whole-retinal analysis with integrated retinal isodensity map generation.

In addition to these features, our software also provides the ability to manually adjust and optimize cell capture for weaker cell labeling by changing histogram parameters, cell size, percentage fill, cell intensity, and adaptive thresholding. Moreover, the accuracy of cell detection can be manually checked by the "link zoom" feature, which enables the user to zoom in on sections to check that exclusion parameters are as accurate as possible.

Comparison of our Novel Software to Existing Automated Counting Software

Danias et al.[10,17] were arguably the first to conceive and validate a freely available software called Image-Tool to provide semi-automated counts of Fluorogold labeled RGCs on rat, and then later mouse, retinal wholemounts. This software, however, requires time-intensive preprocessing steps using separate software (Adobe Photoshop, Adobe Systems, Inc., San Jose, CA) for images prior to generating the automated cell counts.[17] Image preprocessing is integrated into the script of our software, provided that the actual immunolabeling and resultant image capture are of reasonable quality.

The Vidal-Sanz laboratory also developed a script validated for Fluorogold-labeled RGCs on rodent retinal flat mounts and this was later validated for Brn3a-labeling with excellent accuracy (R2 > 0.94) when compared to manual counting.[4,15,29] In addition, they also validated its use in quantifying immuno-labeled photoreceptors.[32] Importantly, this program is also able to distinguish between clusters of cells and automates the image optimization stages. From a mosaic of 154 frames of the retinal whole-mount photographs, retinal isodensity maps were generated using Adobe Photoshop CS 8.0.1 (Adobe Systems, Inc.), IPP (IPP version 5.1 for Windows; Media Cybernetics, Silver Spring, MD), and Sigmaplot (Sigmaplot version 9.0 for Windows; Systat Software, Inc., Richmond, CA) commercial software.[29] The only potential disadvantage to its widespread use is that it requires the commercially available software Image Pro-Plus. Geeraerts et al.[16] developed an ImageJ plug-in to provide semi-automated counts of Brn3a-labelled RGCs on mouse retinal wholemounts with excellent accuracy (r > 0.99) that permitted the generation of retinal isodensity maps integrated into the script. Manual interventions that are required involve the outlining the borders of the retina and excluding

damaged regions / artifacts from the retinal image.[16] We have integrated both whole-retinal analysis and retinal isodensity map generation into our script, which does not require the user to outline the retinal borders. A degree of image optimization is also integrated into our script, to enable the exclusion of small artifacts ("speckles") and background blur. Heavily damaged regions or large artifacts, however, do need to be removed prior.

To our knowledge, Dordea et al.[30] were the first to validate automated RGC counts for Beta-III tubulin and DAPI-labeled RGCs with use of a machine-learning plug-in using CellProfiler open source software. It was estimated that data acquisition was accelerated 10-fold by this automated program. This software requires both an image preprocessing step involving binary contrast enhancement carried out through ImageJ software prior to quantification using CellProfiler, and an initial supervised machine-learning step to ensure accuracy in automated cell recognition for each label.[30]

An open source ImageJ plug-in was developed and validated by Hedberg Buenz et al.[33] for quantifying hematoxylin and eosin-labeled mouse retinal wholemounts (R2 = 0.953 to 0.993). RGCs were identifi-able with reasonable accuracy (83.2%) by using random forest classification based on morphological criteria.[31] Similar to our program, this plug-in initially requires the user to manually calibrate the program with a "training" set of images to ensure accurate RGC detection prior to performing automated RGC counts. Despite using high magnification (200×) photomi-crographs and manually subtracting artifacts from photomicrographs prior to automated counting, some difficulty was encountered with missed nuclei associ-ated with cell clumps or concealment by the nerve fiber layer.[33] Hedberg Buenz et al.[33] also report that the program is cumbersome when used in conjunction with immunohistochemistry or retrograde tracers, thereby limiting its versatility.

Byun et al.[34] also developed an ImageJ plug-in for nuclei detection on transverse retinal sections, which to date has not been validated for use on whole-mounts. Last, Bizrah et al.[35] developed a MATLAB script to automatically quantify apoptotic RGCs in vivo using fluorescent Annexin V labeling with Detec-tion of Apoptosing Retinal Cell (DARC) imaging (r = 0.978, R2 = 0.956). This is particularly attractive as the ability to capture and automatically quantify RGC populations in real-time throughout disease evolution, ex vivo, could provide further robustness to preclinical, and even clinical, trials whereas significantly reducing required sample sizes with repeated sampling, acceler-ating workflow and research output.

Challenges to Counting RGCs

Indistinct cells: Over- or underestimation of RGC counts can potentially lead to erroneous conclusions in animal models of retinal pathology. Our program fundamentally works by separating the cell image from the background image (see Supplementary Fig. S1: Algorithm Development, steps 1–3). By calculating and then removing the background blur, even the faintest cells are observable. When calibrating the program prior to analyzing each immunolabel, the researcher is able to correct for over- or underestimation of RGCs by adjusting the objective parameters and then proceeding to "batch" analyze their image data set.

Our program is able to discriminate cells in clusters with excellent accuracy for Brn3a and RBPMS immunolabels. This is achieved through highlighting the intensity of the boundaries between cells by ensuring the processed image channel intensity occupies the complete intensity range. However, there is still a small window of sampling error whereby a larger cell may be incorrectly counted as two or more separate cells, or vice versa.

Sampling bias: Unless the entire retina is analyzed for RGC quantification, sampling error can arise. RGC density in the rat retina ranges according to location, with the highest density peaking in the most central area ($\sim$3000 cells per mm^2) and lowest in the peripheral retina ($\sim$600 cells per mm^2).[36] However, the spatial distribution of RGCs can vary between rats of the same species and between eyes of the same rat.[17] There may also be sectoral RGC loss in different disease models.[14,37] Therefore, although it is scientifically acceptable to quantify RGCs in predefined areas sampled at a set distance from the optic nerve in hemiretinas or quadrants,[14] this method ultimately accepts that there is variability compared with counting all cells in the retina. Sampling the entire retina is arduous unless automated counting is utilized to expedite the process. Our automated cell counting program can be used to quantify RGCs in the entire retina to permit isodensity map generation and avoid possible sampling bias.

Image quality: Although various preprocessing techniques can be used to fine-tune poorer quality images, optimal image capture is the prerequisite for accurate quantification of any cellular label. Our software has inbuilt image preprocessing capability to remove artifact and background noise and sharpen image quality. It does, however, require images to be homogenously labeled, be reasonably clean without significant large debris obscuring cells, and to be well focused in a single plane. These are obviously technical issues that should be addressed prior to attempting automated quantification of cells with any software, or even manual counting.

Conclusions

Quantifying immunostained RGCs on wholemounts remain an important outcome measure in preclinical animal studies. Manual or semi-automated methods are labor-intensive, time-consuming, and subject to inter- and intra-observer variability. Our automated cell counting software, validated for the RGC specific immunostains Brn3a and RBPMS in rodent retinal wholemounts, accelerates data acquisition and reduces analytical subjectivity. Our automated software demonstrated accuracy and reproducibility in both naïve and injured retinas when compared with manual counting and has the ability to perform whole-retinal analysis with integrated retinal isodensity map generation.

Acknowledgments

References

1. Casson RJ, Chidlow G, Wood JP, Crowston JG, Goldberg I. Definition of glaucoma: clinical and experimental concepts. *Clin Experiment Ophthalmol.* 2012;40:341–349.
2. Peinado-Ramon P, Salvador M, Villegas-Pérez MP, Vidal-Sanz M. Effects of axotomy and intraocular administration of NT-4, NT-3, and brain derived neurotrophic factor on the survival of adult rat retinal ganglion cells: a quantitative in vivo study. *IOVS.* 1996;37:489–500.
3. Thanos S. Specific transcellular carbocyanine-labelling of rat retinal microglia during

translational vision science & technology

injury-induced neuronal degeneration. *Neurosci Lett*. 1991;127:108–112.

4. Nadal-Nicolás FM, Jiménez-López M, Salinas-Navarro M, et al. Whole number, distribution and co-expression of Brn3 transcription factors in retinal ganglion cells of adult albino and pigmented rats. Harvey AR, ed. *PLoS One*. 2012;7:1–16.

5. Kwong JMK, Quan A, Kyung H, Piri N, Caprioli J. Quantitative analysis of retinal ganglion cell survival with RBPMS immunolabeling in animal models of optic neuropathies. *Investig Opthalmology Vis Sci*. 2011;52:9694–9702.

6. Rodriguez AR, de Sevilla Müller LP, Brecha NC. The RNA binding protein RBPMS is a selective marker of ganglion cells in the mammalian retina. *J Comp Neurol*. 2014;522:1411–1443.

7. Surgucheva I, Weisman AD, Goldberg JL, Shnyra A, Surguchov A. γ-Synuclein as a marker of retinal ganglion cells. *Mol Vis*. 2008;14:1540–1548.

8. Jiang S-M, Zeng L-P, Zeng J-H, Tang L, Chen X-M, Wei X. β-III-Tubulin: a reliable marker for retinal ganglion cell labeling in experimental models of glaucoma. *Int J Ophthalmol*. 2015;8:643–652.

9. Thanos S. The relationship of microglial cells to dying neurons during natural neuronal cell death and axotomy-induced degeneration of the rat retina. *Eur J Neurosci*. 1991;3:1189–1207.

10. Danias J, Lee KC, Zamora M-F, et al. Quantitative analysis of retinal ganglion cell (RGC) loss in aging DBA/2NNia glaucomatous mice: comparison with RGC loss in aging C57/BL6 mice. *Investig Opthalmology Vis Sci*. 2003;44:5151–5162.

11. Buckingham BP, Inman DM, Lambert W, et al. Progressive ganglion cell degeneration precedes neuronal loss in a mouse model of glaucoma. *Neurobiol Dis*. 2008;28:2735–2744.

12. Chen H, Wei X, Cho K-S, et al. Optic neuropathy due to microbead-induced elevated intraocular pressure in the mouse. *Investig Opthalmology Vis Sci*. 2011;52:36–44.

13. Schlamp CL, Montgomery AD, Mac Nair CE, Schluart C, Willmer DJ, Nickells RW. Evaluation of the percentage of ganglion cells in the ganglion cell layer of the rodent retina. *Mol Vis*. 2013;19:1387–1396.

14. Mead B, Thompson A, Scheven BA, Logan A, Berry M, Leadbeater W. Comparative evaluation of methods for estimating retinal ganglion cell loss in retinal sections and wholemounts. Badea TC, ed. *PLoS One*. 2014;9:1–9.

15. Nadal-Nicola's FM, Jiménez-López M, Sobrado-Calvo P, et al. Brn3a as a marker of retinal ganglion cells: qualitative and quantitative time course studies in naïve and optic nerve–injured retinas. *Investig Opthalmology Vis Sci*. 2009;50:3860–3868.

16. Geeraerts E, Dekeyster E, Gaublomme D, Salinas-Navarro M, De Groef L, Moons L. A freely available semi-automated method for quantifying retinal ganglion cells in entire retinal flatmounts. *Exp Eye Res*. 2016;147:105–113.

17. Danias J, Shen F, Goldblum D, et al. Cytocarchitecture of the retinal ganglion cells in the rat. *Invest Ophthalmol Vis Sci*. 2002;43:587–594.

18. Markand S, Saul A, Roon P, et al. Retinal ganglion cell loss and mild vasculopathy in methylene tetrahydrofolate reductase (Mthfr)-deficient mice: a model of mild hyperhomocysteinemia. *Investig Opthalmology Vis Sci*. 2015;56:2684–2695.

19. Inman DM, Lambert WS, Calkins DJ, Horner PJ. α-Lipoic acid antioxidant treatment limits glaucoma-related retinal ganglion cell death and dysfunction. Ohlmann A, ed. *PLoS One*. 2013;8:1–17.

20. Soto I, Oglesby E, Buckingham BP, et al. Retinal ganglion cells downregulate gene expression and lose their axons within the optic nerve head in a mouse glaucoma model. *J Neurosci*. 2008;28:548–561.

21. Salinas-Navarro M, Jiménez-López M, Valiente-Soriano FJ, et al. Retinal ganglion cell population in adult albino and pigmented mice: a computerized analysis of the entire population and its spatial distribution. *Vision Res*. 2009;49:637–647.

22. Levkovitch-Verbin H, Quigley HA, Martin KRG, Valenta D, Baumrind LA, Pease ME. Translimbal laser photocoagulation to the trabecular meshwork as a model of glaucoma in rats. *Investig Ophthalmol Vis Sci*. 2002;43:402–410.

23. Ebneter A, Chidlow G, Wood JPM, Casson RJ. Protection of retinal ganglion cells and the optic nerve during short-term hyperglycemia in experimental glaucoma. *Arch Ophthalmol*. 2011;129:1337–1344.

24. Ebneter A, Casson RJ, Wood JPM, Childow G. Microglial activation in the visual pathway in experimental glaucoma: Spatiotemporal characterization and correlation with axonal injury. *Investig Ophthalmol Vis Sci*. 2010;51:6448–6460.

25. Bull ND, Chidlow G, Wood JPM, Martin KR, Casson RJ. The mechanism of axonal degeneration after perikaryal excitotoxic injury to the retina. *Exp Neurol*. 2012;236:34–45.

26. Chidlow G, Wood JPM, Casson RJ, et al. Expression of inducible heat shock proteins Hsp27 and Hsp70 in the visual pathway of rats subjected to various models of retinal ganglion cell injury. Agudo-Barriuso M, ed. *PLoS One*. 2014;9:1–26.

translational vision science & technology

27. Parker RA, Weir CJ, Rubio N, et al. Application of mixed effects limits of agreement in the presence of multiple sources of variability: exemplar from the comparison of several devices to measure respiratory rate in COPD patients. *PLoS One*. 2016;11:1–15.

28. Bland JM, Altman DG. Agreement between methods of measurement with multiple observations per individual. *J Biopharm Stat*. 2007;17:571–582.

29. Salinas-Navarro M, Mayor-Torroglosa S, Jiménez-López M, et al. A computerized analysis of the entire retinal ganglion cell population and its spatial distribution in adult rats. *Vision Res*. 2009;49:115–126.

30. Dordea AC, Bray M-A, Allen K, et al. An open-source computational tool to automatically quantify immunolabeled retinal ganglion cells. *Exp Eye Res*. 2016;147:50–56.

31. Hedberg-Buenz A, Christopher MA, Lewis CJ, et al. Quantitative measurement of retinal ganglion cell populations via histology-based random forest classification. *Exp Eye Res*. 2016;146:370–385.

32. Ortín-Martínez A, Jiménez-López M, Nadal-Nicolás FM, et al. Automated quantification and topographical distribution of the whole population of S- and L-cones in adult albino and pigmented rats. *Investig Opthalmology Vis Sci*. 2010;51:3171–3183.

33. Hedberg-Buenz A, Christopher MA, Lewis CJ, et al. RetFM-J, an ImageJ-based module for automated counting and quantifying features of nuclei in retinal whole-mounts. *Exp Eye Res*. 2016;146:386–392.

34. Byun J, Verardo MR, Sumengen B, Lewis GP, Manjunath BS, Fisher SK. Automated tool for the detection of cell nuclei in digital microscopic images: application to retinal images. *Mol Vis*. 2006;12:949–960.

35. Bizrah M, Dakin SC, Guo L, et al. A semi-automated technique for labeling and counting of apoptosing retinal cells. *BMC Bioinformatics*. 2014;15:169.

36. Sefton AJ, Dreher B, Harvey AR, Martin PR. *The Rat Nervous System*. Fourth Edi. (Paxinos G, Ed.). Elsevier Inc.; 2015.

37. Lei Y, Garrahan N, Hermann B, et al. Topography of neuron loss in the retinal ganglion cell layer in human glaucoma. *Br J Ophthalmol*. 2009;93:1676–1679.

3.1. Supplement 1: Algorithm Development

The code assumes all images are captured as a three channel (red, green, blue - RGB) image where the stained cells to be counted exist within one stain channel only. As the code is not stain dependant, the code is capable of operating on any stain that highlights artefacts in either the red, green or blue colours. For brevity this supplement uses a red stained image (Group 1 data set immunolabelled for Brn3a) to highlight operation of each code Step, but the authors have used the code on green stained images with great success.

The code makes use of the fact that an image fundamentally has three surfaces corresponding to each colour channel, that combine to create the perceived image. The execution of the code depends on determining the pixels of the image that describe cells separate to those pixels that describe background. Data can be extracted from each surface (channel) and used to better understand the overall cell count. An example image is shown in Supplementary Figure 1 with a rectangular subsection highlighted with overlapping cells. The subsection highlighted is a good example of where existing programs would need human intervention to differentiate the cells within the clump. The three surfaces corresponding to the rectangular sub-image are shown in Figure 2 below and used throughout this section.
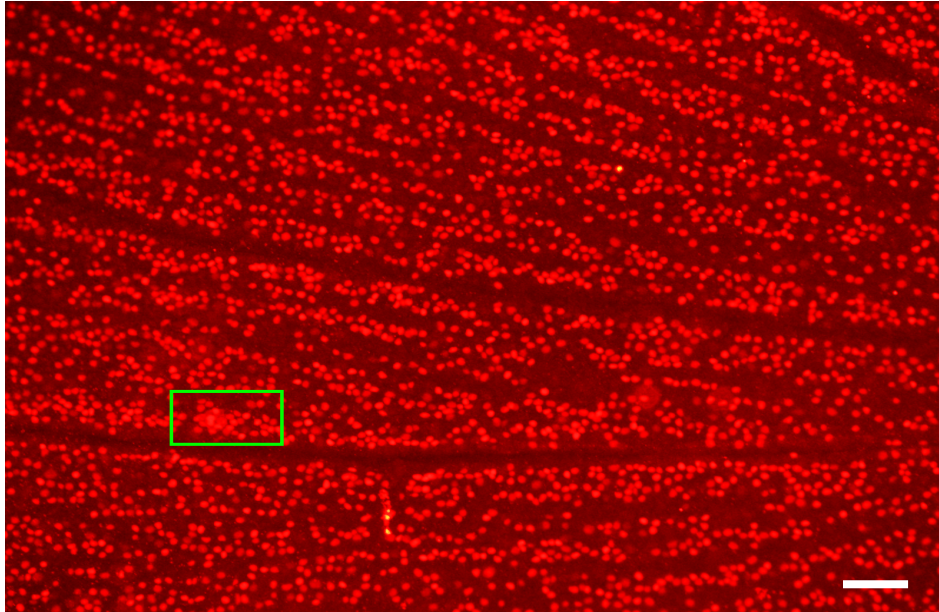
Supplementary Figure 1. Raw Input image showing rectangular area of interest containing overlapped cells. Brn3a immunolabelled central retinal photomicrograph, captured at 10x magnification (Scale bar = 50μm).

Step 1: Artefact subtraction

Step one is dedicated to preparing the image prior to analysis. During this stage any 'speckles' (artefact of artificially high intensity across all three channels) are identified and removed. Speckles are introduced by the image capture device (CMOS or otherwise) when one pixel, across all three channels, incorrectly registers an intense value. Removing speckles is therefore achieved by subtracting non-channel pixel values from the stain channel values.

In Supplementary Figure 2, the introduced speckles are shown as non-zero values in the green and blue channels, while the stain image is shown in the red surface. While the red channel contains all the identified cells as peaks in the surface, the background value floor in the image is greater than the values in the red and blue channels. For reference the background red channel is also irregular and varies from image to image, hence a simple intensity threshold cannot be

applied. This variation in background intensity is due to differences in stain adhesion, lighting, cellular layout and sample thickness.
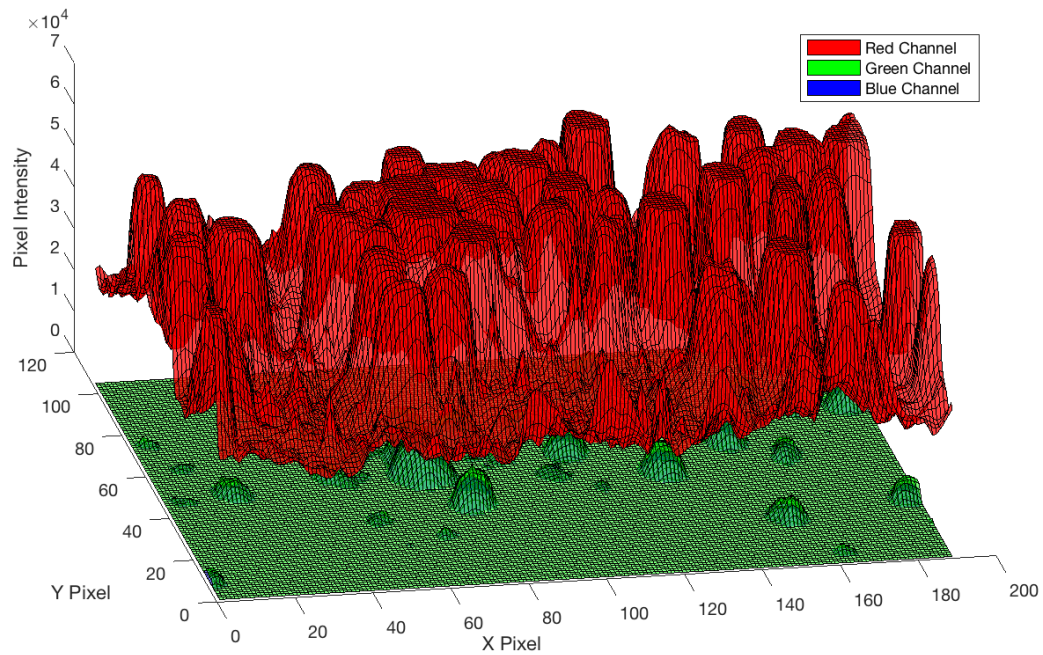
Supplementary Figure 2. Raw Rectangular Sub-image

The resulting subtraction of the non-stain channels are visualised in Supplementary Figure 3 comparing the original three channel image to the speckle free image. The areas of highest intensity are notably dimmer highlighting the boundary between overlapping cells.

Original Image
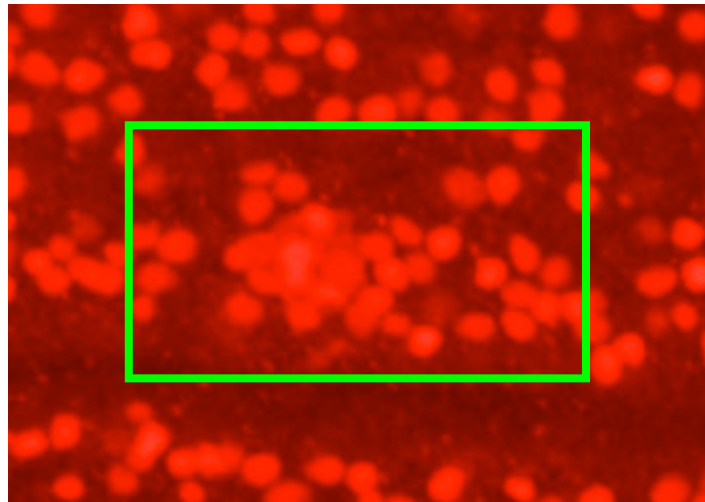
Speckle Free Image
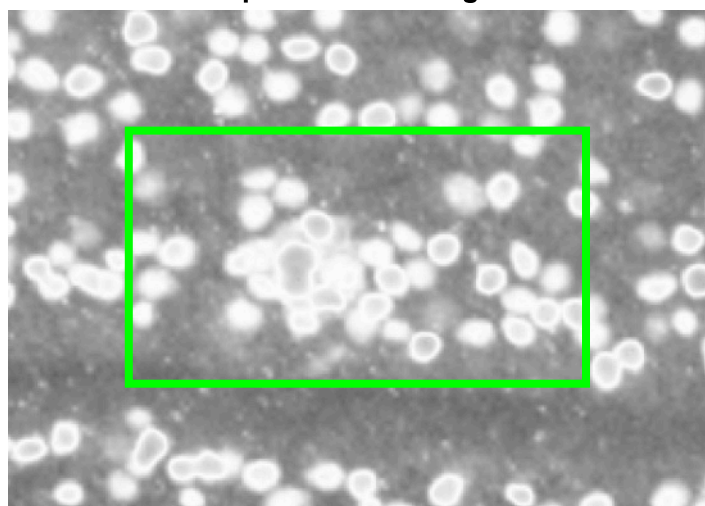
Supplementary Figure 3. Comparison of Raw versus Speckle-Removed Sub-images in zoomed-in section of Brn3a immunolabelled retinal photomicrograph.

The contrast in the stain channel is further enhanced by stretching the image intensities across 98% of the intensity range. The resulting adjustment in channel background intensity is shown

in Supplementary Figure 4 with the new adjusted background intensity contained within the lower third of the image intensity.
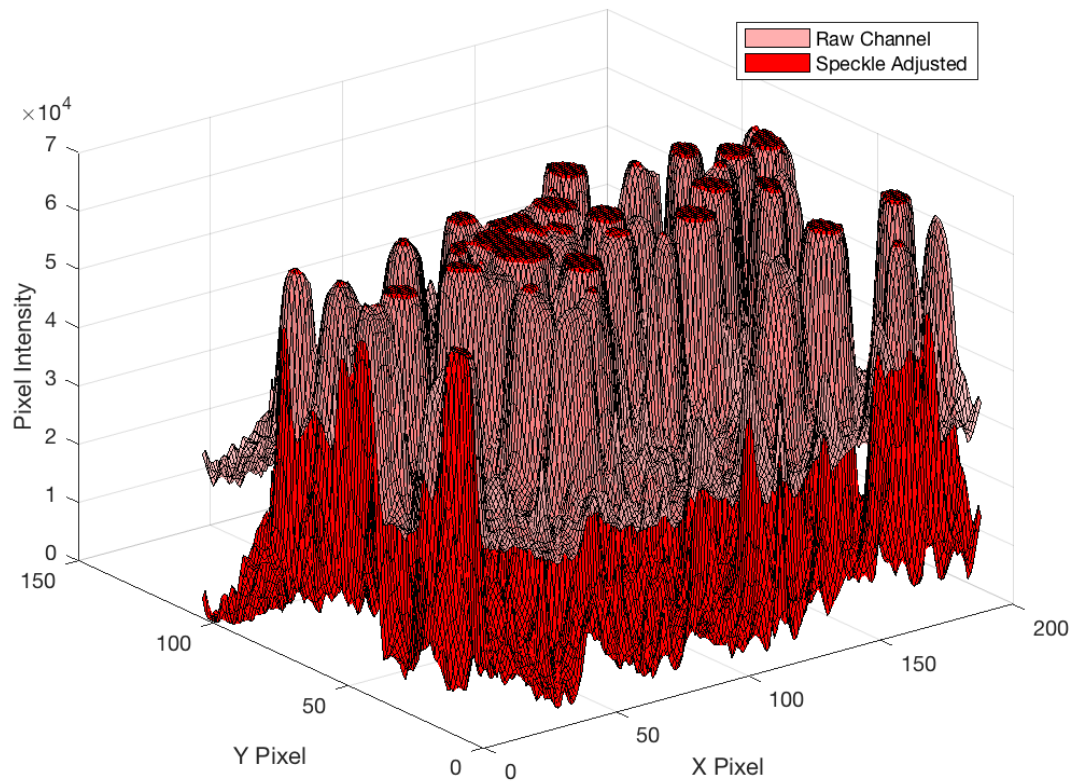
Supplementary Figure 4. Pre- and Post-Speckle and Intensity modification

Background blurring is removed by first calculating a localised Gaussian filtered image that represents a total blurred image. The background blur is then further localised by subtracting the blur from original image using a binary mask generated using Otsu's method that is subtracted from the de-speckled image (Supplementary Figure 5).

Raw Stain Channel

Calculated Background Blur Mask
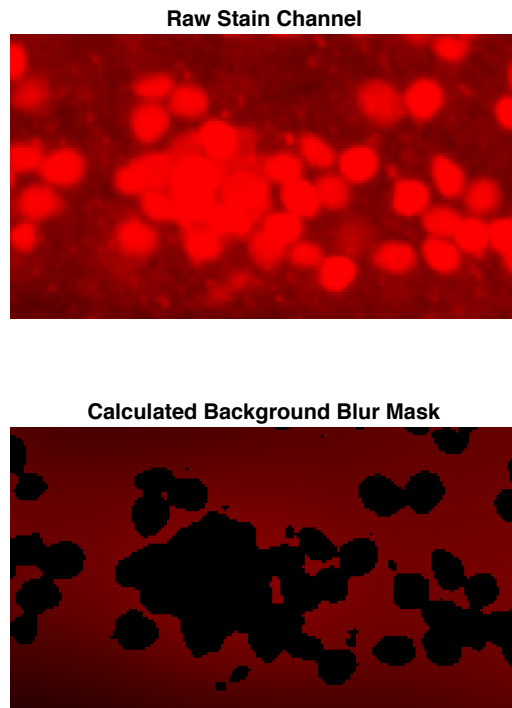
Supplementary Figure 5. Example of isolated Background Mask in zoomed-in section of clumped cells from Brn3a immunolabelled retinal photomicrograph.

The development of the mask has the user configurable option of attempting to account for any non-uniform image intensity by applying an adaptive threshold based on local first-order image statistics. This de-blurring operation has the effect of increasing the contrast of the stained cells from the background. In many cases this process removes all background channel data, highlighting the cells with the maximum intensity as shown in Supplementary Figure 6.
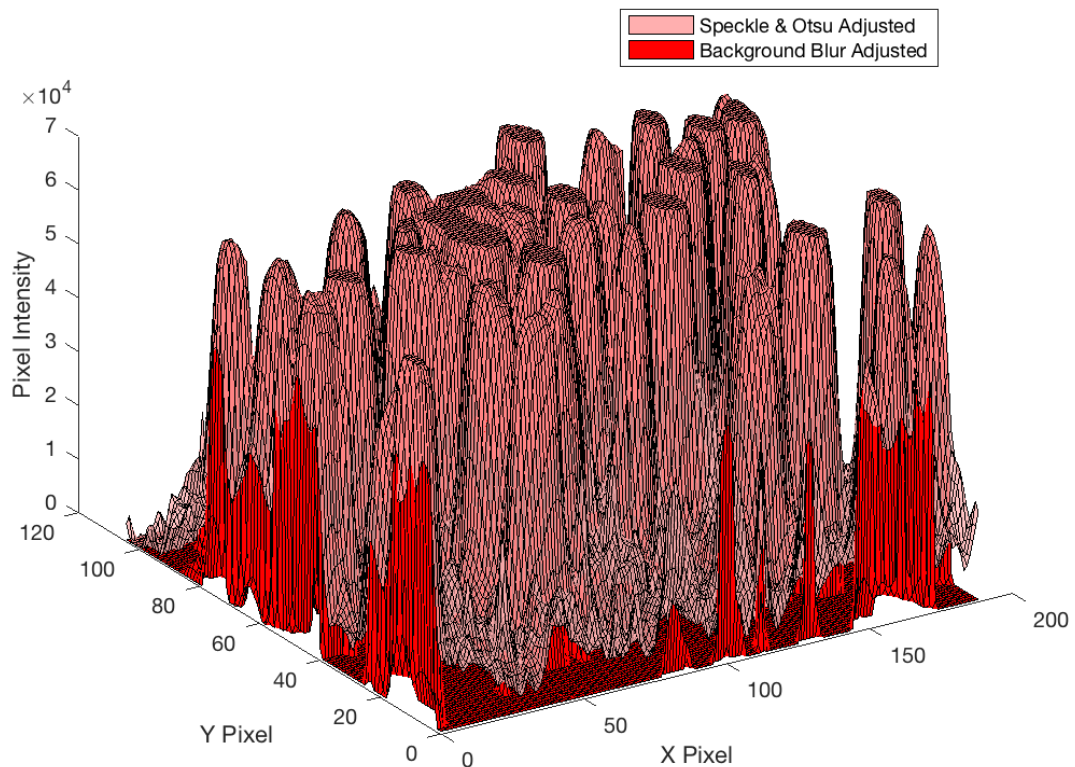
Supplementary Figure 6. Example of background removal in Brn3a immunolabelled photomicrograph.

Step 2: Noise subtraction and histogram analysis

Any remaining noise in the image is identified and removed by measuring the relative image thresholds on the channels not containing any stained cells. This thresholding takes the form of histogram analysis that creates 100 linearly spaced bins between the minimum pixel intensity through to the maximum pixel intensity. Each pixel in the image is then compared to the different bin ranges and placed into the corresponding bin as appropriate. For the non-stain channels, an assumption is made that the stain has worked to only generate colours in the stain channel and hence the majority of the pixel intensities should reside in the lower intensity bins in the histogram. Correspondingly, in the stain channel the object of interest exhibits greater pixel intensities and result in larger number of pixels in the higher intensity histogram bins.

The algorithm identifies where the background noise floor boundary lies by analysing when the stain channel histogram bin value counts exceed those of the non-stain channels. The user can override the automated threshold for more precise control over the threshold cut-off. The calculated background threshold value is shown below in Supplementary Figure 7.
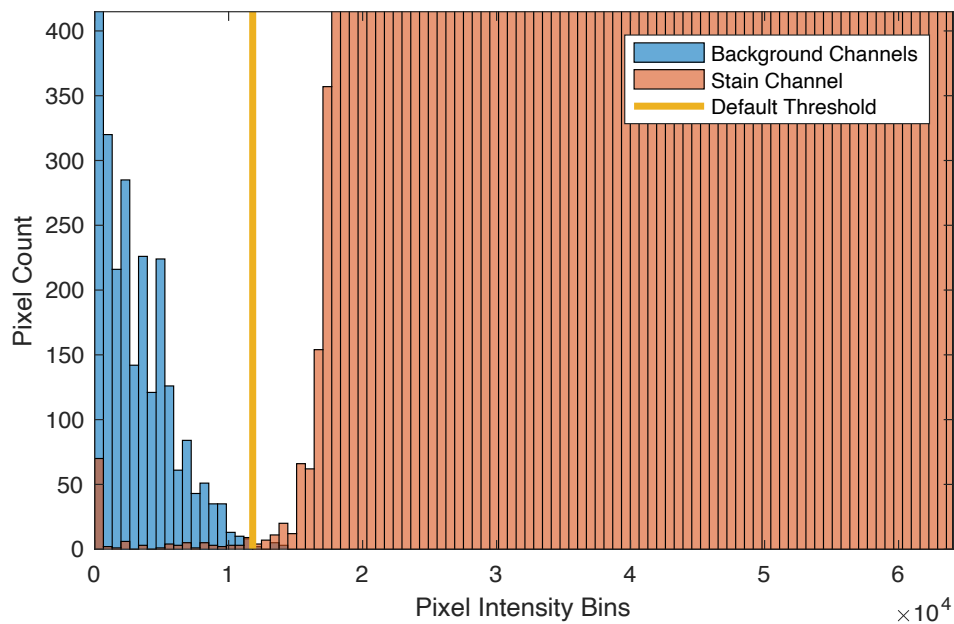
Supplementary Figure 7. Histogram analysis of Brn3a immunolabelled retinal photomicrograph.

Step 3: Adaptive thresholding

Image filtering is performed in the spatial domain to first smooth an image before creating a binary version of the image using an adaptive threshold. The adaptive threshold rebalances lighting across an image thereby bringing into focus areas of an image with lower light levels. Smoothing is achieved by performing image dilation using a disc shaped structured object with a radius of 1 pixel before performing area opening, removing any unconnected object comprised of less than 100 pixels. This operation removes any noise in the image introduced through the filtering operations performed earlier.

Step 4: Circular Hough Transform

A two-stage Circular Hough Transform(248,249) is applied to the image. Cell radii and computational sensitivity are parameters the user can modify to best localise the cells of interest. The cell boundaries are highlighted in Supplementary Figure 8 with a green cap added to each peak within the stain channel surface.
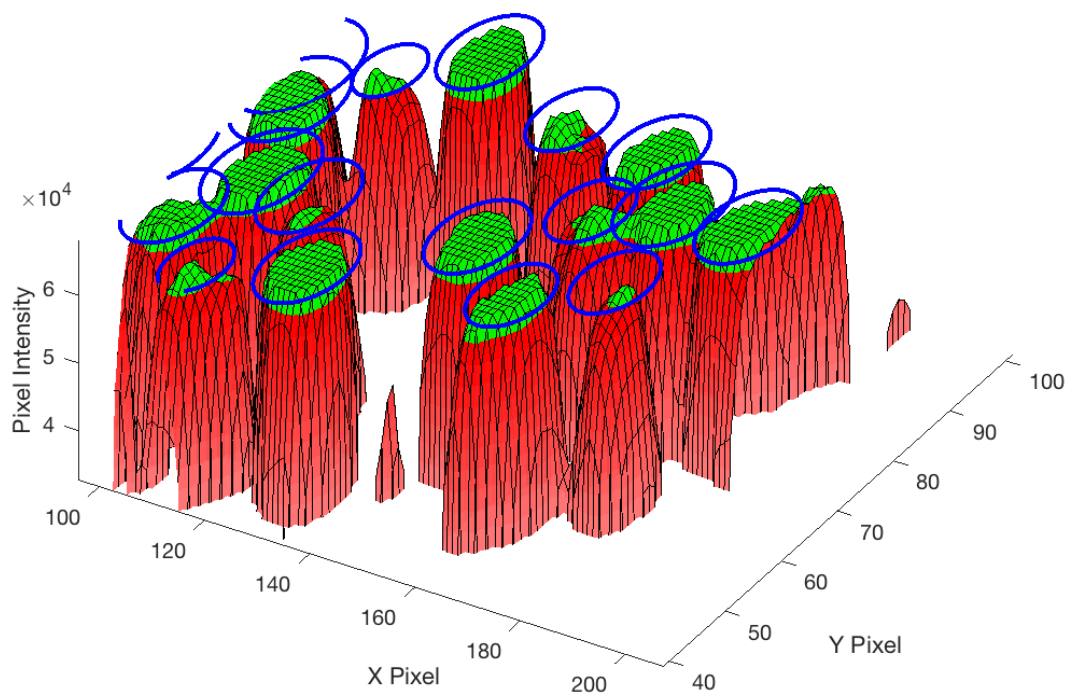
Supplementary Figure 8. Processed Image and Identified Circular Objects in 3D

The original input sub-image and identified cells are shown in Supplementary Figure 9. While barely perceptible to the human eye in the raw image, the computational image processing algorithms isolate and identify overlapping cells with a high degree of success.

Raw Stain Channel
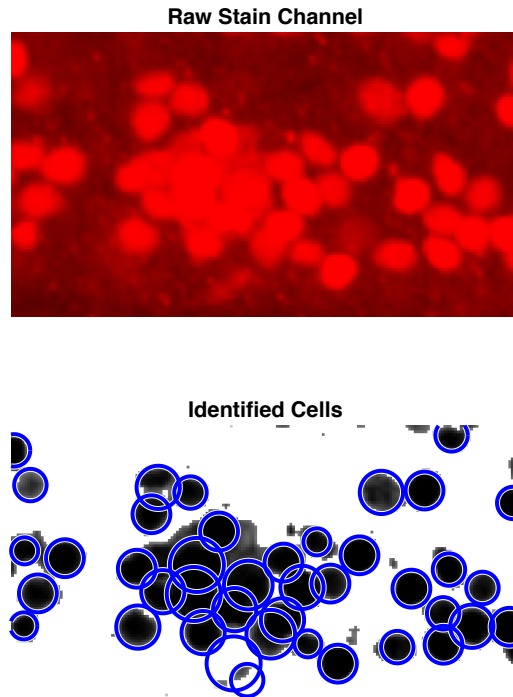
Identified Cells

Supplementary Figure 9. Zoomed-in example of raw stain channel and identified cells as an image from Brn3a immunolabelled photomicrograph.

Step 5: Checking the cell count (Optional)

An optional final step undertakes up to three operations. The first operation integrates the intensity of the image within the proposed circular cell boundary, normalises the value and compares that to the user specified setting. The higher the normalised integrated value the further the cell is away from the background noise (characterise by low intensity values). This has the effect of ensuring only those circular regions that correspond to cells are included in the final cell count.

The second operation calculates the percentage of the proposed circular cell volume that contains non-background values. The Hough transform calculates the centre and radii that correspond to the boundary of circular regions regardless of whether the boundary is complete,

or the region within the circumference is populated. As such, spurious results can emerge where the boundary of a cell is calculated due to the location of noise in the image only. This step checks to see that a minimum percentage of the cell contains non-background values. It is recommended that this value be greater than 50% but less than 70% to account for cells that are not parallel to the image plane.

The third action checks the degree to which any neighbouring cells overlap, and any cells where the difference between the cells centres is less than 75% of the minimum cell radius are removed from the overall cell count.

This final code Step removes cell candidates that were incorrectly identified in Step 4 as shown in the removal of two spurious cells at the bottom centre in Supplement Figure 10.

Raw Stain Channel
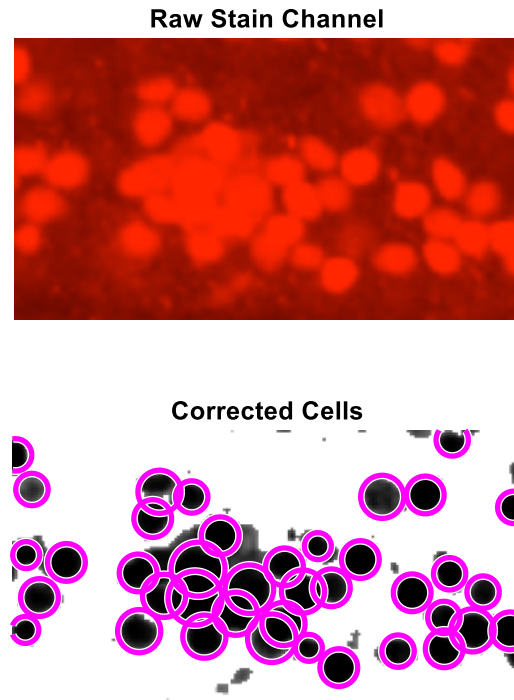
Corrected Cells

Supplementary Figure 10. Zoomed-in example of raw stain channel and corrected cells as an image from Brn3a immunolabelled photomicrograph.

Heat Map Generation

The density of cells across any image is calculated using a Kernel Density Estimate (KDE).

$$\hat{f}_h(x) = \frac{1}{nh} \sum_{i=1}^{n} K\left(\frac{x - x_i}{h}\right)$$

The KDE function calculates the bivariate density of cells across the input image x by applying an underlying gaussian kernel function K at each cell centre. The authors found that to best capture the changes in cell density across an image, the bandwidth h should be set to three times the maximum cell dimension used in Step 4.
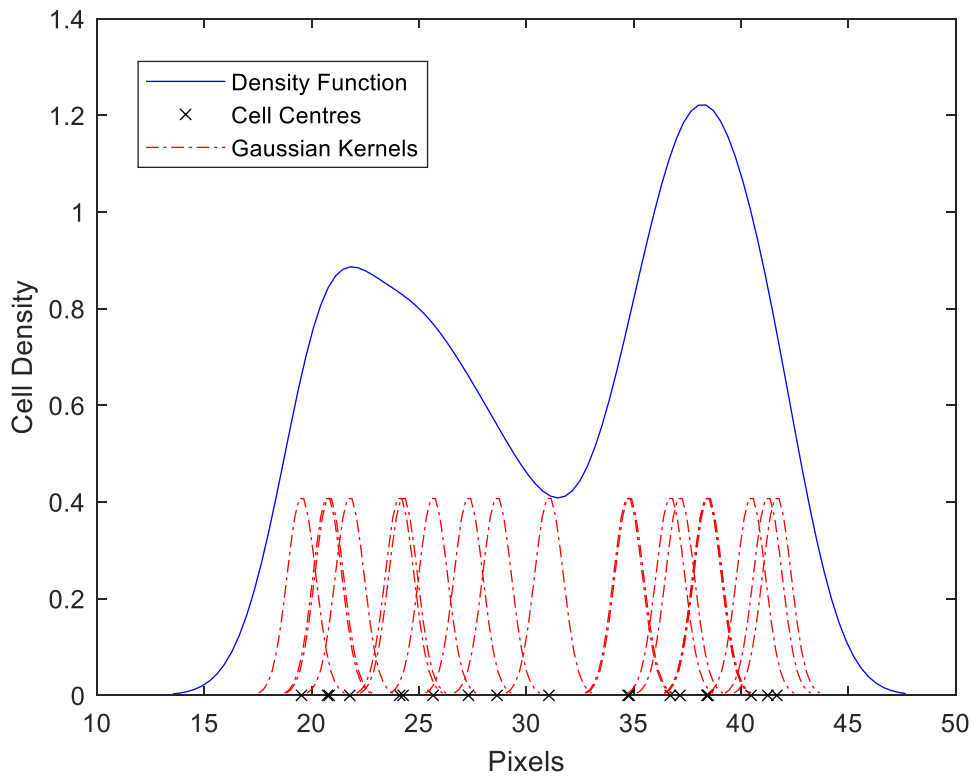
Supplementary Figure 11. KDE generation showing points of higher density resulting in higher Density Function values.

The resultant Density Function (DF) contains only those sections of the image that contain cells with empty areas excluded. The DF is scaled by the number of cells counted in the image and any dimensional data stored in the metadata of the image file.

The use of a KDE ensures the user need not undertake any additional steps when calculating the cell density across any image.

Operating on Large Images

Images stored in multi-file formats such as Hamamatsu (.vms, .vmu, .ndpi) must first be 'unpacked' and their individual image files (.tiff, .jpeg, .png, etc.) exposed(250).

Any image that has a resolution greater than twice the standard 4K resolution is segmented into blocks and each block operated upon in isolation of the rest of the image. Block processing is used to calculate local image (block) quantities and is not used to calculate global image quantities.

Using block processing enables the code to use parallel processing as well as reduce the memory burden of holding large image files in memory. Block processing has shown to reduce the computational time across Steps 1 through 5 of a full retinal image containing 12288 x 12224 pixels at 24-bit image depth from 360 minutes (6 hours) down to 5 minutes.

Displaying large images in the GUI at full resolution or saving full resolution image files cannot be block processed. These steps require a large amount of computer memory and can take a long period of time to execute.

4. Oral pyruvate supplementation protects against neurodegeneration in a rat model of glaucoma.

Dr Chelsea Guymer, Dr John Wood, Dr Glyn Chidlow, Prof Robert Casson

4.1. Abstract

Purpose: Emerging evidence strongly associates retinal ganglion cell (RGC) energetic dysfunction with optic nerve degeneration in glaucoma. Herein we test the hypothesis that oral pyruvate supplementation protects against RGC death in an experimental rat model of induced glaucoma.

Method: Rats were randomly assigned into control (vehicle; n=18) and pyruvate treatment (administered in drinking water, dosed at 500mg/kg/day; n=19) groups. Experimental glaucoma was induced in the right eye of each animal by laser photocoagulation of the trabecular meshwork and episcleral veins at day 0. Intraocular pressure (IOP) was monitored throughout the experiment and all rats were killed on day 14. Retina and optic nerves were processed for quantification of the number of surviving RGCs and axonal injury, respectively. To evaluate the retinal bioavailability of pyruvate, whole retinas were homogenized and the pyruvate level measured using the commercially available kit. To demonstrate the mechanism of pyruvate neuroprotection, mixed retinal cell cultures were subjected to glucose deprivation and oxidative stress in the presence and absence of pyruvate.

Results: There was a clear pressure elevation in the right eye of all animals with no statistically significant difference in peak IOP (p 0.60), IOP exposure (p 0.54), IOP integral (p 0.40) or average IOP (p 0.74) between glaucomatous groups (pyruvate vs. vehicle).

Immunohistochemical labelling of retinal wholemounts with the RGC marker Brn3a demonstrated a significant reduction (p 0.03) in the quantity of RGC loss in the pyruvate supplemented relative to the vehicle-treated glaucomatous eyes. Whilst greater axonal preservation was evident in the pyruvate-supplemented group (74% glaucoma pyruvate vs 63% glaucoma vehicle) this did not reach statistical significance (p 0.124). Quantitative analyses of data from distal optic nerve sections immunolabelled for markers of axonal cytoskeletal damage and microglial activation also indicated white matter protection by pyruvate, which was significant when comparing pyruvate and vehicle glaucomatous groups (p 0.03 and p 0.04 respectively). There was a statistically significant increased bioavailability of pyruvate in the retinas of pyruvate supplemented animals compared to controls (p 0.0034). Retinal cell cultures demonstrated that the presence of pyruvate counteracted the loss of both glia and neurons when subjected to either glucose deprivation or oxidative stress.

Conclusion: Oral pyruvate supplementation reduces RGC loss and consequent optic nerve damage in our rat model of experimental glaucoma. The protecting effect of pyruvate is likely manifest via its ability to act both as a supplemental metabolic substrate and as an antioxidant. These results unveil a potential new therapy for glaucoma with the promise of translation into clinical trials.

4.2. Introduction

Glaucoma is typically, but not exclusively, associated with raised intraocular pressure (IOP), and, elevated IOP remains the most tangible modifiable risk factor in human disease(2,15,140). Yet, despite optimal treatment with pressure lowering therapies, a significant proportion of glaucoma patients will progress, with consequent loss of vision and quality of life(6). A new 'neuroprotective' modality that could augment current treatment and reduce the rate of neurodegeneration to preserve vision throughout life would be a breakthrough.

It is widely accepted that RGC degeneration is the key pathological characteristic of glaucoma(16,32,73,140) and converging evidence has suggested that energy failure in these cells plays a vital role(182–184), in at least some patients. It is also appreciated that in neurodegenerative conditions, glutamate excitotoxicity and generation of reactive oxygen species (ROS) contribute to oxidative damage(157,177,197,199). Prior research in our laboratory has demonstrated 'proof of principle' that RGC survival can be prolonged by increasing the retinal bioavailability of the metabolic substrate glucose (200,204,245,247). This approach offers a degree of neuroprotection, or neurorecovery, to compromised RGCs. Yet, the quest for a more desirable metabolic neuroprotectant, i.e. a compound without the adverse long-term effects of glucose, is warranted. Pyruvate may offer a viable and safe alternative option to glucose.

Pyruvate is a molecule synthesised during the metabolism of glucose, which is readily bioavailable when delivered as an oral supplement and which is also safe(251). It has previously been demonstrated that RGCs are highly oxidative(177,201), that they have the glycolytic machinery to produce pyruvate(252), and that they have a high level of the carrier that transports pyruvate from the cytosol into the mitochondrion for entry into the Krebs

cycle(253). Evidence is accumulating to support the neuroprotective effect of pyruvate in experimental models of neurodegenerative disease, such as ischaemic brain injury, hypoglycaemic brain injury, Huntington's disease, neuroblastoma, closed head injury, and Parkinson's disease(254–262). Interestingly, pyruvate has also been shown to protect against oxidative stress in the mouse lens in culture(263) and attenuate galactose-induced cataract(264). To date, however, there are few studies that have investigated pyruvate neuroprotection in the retina(197,198,257,265).

Whilst the concept of pyruvate neuroprotection is established in the central nervous system, it is essentially novel as regards glaucomatous optic neuropathy. Herein, we provide evidence that RGC axons and their perikarya are significantly protected by high-dose oral pyruvate supplementation in an induced rat model of subacute glaucoma.

The aims of this study were three-fold:

1) To determine whether oral pyruvate supplementation increases the retinal bioavailability of pyruvate.

2) To test the neuroprotective effect of high dose pyruvate supplementation (500mg/kg) in drinking water vs water alone in experimental glaucoma.

3) To determine the neuroprotective mechanism of action of pyruvate using interrogation of mixed retinal cell cultures with glucose deprivation and oxidative stress.

4.3. Materials and Methods

4.3.1. Experimental plan

The study comprised three separate experiments:

Experiment 1: To determine whether oral pyruvate supplementation increases the retinal bioavailability of pyruvate. The primary outcome was retinal pyruvate quantification.

Experiment 2: To test the neuroprotective effect of high dose pyruvate supplementation (500mg/kg) in drinking water vs water alone in experimental glaucoma. Primary outcomes were RGC loss in retinal wholemounts and axon counts in transverse sections of the optic nerve. Secondary outcomes were measurement of microglial activation and neurofilament breakdown in longitudinal tissue sections of the optic nerve (at the level of the optic chiasm).

Experiment 3: To determine the neuroprotective mechanism of action of pyruvate using interrogation of mixed retinal cell cultures with glucose deprivation and oxidative stress. Primary outcomes were quantification of surviving neurons when treated with pyruvate, under conditions of substrate deprivation and oxidative stress.

4.3.2. Animals and procedures

This study was approved by the Animal Ethics Committees of SA Pathology/Central Adelaide Local Health Network and the University of Adelaide (Adelaide, Australia) and conformed with the Australian Code of Practice for the Care and Use of Animals for Scientific Purposes, 2013, and with the ARVO Statement for the use of animals in vision and ophthalmic research.

Adult Sprague-Dawley rats (aged >10 weeks, >230g) were housed in a temperature and humidity-controlled room with 12-hour light and dark cycles. Food and water were provided ad libitum.

Experiment 1: Rats (pyruvate = 10, control = 8) were randomly assigned into control (water only) and high dose pyruvate supplementation (500mg/kg/day in drinking water) groups. They were humanely killed on day 14 by transcardial perfusion with physiological saline under terminal anaesthesia and the retinas dissected. Whole retinas were homogenized and the pyruvate level measured using the commercially available kit (Sigma-Aldrich Pyruvate Assay Kit, Catalog number MAK071).

Experiment 2: Rats (pyruvate = 24, water = 20) were randomly assigned into control (water only) and high dose pyruvate supplementation (500mg/kg/day in drinking water) groups exactly one week prior to glaucoma induction and continued receiving pyruvate throughout the experiment.

Experimental glaucoma was induced at day 0 in the right eye of all animals, leaving the left eye untouched to serve as a control. Rats were anaesthetized with a combination of ketamine hydrochloride, 100mg/kg, and xylazine hydrochloride, 10mg/kg for the procedure. A slightly modified protocol of the method described by Levkovitch-Verbin *et al.*(86) was then used to induce ocular hypertension in the right eye of each animal by laser photocoagulation of the episcleral and circumlimbal vessels. In brief, 135-150 spots of 100μm diameter, 340mW power and 0.6 second duration, were applied the circumlimbal vessels. An additional 35-50 spots, 200μm diameter, 300mW power for 0.6 seconds duration, were delivered to the dominant superior, inferior and temporal episcleral veins whilst leaving the nasal episcleral vein and intersecting nasal margins of the circumlimbal vessel patent.

Elevated IOP over a course of two weeks using this model causes measurable loss of RGCs and their axons, together with activation of retinal and ON glia(200,266). IOP was monitored

using a rebound tonometer (TonoLab; Icare, Espoo, Finland) in bilateral eyes, calibrated for use in rats and performed under light isoflurane anaesthesia, at time points: immediately pre-procedure (baseline), 3 hours post-procedure, days 1, 3, 7, 10, and 14. Rats were killed by cardiac perfusion with physiological saline followed by 10% neutral-buffered formalin (NBF) under terminal anaesthesia. Whole eyes, optic nerves (ON) and chiasms (CHI) were carefully dissected.

Experiment 3: From stocks, litters of pups (1-3 days post-partum) were obtained to derive mixed retinal cell cultures. Cultures were prepared via a sequential trypsin- and mechanical-digest procedure and comprised neurons, glia and photoreceptors, as described previously[265]. Isolated cells were dispensed at 0.5×10^6 cells/mL onto 13mm borosilicate glass coverslips (pre-coated for 15 minutes with 10 µg/ml poly-L-lysine), for immunocytochemistry, or into 96-well plates (CellPlus positive-charge-coated plates, Sarstedt, Adelaide, Australia), for viability assays. Cultures were routinely maintained under saturating humidity at 37°C in Minimal Essential Medium containing 10% (v/v) foetal bovine serum (FBS), 5mM D-glucose, 2mM L-glutamine and penicillin/streptomycin.

Treatments were commenced at 7 days in vitro and were carried out for 24 hours. For nutrient deprivation (ND) experiments, culture medium was replaced with one lacking FBS, glucose, pyruvate and glutamine. Pyruvate was added at appropriate test concentrations (100 µM, 1 mM, 5 mM) and the monocarboxylate transport inhibitor, α-cyano-4-hydroxycinnamic acid (4-CIN), was applied at 10 µM. For application of oxidative stress to cells, medium lacking FBS, glucose and pyruvate but containing 2 mM L-glutamine was used. Glutamine was present in this case because removal of all nutrients caused catastrophic death of all cells within 2-4 hours and this amino acid has been shown to support neuron survival in vitro[267]. Oxidative stress

was established by incubating cells with tert-butylhydroperoxide (t-bH) for 24 hours (1 µM to 250 µM). In some cases, test compounds were co-applied: pyruvate (1 mM), the antioxidant, 6-hydroxy-2,5,7,8-tetramethylchroman-2-carboxylic acid (trolox, 100 µM), 4-CIN (10 µM). When cultures were to be used for immunocytochemistry, cells on coverslips were fixed for 10 minutes with 10% (w/v) neutral buffered formalin containing 1% (v/v) methanol. For viability assessment using the 3-(4,5-dimethylthiazol-2-yl)-2,5-diphenyltetrazolium bromide (MTT) assay, for the last hour of the incubation, medium and test compounds were removed and new medium free of potentially-confounding dead cells/cell debris was applied along with 0.5 mg/ml MTT. After one hour, medium was removed from wells again and remaining cells solubilised with dimethyl sulphoxide (DMSO) before colorimetric absorbance was determined at 570 nm (with 630 nm reference).

4.3.3. Measurement of retinal pyruvate

Saline-perfused whole retinas were homogenised in the pyruvate assay buffer. Samples were centrifuged at 13000 x g for 10 minutes to remove insoluble material. Samples were deproteinized with a 10 kDA MWCO spin filter prior to addition to the reaction to avoid lactate dehydrogenase converting pyruvate to lactate. Samples were then stored at -70°C. Thawed samples were mixed with reagent (pyruvate assay buffer 46µL, pyruvate probe solution (colorimetric) 2µL, and pyruvate enzyme mix 2µL) and incubated for 30 minutes at room temperature. Absorbance was measured at 570nm (A_{570}) for colorimetric assay.

Background values (i.e. the value obtained for the 0 pyruvate standard) were subtracted from all readings. The pyruvate concentration was calculated using the formula: $S_a/S_v = C$ where S_a = amount of pyruvate in unknown sample (nmole) from standard curve, S_v = Sample volume

(μL) added to reaction well, C = Concentration of pyruvate in sample. The amount of pyruvate present in the samples was determined from the standard curve.

4.3.4. Tissue Processing

Whole eyes, distal optic nerves and chiasms were placed in 10% NBF for 24 hours following dissection. Chiasms and distal optic nerves were processed for routine paraffin-embedded (longitudinal) sections and 4μm tissue sections were cut for immunohistochemistry. Following fixation, eyes were dissected into posterior eye-cups. Retinas were removed and prepared as flattened wholemounts by making another four radial cuts. A short piece of proximal ON from the right treated eye of each animal, 1.5mm behind the globe, was removed for resin processing. ONs were fixed by immersion in 2.5% glutaraldehyde with 4% paraformaldehyde in 0.1M phosphate buffer, pH 7.4 for at least 24 hours. ONs were then placed in osmium tetroxide in saline overnight and washed with cocadylate buffer at room temperature. ONs were subsequently dehydrated in graded alcohols and embedded in epoxy resin for transverse sectioning. An ultramicrotome was used to cut sections at 1μm, which were then mounted on glass slides, and enhanced with osmium tetroxide-induced myelin staining using 1% toluidine blue.

4.3.5. Immunohistochemistry

4.3.5.1. Retinal wholemounts

Wholemounts were washed in PBS, before being permeabilised with PBS containing 1% Triton-X (PBS-T), and subsequently blocked in PBS containing 1% Triton-X and 3% normal horse serum (NHS-T). The wholemounts were then incubated with primary anti-goat Brn3a (Table 1) antibody in PBS containing 1% Triton-X and 3% NHS overnight at 4°C. On day 2, retinas were washed for 1 hour at room temperature in PBS-T, then incubated overnight at 4°C

with AlexaFluor-594 conjugated secondary antibody (1:250; Invitrogen, Carlsbad, CA) diluted in NHS-T. Finally, retinas were washed in PBS for 1 hour at room temperature prior to mounting with the RGC side facing up using anti-fade mounting medium (Dako, Botany Bay, New South Wales, Australia).

4.3.5.2. Chiasms and Distal ONs

Tissue sections were deparaffinised and treated with 0.5% hydrogen peroxide to block endogenous peroxidase activity. The sections were then microwaved in 10mM citrate buffer (pH 6.0) for 10 minutes at 95-100°C to achieve antigen retrieval. Tissue sections were then blocked in phosphate-buffered saline containing 3% normal horse serum, incubated overnight at room temperature in primary antibody (Table 1). Sections were then incubated in biotinylated anti-mouse secondary antibody (1:250; Vector, Burlingame, CA), followed by streptavidin-peroxidase conjugate (1:1000). Colour development was achieved by 3'-, 3'-diaminobenzidine. Sections were counterstained with haematoxylin, dehydrated, cleared in histolene and mounted in DPX. Confirmation of the specificity of antibody labelling was judged by the morphology and distribution of the labelled cells, by the absence of signal when the primary antibody was replaced by isotype/serum controls, and by comparison with the expected staining pattern based on our own, and other, previously published results. All of the antibodies employed in the current study have previously been validated for use.

4.3.5.3. Retinal cell cultures

Fixed cells were permeabilised in 0.1% Triton X-100 (v/v) in phosphate buffered saline (PBS; 137 mM NaCl, 5.4 mM KCl, 1.28 mM NaH_2PO_4, 7 mM Na_2HPO_4; pH 7.4) for 15 minutes and then blocked in 3.3% (v/v) horse serum in PBS (PBS-HS). Primary antibodies were appropriately diluted in PBS-HS and applied to coverslips overnight at room temperature in a

moist chamber (Table 1). After overnight incubation, coverslips were washed in PBS and then labelling was completed by successive incubations with appropriate biotinylated secondary antibody (1:250) and fluorescent AlexaFluor-conjugated (488, green; 594, red) streptavidin (1:500). Nuclear counterstaining was achieved with a 5-minute incubation between PBS washes with 500ng/mL 4′,6-diamidino-2-phenylindole (DAPI). In the case of double-labelling of cultures by two antibodies, one was developed as mentioned and the other concurrently with an appropriate secondary species-specific antibody directly linked to the opposite coloured Alexafluor fluorescent label.

Table 1. Primary antibodies

Target	Host	Clone / Cat# No.	Dilution	Source
Brn3a	Goat	Sc-31984	1:600	Santa Cruz Biotechnology Inc, Santa Cruz, California
ED1	Mouse	MCA342R	1:500	AbD Serotec, Oxford, England
SMI-32	Mouse	SMI32-R	1:10,000	Covance, Princeton, USA
Calretinin	Mouse	MAB1568	1:1000	Millipore
GABA	Rabbit	A2052	1:2000	Sigma
GFAP	Rabbit	ZO334	1:10000	Dako
Rhodopsin	Mouse	Ret-P1*	1:5000	Abcam
βIII-tubulin	Rabbit	D65A4*	1:1000	Cell Signalling Technology
Vimentin	Mouse	V9*	1:10000	Dako

4.3.6. Image acquisition and quantification

All analyses were conducted in a blinded fashion. For quantification of RGC survival, left retinas served as controls. For quantification of axon counts and microglial activation/neurofilament breakdown, left optic nerves served as controls.

4.3.6.1. RGC counts on retinal wholemounts

Retinal wholemounts were examined under a fluorescence microscope (BX-61; Olympus, Mount Waverly, Victoria, Australia) equipped with a scientific grade, cooled CCD camera. Central and peripheral images (700 x 525μm, captured at 10x magnification) were taken from the superior, inferior, nasal and temporal quadrants.

Retinal ganglion cell counts were performed using the automated software as described in Chapter 3. In short, the software was calibrated for Brn3a immunohistochemical label to ensure that all images were analysed using the same objective parameters set by the user to optimise cell capture. Each immunolabelled image was then run through the program and the corresponding map of the cell count was visually checked to ensure adequate cell capture. For any images of suboptimal quality (for example, in the case of heavily damaged retina), cell counts were manually performed.

4.3.6.2. Axon counts on transverse sections of the proximal ON

Axon counts of toluidine blue-stained resin cross sections were performed using the 'fixed pattern sampling method' described by Ebneter *et al.*(268). In brief, oil-immersion photomicrographs were taken in five defined areas (centre of the ON and four peripheral images captured at 12, 3, 6, and 9 o'clock position by aligning the microscope visual-field edge with the margin of the ON) of each ON cross-section using the 100x magnification objective.

The sampled area corresponded to approximately 6% of each entire ON cross section. Images were contrast-enhanced, and each axon with a single, intact myelin sheath was counted using a macro-routine written for ImageJ. The weighted average axon counts of the five photomicrographed images were then used to estimate the number of surviving axons in the total ON. To calculate the estimated axonal loss, the axon counts of treated right ONs were compared to control left ONs.

4.3.6.3. Distal ONs

For each antigen, immunohistochemistry was performed using one section of mid ON and one section of distal ON adjacent to the optic decussation. One photomicrograph (175 x 131.25µm) from each location covering the entire width of the nerve was taken using the 20x microscope objective. Measurements from one animal were averaged and treated as an independent data point. For counterstained sections, colour deconvolution was applied to extract the 3'-,3'-diaminobenzidine staining. After thresholding, microglial activation (labelled with ED1) and neurofilament degeneration (labelled with SMI-32) were quantified as a percentage of area stained per image, using ImageJ Software package platform (imagej.net, version 2.0.0-rc-43/1.51q).

4.3.6.4. Retinal cell cultures

Quantification of immunocytochemistry was achieved by manually counting labelled cells for each antibody in five fields per coverslip, averaged, rounded to the nearest integer and this became a single determination. Similar counting on separate coverslips from "n" different cultures constituted "n" determinations. In the case of antibodies that labelled large numbers of over-lapping cells (e.g. tau) or cells that were not easily distinguished from each other (e.g. vimentin), five individual images were recorded from each coverslip and Image J was used to

quantify labelling level per image. The number of separate determinations was calculated as before. All data were correlated and converted to percentages of the mean untreated control value.

4.3.7. Statistical Analysis

Our hypothesis was that short-term oral pyruvate supplementation would protect RGC axons and their somata. Complementary outcomes were the analysis of the optic nerve and retina. Where single groups were being compared, an unpaired t test was used if parametric assumptions were met. Where parametric assumptions were not met, permutation tests were used to calculate an exact p value using R statistical Software (R Core Team (2017). R: A language and environment for statistical computing. R Foundation for Statistical Computing, Vienna, Austria. URL https://www.R-project.org/). Where multiple groups were compared, a one-way ANOVA was employed, with post-hoc Tukey-Kramer test. Number of determinations were recorded for each test, where applied.

4.4. Results

4.4.1 Retinal Pyruvate Concentration

The bioavailability of pyruvate in the retinas of both control rats and pyruvate-supplemented rats was determined using a commercially available kit. Given that experimental glaucoma would not be expected to change the overall bioavailability of pyruvate in the retina, data from both left (normotensive) and right (ocular hypertensive) retinas of each animal were pooled for final analysis. As shown in figure 1, there was a statistically significant (p 0.0034 by unpaired two-tailed t test) increased bioavailability of pyruvate in the retinas of pyruvate supplemented animals (4.891 ± 1.025 ng/µL) when compared to controls (0.615 ± 0.277 ng/µL).
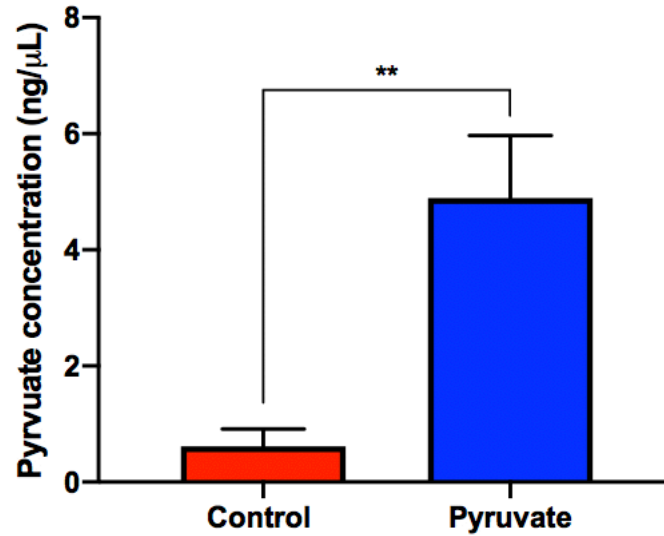
Figure 1. Retinal pyruvate bioavailability. Data represent mean±SEM, where n = 8 (control) and n = 10 (pyruvate). [**]p <0.01 by exact unpaired two-tailed t test (control versus pyruvate).

4.4.2 IOP Profiles

To characterise IOP profiles for each rat peak IOP, IOP exposure (positive IOP integral) and the IOP integral were calculated using the following formulas:

$$\text{Positive IOP Integral} = \sum_{i=1}^{k} (t_i - t_{i-1}) \times \tfrac{1}{2} \times [(IOP_R - IOP_L)_{ti} + (IOP_R - IOP_L)_{ti-1}]$$

$$\text{IOP Integral} = \sum_{i=1}^{k} (t_i - t_{i-1}) \times \tfrac{1}{2} \times (IOP_{ti} + IOP_{ti-1}),$$

where t_i indicates the time point i (in days), IOP_R, IOP in the right eye; and IOP_L, IOP in the left eye(200). IOP peak and integral values are summarised in Table 2 and 3, and average data summarised in Table 4 and Figure 2.

Table 2. Peak IOP and IOP exposure in glaucomatous rats

	Peak IOP (mm Hg-Days)	IOP Exposure (mm Hg-Days)

Glaucoma Pyruvate (n = 18)	41.1 ± 10.5	130.7 ± 69.0
Glaucoma Vehicle (n = 19)	42.6 ± 6.6	116.4 ± 71.0
P value	0.599	0.538

IOP exposure (positive integral) represents the difference in area under the curve of right glaucomatous eyes and left normotensive (control) eyes in each group, calculated for each animal. Data represent mean ± SD. P values were calculated as the comparison between glaucomatous pyruvate and vehicle experimental groups (unpaired, two-tailed t test).

Table 3. IOP integral in control and glaucomatous rats

	Glaucoma Pyruvate (n = 18)	Glaucoma Vehicle (n = 19)	Control Pyruvate (n = 18)	Control Vehicle (n = 19)
IOP Integral (mmHg-Days)	286.0 ± 71.8	306.7 ± 74.5	155.2 ± 31.0	190.3 ± 34.9
P value	0.395		0.003	

IOP integral represents the area under the curve of right glaucomatous eyes in each group, calculated for each animal. Data represent mean ± SD. P values calculated as the comparison between glaucomatous pyruvate and vehicle experimental groups (unpaired, two-tailed t test).

IOPs were first assessed as an independent variable and subsequent analysis controlled for IOP to ensure there was a satisfactory and consistent pressure rise in all animals. Outliers were eliminated, namely 6 pyruvate animals with the lowest cumulative IOPs and one vehicle

glaucoma animal with an aberrantly high IOP profile. This was performed in a blinded fashion prior to examining immunohistochemistry data.

Hence n = 18 pyruvate and n = 19 vehicle treated animals were included for subsequent analysis, resulting in closer correlation of IOP profiles to ensure that there was no statistically significant difference in mean IOP elevations between the treatment and control groups across all time points (*p* 0.79 glaucoma pyruvate vs vehicle groups, *p* 0.16 normotensive pyruvate vs vehicle groups determined via an unpaired two-tailed student's t-test).

Table 4. Mean IOP profiles (mm Hg)

	Baseline (0 hours)	3 hours	1 day	3 days	7 days	10 days	14 days
Glaucoma Pyruvate (n = 18)	11.7	36.2	27.3	21.8	20.1	18.2	11.8
Glaucoma Vehicle (n = 19)	10.3	37.8	32	25.6	19.7	17.1	13.9
Normotensive Pyruvate (n = 18)	9.7	10.8	11.3	12.0	12.3	10.7	9.3
Normotensive Vehicle (n = 19)	9.3	11.1	11	14.6	14.5	13.9	11

Data represent mean IOP (mmHg) of control (left) and glaucomatous (right) eyes in vehicle and pyruvate supplemented groups.
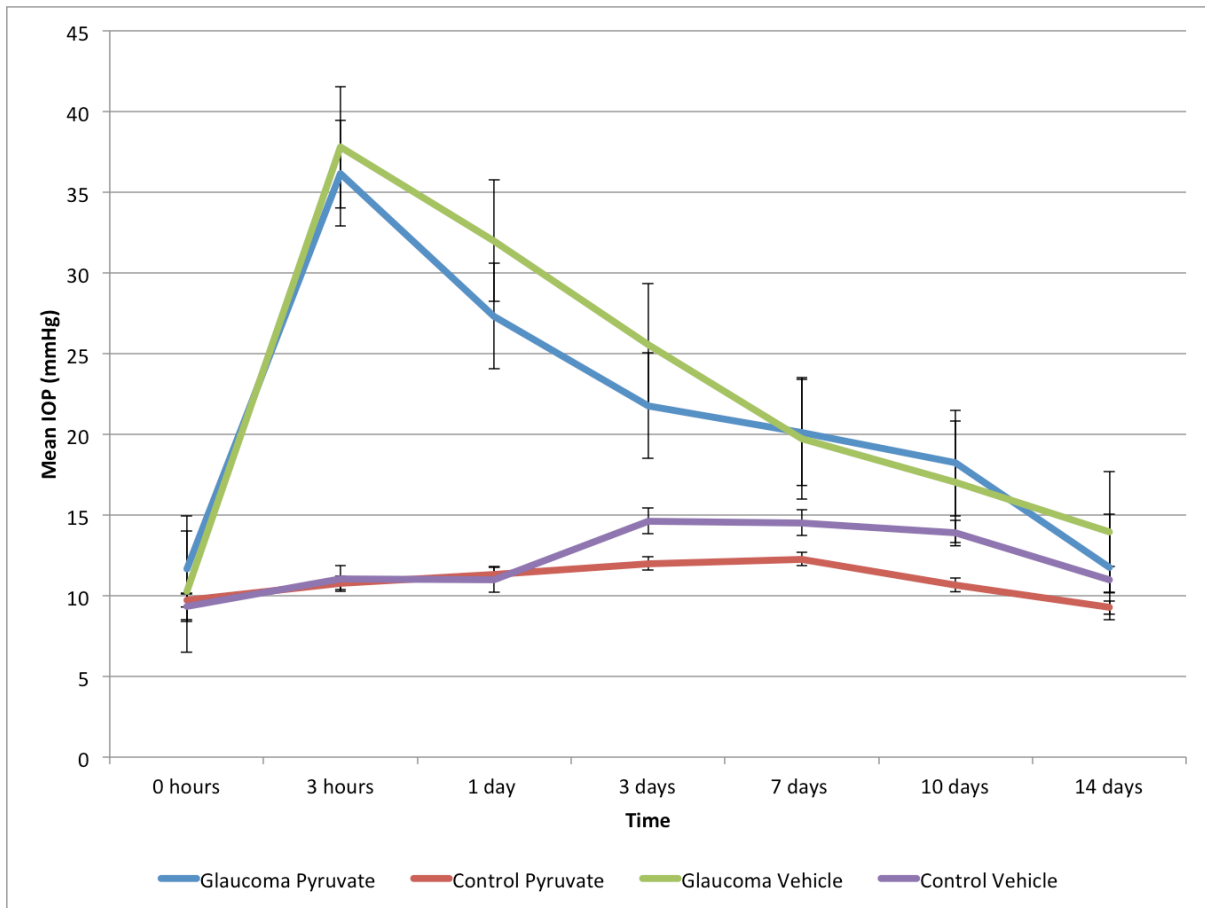
Figure 2. Mean IOP (mmgHg) over time, where n = 18 (glaucoma pyruvate and control pyruvate groups) and n = 19 (glaucoma vehicle and control vehicle groups).

4.4.3. RGC counts in retinal wholemounts

Survival of RGCs was the primary retinal outcome of this study. This was assessed by counting Brn3a-positive cells in retinal wholemounts. Brn3a is a transcription factor down-regulated prior to RGC death and has been demonstrated to be a highly reliable marker for quantification of RGC survival in models of RGC degeneration(107,108,120).

Representative immunohistochemistry images are shown in Figure 3 and the overall results are provided in Table 5 and 6. The box plot (Figure 4) summarises the total RGC Brn3a-labelled counts per sampled retina. Pyruvate afforded statistically significant preservation of Brn3a-labelled RGC counts per sampled retina (*p* 0.03 using unpaired two-tailed t test) and protection from RGC loss in our model of glaucoma (*p* 0.04 by unpaired two-tailed t test).
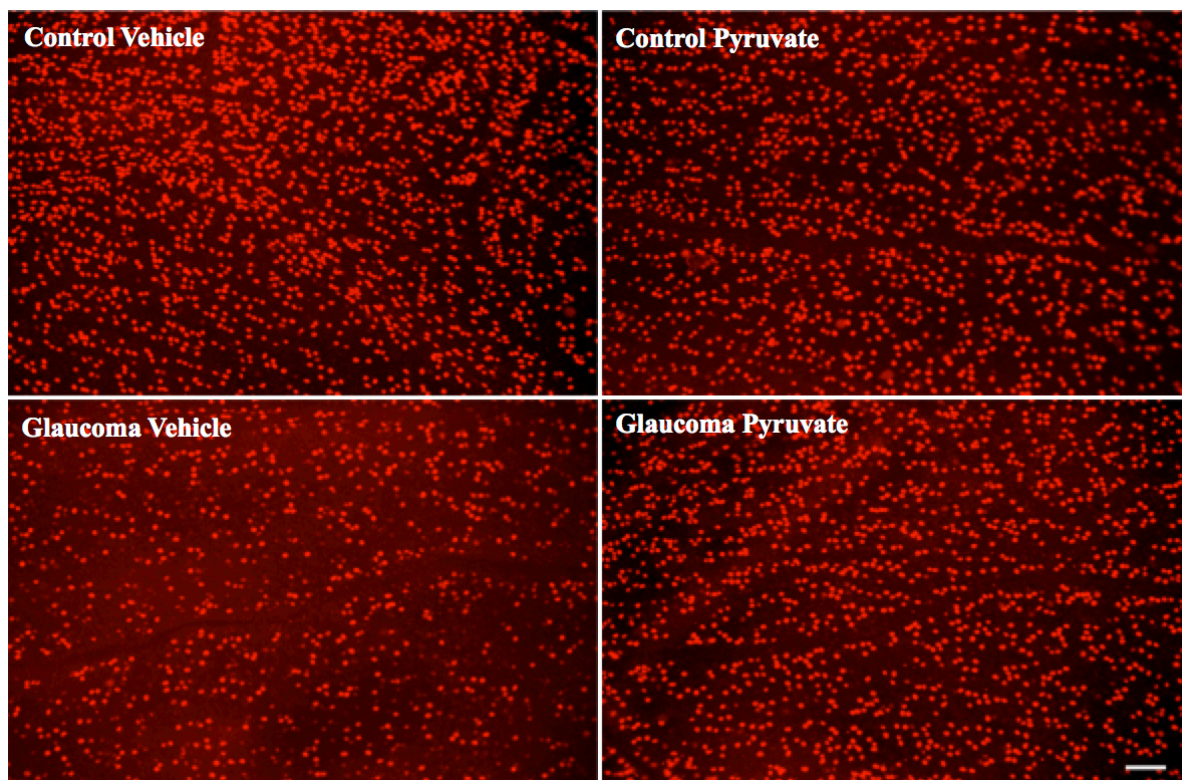
Figure 3. Representative immunofluorescence photomicrographs of Brn3a-labelled RGCs in wholemount retinas. Scale bar = 50μm.

Table 5. Average Brn3a-labelled RGC counts per sampled retina

	Control Pyruvate	Control Vehicle	Glaucoma Pyruvate	Glaucoma Vehicle
Brn3a labeled RGC count	16973±179.1	16343±270.2	12848±611.3	9734±1213.2
P value		0.07		0.03

Data represent Mean ± SEM, where n = 18 (pyruvate) and n = 19 (vehicle). P value was calculated using an unpaired two-tailed t test.

Table 6. The effect of pyruvate on glaucoma induced RGC loss

Experimental Group	Brn3a-labelled RGCs loss (%)
Glaucoma pyruvate	24.3 ± 3.6
Glaucoma vehicle	42.5 ± 7.5
P value	0.04

Data represent Mean ± SEM expressed as a percentage, where n = 18 (pyruvate) and n = 19 (vehicle). The loss of RGCs was calculated from the average difference between control (left) and glaucomatous (right) Brn3a-labelled RGC counts, expressed as a percentage. *p* value was calculated using an unpaired two-tailed t test.

Figure 4. Box Plot summarising Brn3a-labelled RGC total cell counts per sampled retina. Data represent Mean ± SEM, and 5-95th percentiles. n = 18 (glaucoma pyruvate and control pyruvate groups) and n = 19 (glaucoma vehicle and control vehicle groups). $^{*}p <0.05$ by unpaired two-tailed t test (glaucoma vehicle versus glaucoma pyruvate).

Sectoral analyses were also performed of Brn3a-labelled wholemounts. Representative immunofluorescence photomicrographs are shown in Figure 5. As demonstrated in Table 7 and Figure 6, there was no marked sectoral bias in protection afforded by pyruvate.

A. Inferior Quadrants

Control Vehicle

Control Pyruvate

Glaucoma Vehicle

Glaucoma Pyruvate

B. Superior Quadrants

Control Vehicle

Control Pyruvate

Glaucoma Vehicle

Glaucoma Pyruvate

C. Nasal Quadrants

Control Vehicle

Control Pyruvate

Glaucoma Vehicle

Glaucoma Pyruvate

D. Temporal Quadrants

Control Vehicle

Control Pyruvate

Glaucoma Vehicle

Glaucoma Pyruvate

Figure 5. Representative immunofluorescence photomicrographs of Brn3a-labelled RGCs in wholemount retinal quadrants (A. Inferior, B. Superior, C. Nasal, D. Temporal). Scale bar = 50μm.

Table 7. Average Brn3a-labelled RGC counts per sampled retinal quadrant

	Control Pyruvate	Control Vehicle	Glaucoma Pyruvate	Glaucoma Vehicle
Inferior quadrant	4149±82.9	3929±142.0	3238±166.5	2407±298
P value		0.20		0.02
Superior quadrant	4210±96.5	4071±125.1	3102±195.8	2420±342.0
P value		0.39		0.10
Nasal quadrant	4220±72.4	4038±108.1	3108±166.6	2545±301.9
P value		0.18		0.12
Temporal quadrant	4394±130.7	4305±122.6	3400±194.9	2376±386.7
P value		0.62		0.03

Data represent Mean ± SEM, where n = 18 (pyruvate) and n = 19 (vehicle). P value was calculated using an unpaired, two-tailed t test.
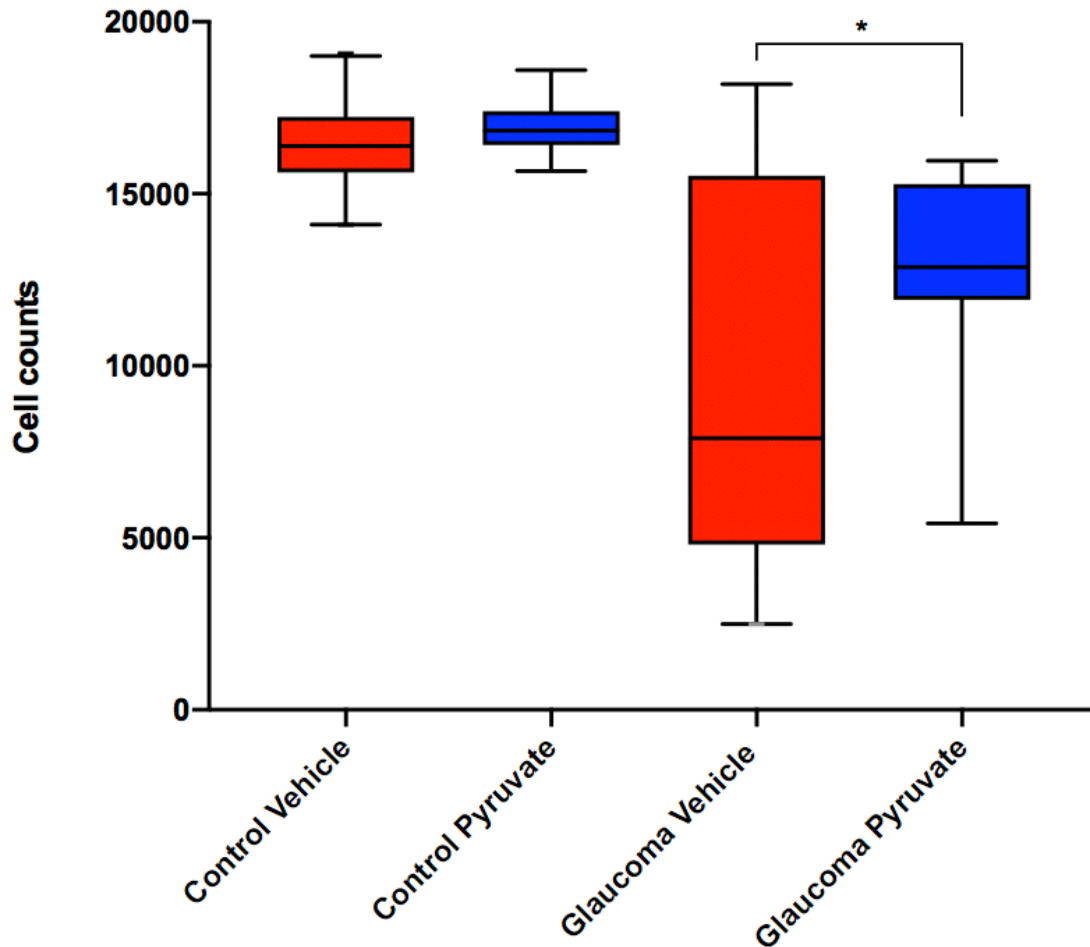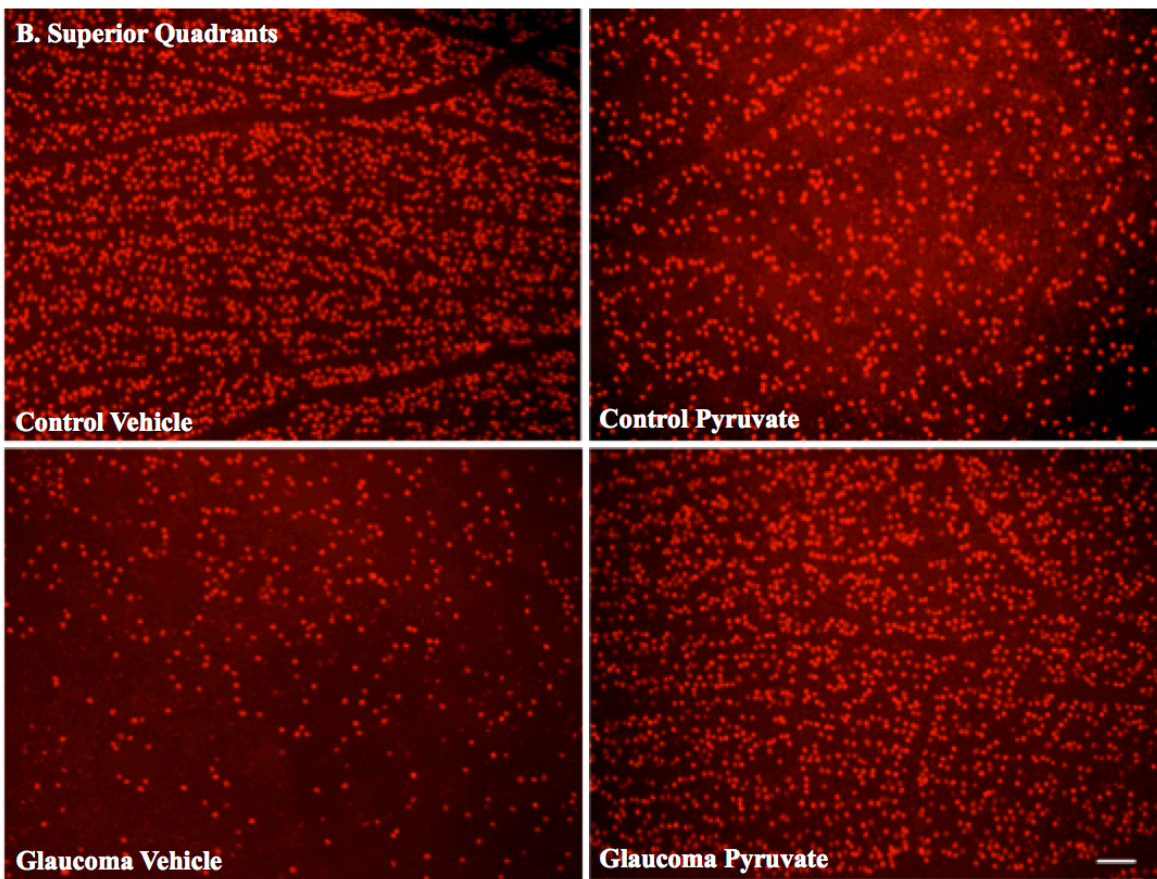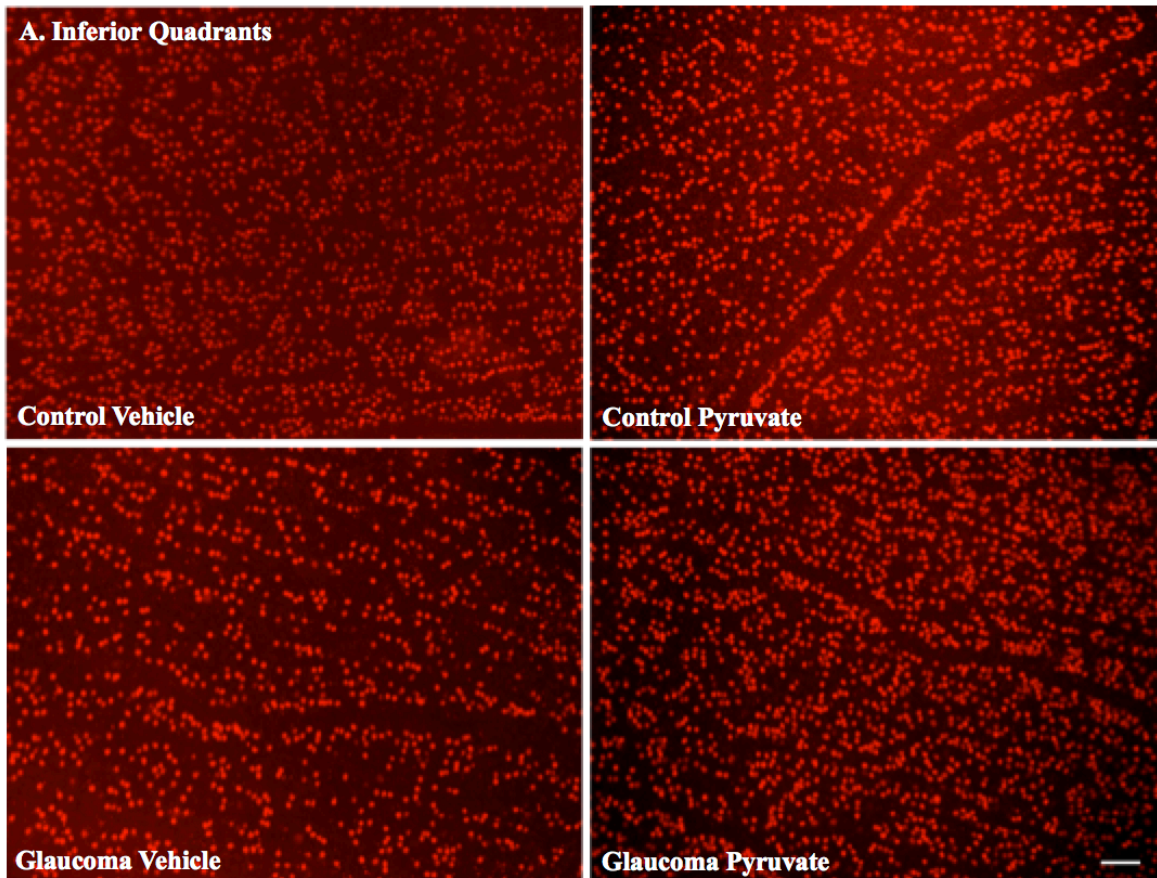
Figure 6. Box Plot summarising Brn3a-labelled RGC average cell counts per sampled retinal quadrant. Data represent Mean $\pm$ SEM and 5-95th percentiles. n = 18 (glaucoma pyruvate and control pyruvate groups) and n = 19 (glaucoma vehicle and control vehicle groups). *p <0.05 by unpaired two-tailed t test (glaucoma vehicle versus glaucoma pyruvate).

4.4.4. ON axon counts

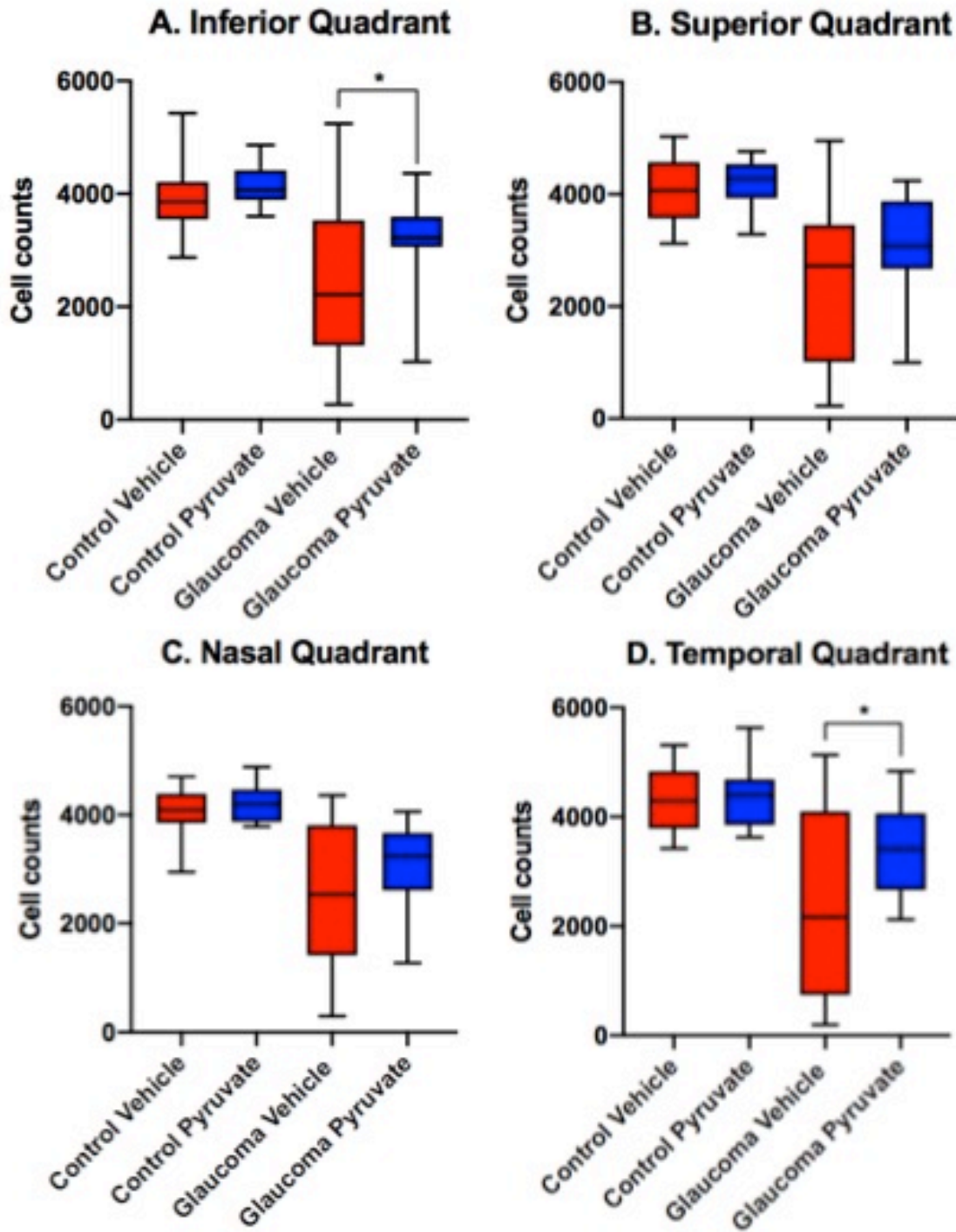To assess the health of RGC axons in this study, two different approaches were taken. The primary outcome was estimation of axon counts in toluidine blue-stained cross-sections of the proximal ON. Axon counting was determined using a semi-quantitative, automated, fixed pattern sampling approach as previously described(268). Complementary outcomes included evaluation of longitudinal sections of the distal ON immunolabeled for markers of axonal cytoskeletal damage and microglial activation (see section 4.4.5).

In the vehicle-treated group, experimental glaucoma resulted in an estimated 37% loss of axons, relative to the control nerve, as evaluated by quantification of toluidine blue-stained ON cross-sections. Greater axonal preservation was evident in the pyruvate-supplemented group (26% loss of axons relative to controls), however, this difference did not reach statistical significance (p 0.124, by unpaired student's t-test; Table 8, Figures 7 and 8).

Table 8. Effect of Pyruvate on Glaucoma-induced Axonal loss in the proximal ON

	Axon count
Control Pyruvate	73367 ± 6636
Control Vehicle	69072 ± 6412
Glaucoma Pyruvate	54572 ± 4683
Glaucoma Vehicle	43799 ± 4986
P value	0.124

Data represent Mean ± SEM, where n = 6 (control pyruvate), n = 6 (control vehicle), n = 18 (glaucoma pyruvate) and n = 18 (glaucoma vehicle). The sampled area corresponded to approximately 9% of each entire ON cross section, with the weighted average axons counts of

the five photomicrographed images used to estimate the number of surviving axons in the total ON. P value was calculated using an unpaired two-tailed t-test (glaucoma pyruvate versus glaucoma vehicle).
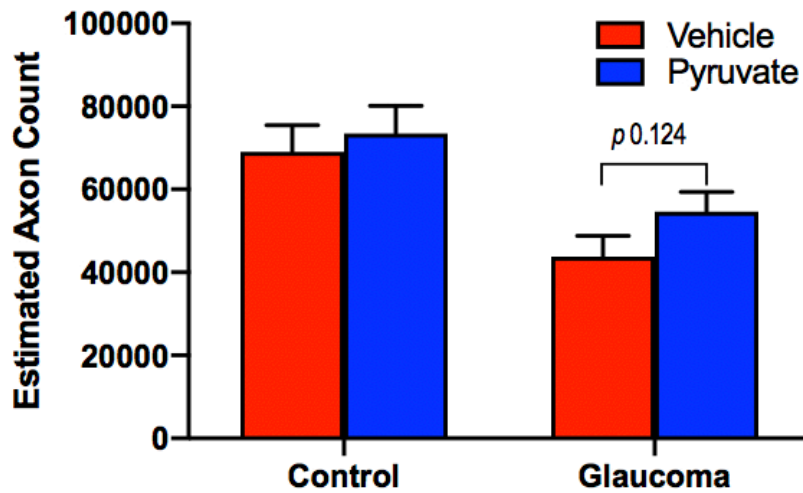
Figure 7. Estimated Proximal Axon Counts from Toluidine Blue-stained ON cross sections. Data represent Mean ± SEM (by unpaired two-tailed t test).
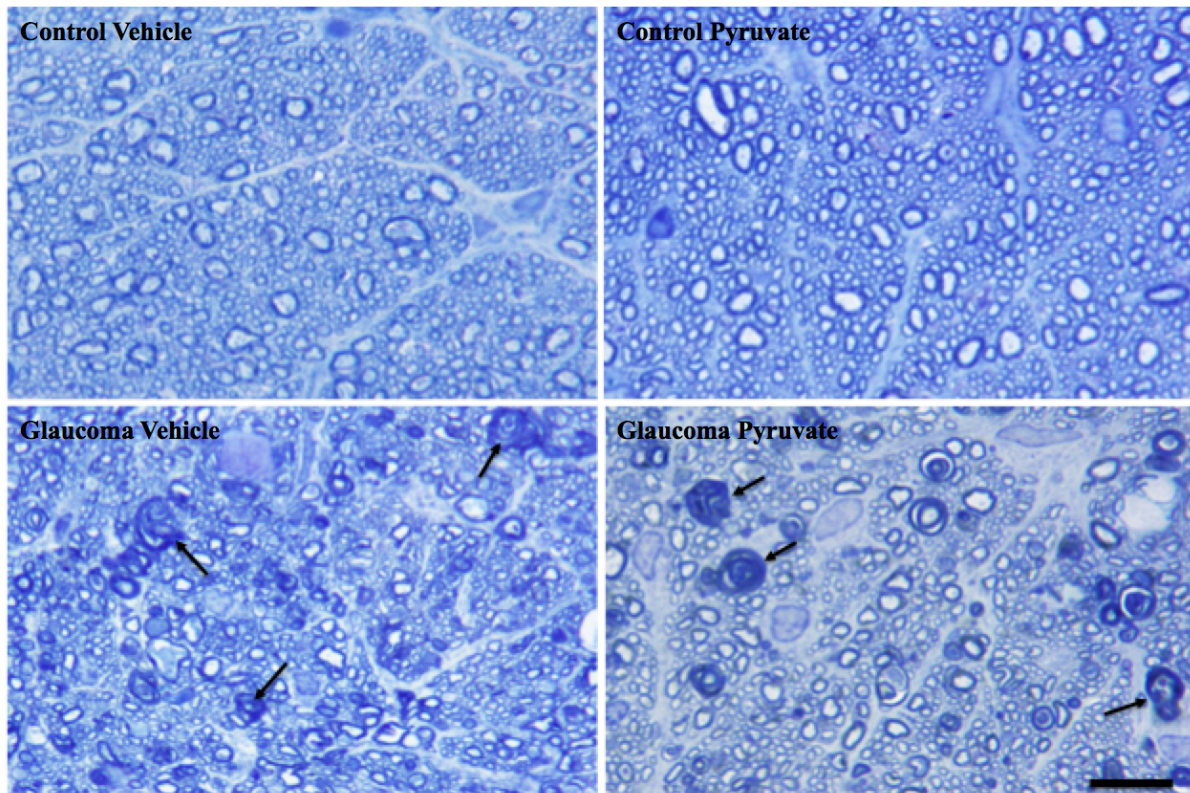
Figure 8. Representative toluidine blue-stained resin proximal optic nerve cross sections (oil-immersion microphotographs). Arrowheads refer to damaged axons, which are typically shrunken, and their myelin sheaths split into layers. Scale bar = 10μm.

4.4.5. Optic Nerve immunohistochemistry

To assess the extent of axonal degeneration in longitudinal sections of the ON, SMI32 – an antibody directed against non-phosphorylated, neurofilament heavy chain – was utilised. SMI32 highlights any axon fibers in the process of degeneration and provides information about active, rather than cumulative, injury(266,269). In control ONs, no SMI32 abnormalities were evident (Table 9, Figures 9 and10). In glaucomatous ONs, a significantly (p 0.03, by Exact Two-Sample Fisher-Pitman Permutation Test) greater number of SMI32 abnormalities were evident in the vehicle group compared to the pyruvate group (Table 9, Figures 9 and 10).

In addition to evaluation of the axonal cytoskeleton, longitudinal sections of the ON were also immunolabelled with ED1, an antibody that delineates microglial phagocytic activity. ED1 has previously been demonstrated to correlate well with axonal injury during experimental glaucoma(266). In controls ONs, no ED1 immunoreactivity were present (Table 9, Figures 11 and 12). In glaucomatous ONs, ED1 immunoreactivity was significantly (p 0.04, by Exact Two-Sample Fisher-Pitman Permutation Test) less abundant in the distal ONs of the pyruvate-treated rats compared with the vehicle group (Figures 11 and 12, Table 9).

Table 9. Effect of Pyruvate on Glaucoma-induced Neurofilament Degeneration and microglial phagocytosis in the ON.

	Neurofilament Degeneration (SMI32)	Microglial Activation (ED1)
Controls (n=37)	Absent	Absent
Glaucoma Pyruvate	1.75 ± 0.57	0.22 ± 0.05
Glaucoma Vehicle	4.45 ± 1.08	0.49 ± 0.12
P value	0.03	0.04

Data represent Mean $\pm$ SEM and are expressed as % area of immunostaining, combining the results of both ON photomicrographs, where n=37 (control), n = 18 (glaucoma pyruvate) and n = 19 (glaucoma vehicle). Controls represent contralateral untreated eyes from both pyruvate and vehicle groups. P values were calculated using Exact two-sample Fisher Pitman Permutation Test (glaucoma vehicle versus glaucoma pyruvate).
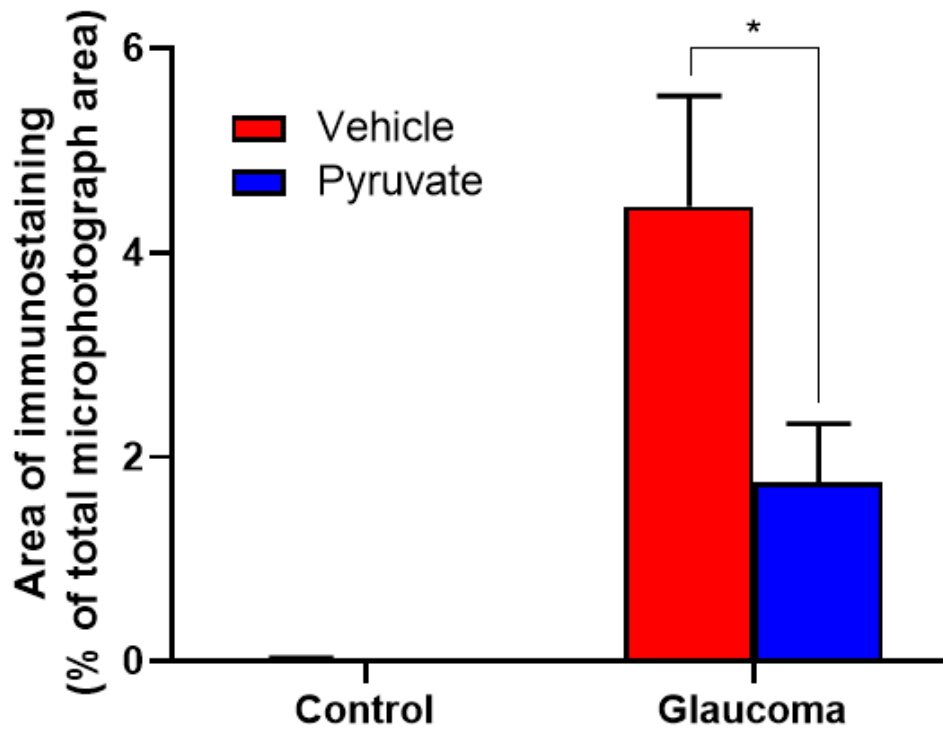
Figure 9. Box plot summarising SMI32 % area stained in glaucomatous distal optic nerves.

Data represent Mean ± SEM, where n = 18 (glaucoma pyruvate and control pyruvate groups)

and n = 19 (glaucoma vehicle and control vehicle groups). *P<0.05 by Exact two-sample

fisher-pitman permutation test.
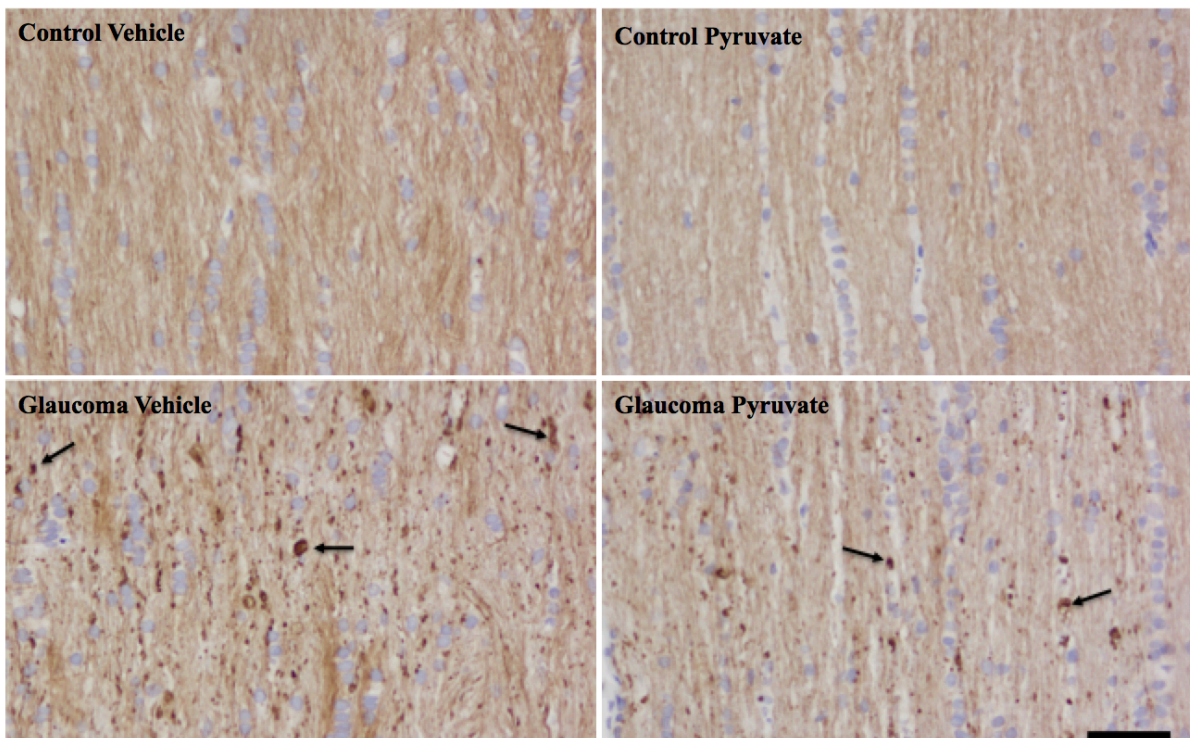
Figure 10. Representative photomicrographs of SMI32 immunohistochemistry of control and glaucomatous optic nerve sections (arrows indicate SMI32 abnormalities). Scale bar = 25μm.
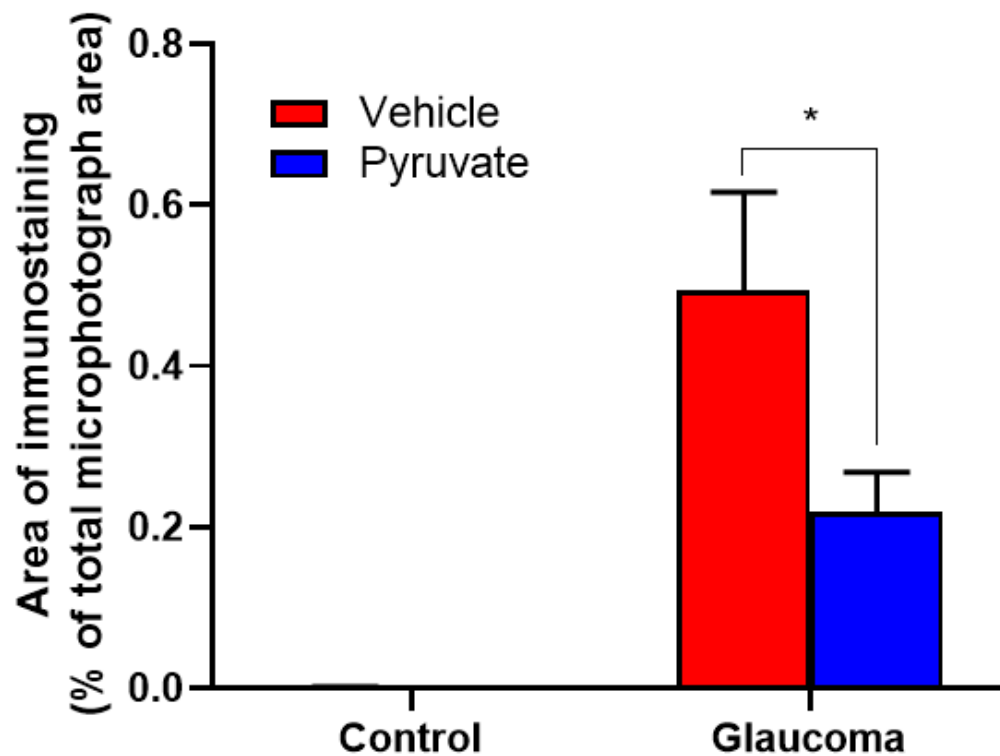
Figure 11. Box plot summarising ED1 % area stained in glaucomatous distal optic nerves. Data represent Mean ± SEM, where n = 18 (glaucoma pyruvate and control pyruvate groups) and n = 19 (glaucoma vehicle and control vehicle groups). *P<0.05 by Exact two-sample fisher-pitman permutation test.
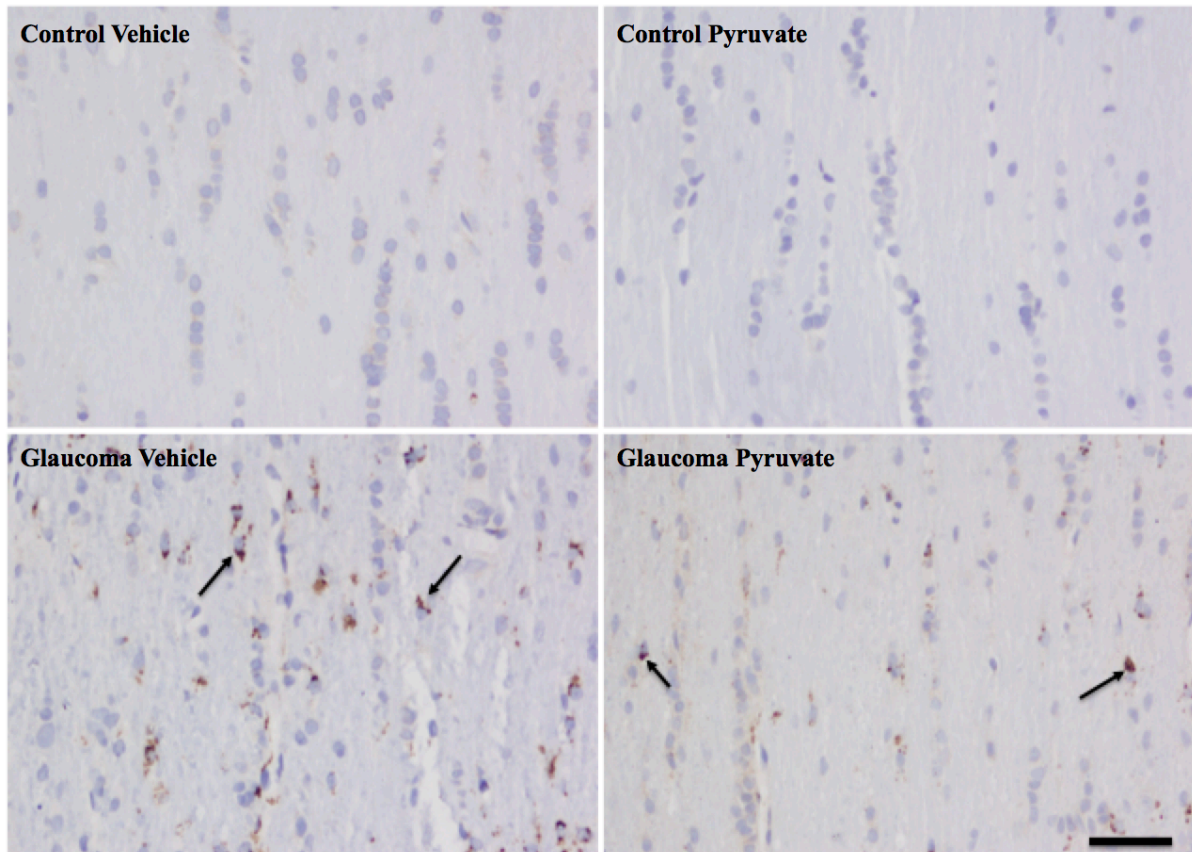
Figure 12. Representative photomicrographs of ED1 immunohistochemistry of control and glaucomatous distal optic nerve sections (arrows indicate areas of phagocytosis). Scale bar = 25μm.

4.4.6. Retinal cell cultures

Mixed retinal cell cultures were used to investigate the effects of pyruvate treatment following glucose deprivation and oxidative injury. All mixed retinal cell culture incubations were carried out for 24 hours following treatment.

Glucose deprivation resulted in the loss of all cells in culture after 24 hours. Supplementation with pyruvate counteracted the loss of both neurons (RGCs, amacrine cells, bipolar cells, horizontal cells and photoreceptors) and glia (Müller cells and astrocytes). The effect of pyruvate was dose-dependent with higher doses of pyruvate affording increased cell survival

(Figures 13-14). Interestingly, the protective effect of pyruvate was prevented completely by inclusion of the monocarboxylate transporter uptake blocker alpha-cyano-4-hydroxy-cinnamate (4-CIN, 1mM).

Figure 13. The effects of glucose deprivation and pyruvate supplementation in mixed retinal cell cultures. Controls represent mixed retinal cell cultures, stained as annotated on the left-hand column. β III tubulin and calretinin are sensitive markers for RGCs, and rhodopsin for photoreceptors. GFAP and vimentin primarily stain glial cells. GABA is a non-selective neuronal stain. The second column demonstrates glucose deprivation for 24 hours, which was catastrophic to all cells in culture. In the third column, the presence of pyruvate (dosed at 1μM) was able to counteract the loss of all cells in culture. In the fourth column, the protective effects of pyruvate were blocked completely when blocking the neuronal monocarboxylate transporter by 4-CIN (1mM).
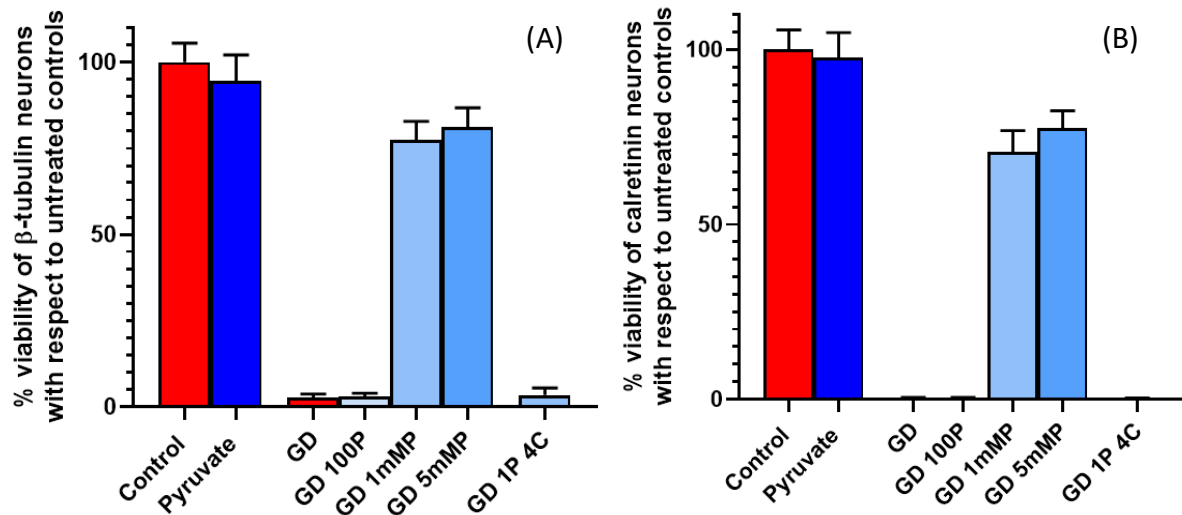
Figure 14. Percentage preservation of β-tubulin (A) and calretinin (B) stained neurons under conditions of glucose deprivation and pyruvate supplementation (Mean (SEM)). n = 8/group. Glucose deprivation caused loss of virtually for all neurons. Pyruvate supplementation offered significant neuroprotection, which was dose dependent ((A) β-tubulin stained neurons: 3% with 100microM, 78% with 1mM, 81% with 5mM, (B) calretinin stained neurons: 0% with 100microM, 71% with 1mM, 78% with 5mM). Pyruvate = controls with added pyruvate; GD = glucose deprivation; GD 100P = glucose deprivation plus 100microM pyruvate; GD 1mMP = glucose deprivation plus 1mM pyruvate; GD 5mMP = glucose deprivation plus 5mM pyruvate; GD 1P 4C = glucose deprivation plus 1mM pyruvate plus 1mM 4-CIN.

When mixed retinal cell cultures were subjected to oxidative challenge with tert-butyl Hydroperoxide (t-bH) approximately 90% of β-tubulin- and calretinin-positive neurons were lost over 24 hours (Figures 15-17). Pyruvate, dosed at 1mM, was able to counteract neuronal loss under oxidative stress with t-bH (approximately 60% neuronal rescue achieved). The antioxidative effect of pyruvate was not completely blocked by 4-CIN (1mM).
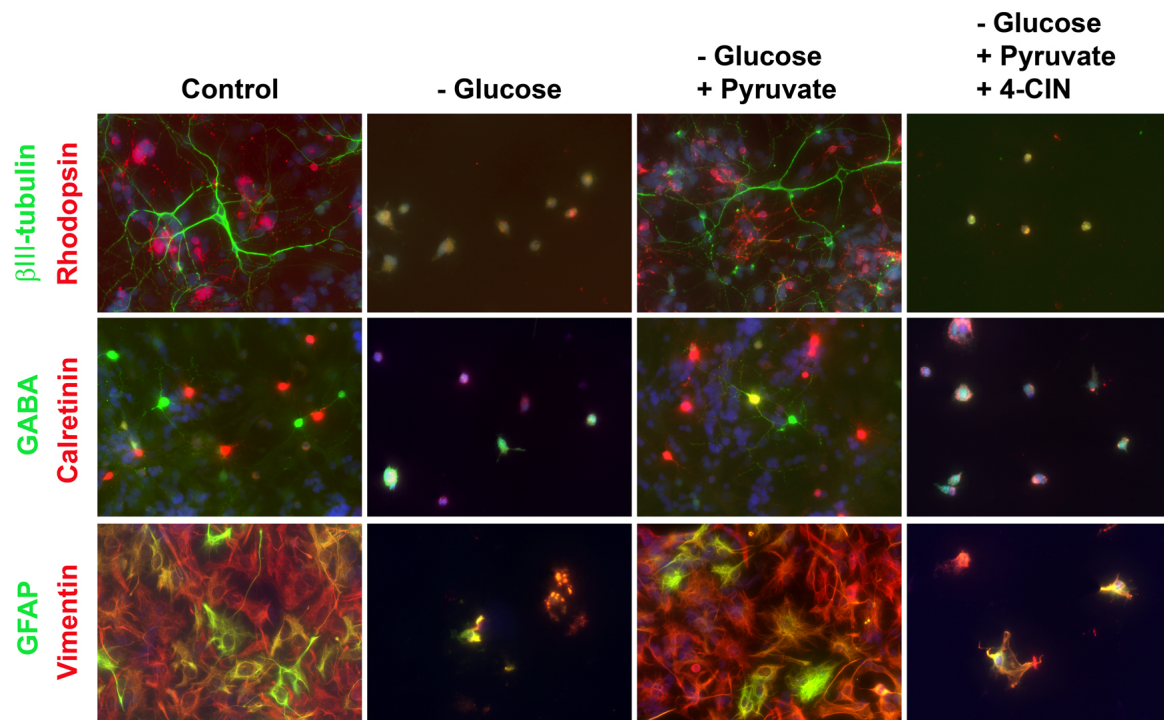
.
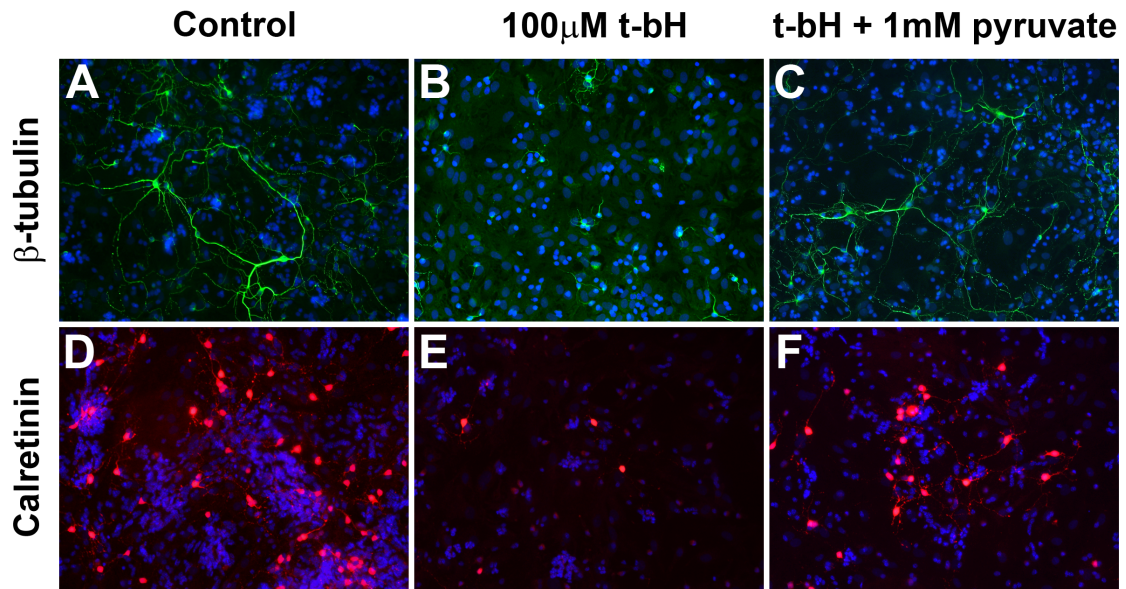
Figure 15. The effects of oxidative stress and pyruvate supplementation in mixed retinal cell cultures. Controls represent mixed retinal cell cultures, stained as annotated on the left-hand side. The second column demonstrates that oxidative challenge with t-bH (100μM) kills up to 90% of neurons (but not glia) after 24 hours. The third column shows that the presence of pyruvate (dosed at 1μM) can prevent neuronal loss under oxidative challenge with t-bH
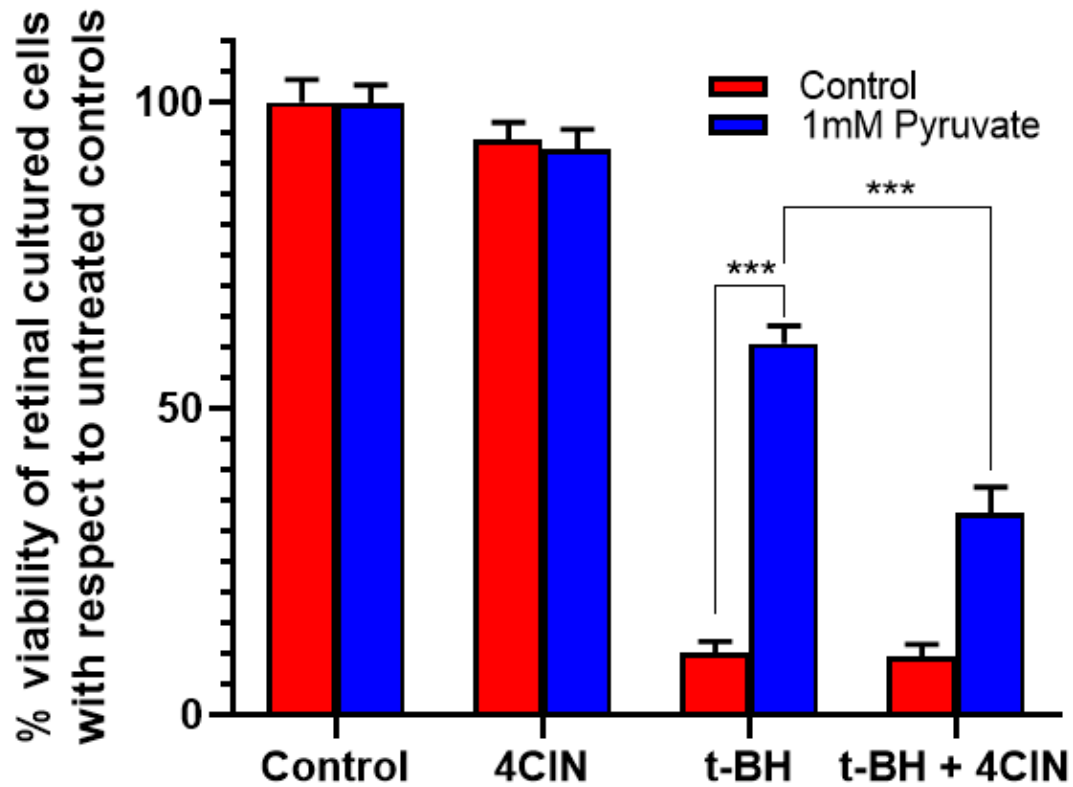
Figure 16. Viability of retinal cells in culture when treated with 4CIN and t-bH, in control and pyruvate supplemented groups. n = 8/group. Pyruvate was able to counteract the loss of retinal cells in culture under oxidative stress with t-bH, which was partially blocked by the addition of 4CIN. ***P<0.001 by one-way ANOVA plus post-hoc Tukey's multiple comparison test.
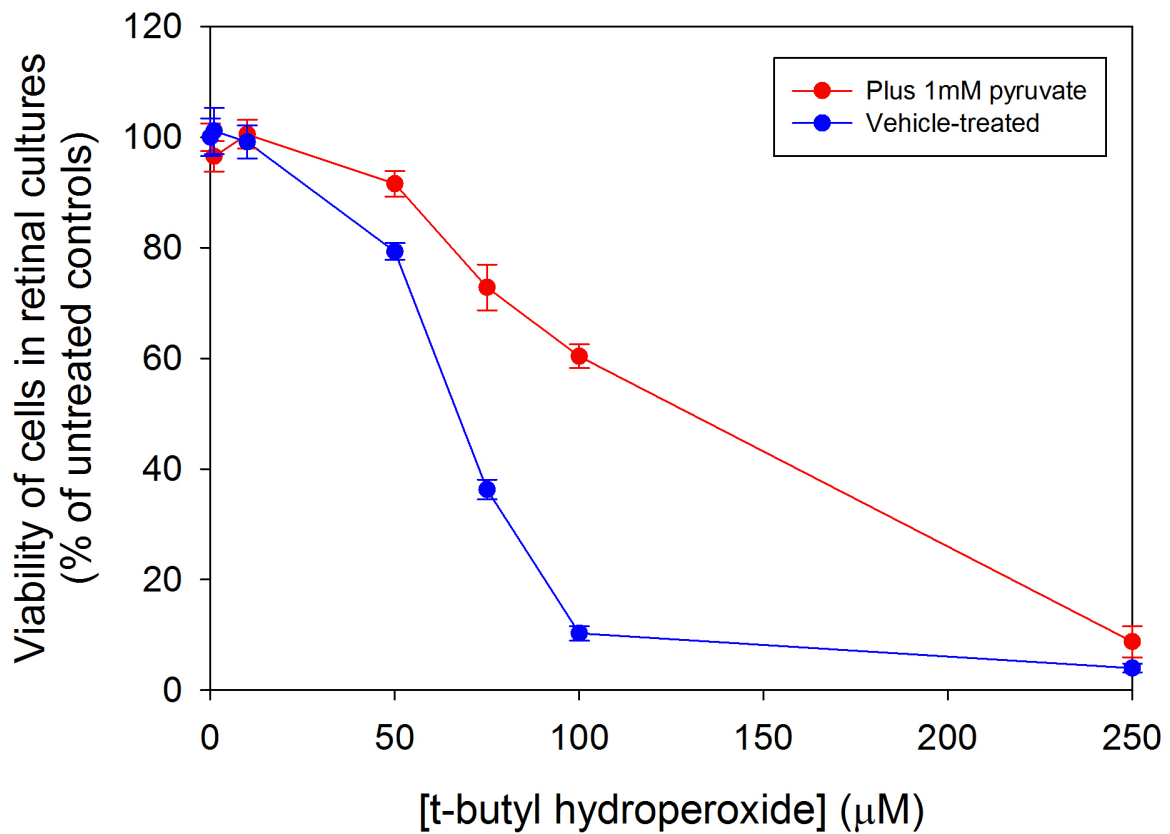
Figure 17. Viability of cells in retinal culture with increasing concentrations of t-butyl hydroperoxide (t-bH) in control and pyruvate supplemented groups. The pyruvate supplemented group (1mM) was able to counteract the loss of retinal cells in culture under the influence of t-bH.

4.5. Discussion

Overall results

Despite the advent of promising data from other neurodegenerative conditions, the neuroprotective efficacy of pyruvate has not previously been investigated in experimental glaucoma. The main aims of the present study were as follows: (1) To determine whether oral pyruvate supplementation increases the retinal bioavailability of pyruvate; (2) To test the neuroprotective effect of high dose pyruvate supplementation (500mg/kg) in the drinking water in a subacute rodent model of experimental glaucoma; (3) To explore the mechanism of action of pyruvate by interrogation of mixed retinal cell cultures.

The major findings were as follows: (1) Oral pyruvate supplementation significantly increased the bioavailability of pyruvate in the retina. (2) In the model of glaucoma, pyruvate afforded a statistically significant preservation of RGC counts per sampled retina with no discernible sectoral bias. With regard to the ON, pyruvate-treated rats showed a tendency for greater axonal preservation, relative to the vehicle-treated rats, in the proximal portion of the ON, and, displayed significantly less axonal cytoskeletal damage and microglial activation in the distal portion of the ON. Experiments using mixed retinal cell cultures demonstrated that pyruvate acted as both a metabolic, energetic substrate as well as a scavenger of reactive oxygen species in protecting cultured cells from nutrient deprivation and oxidative stress insults.

Experimental model of glaucoma

The laser-induced glaucoma model described by Levkovitch-Verbin *et.al.*(86), in which elevated IOP is achieved in rats by translimbal laser photocoagulation to the trabecular meshwork, is one of the best-described, and most widely-used, rodent models of glaucoma. It has both strengths and weaknesses as a model. The key strengths of the model are that it fulfils

the key disease criteria of sectorial RGC loss, early ONH axonal transport disruption and damage, exclusivity of RGC death, and correlation between RGC loss and IOP exposure(16,270). It is also straightforward to achieve on a technical basis. Nevertheless, the model has both a limited duration of IOP elevation and a somewhat greater magnitude of pressure than that observed in a typical open angle glaucoma patient, rendering it best described as a subacute model of glaucoma.

One difficulty with the model is that is known to cause wide inter-animal variability in terms of IOP profiles and RGC / axonal injury(70,71,86). Thus, Ebneter *et.al.*(200) reported an axon loss of 21% in their control glaucoma group at 2 weeks following induction of elevated IOP, compared with a 36.6% axon loss at the same time point in the present study, whilst Beirowski *et.al.*(271) reported an axonal loss of 52.5% in the distal ON and 88.7% in the proximal ON of control groups at 2 weeks. Bull *et.al.*(272) found an axonal loss of 60.3% in control glaucomatous ONs relative to untreated fellow eyes at 4 weeks following IOP induction. It is worth noting that Beirowski *et.al.*(271) and Bull *et.al.*(272) repeated laser therapy at weekly intervals if there was inadequate difference between the right and left eyes (i.e. <6mmHg and <10mmgHg respectively), which may, in part, account for the greater degree of axonal injury incurred. Despite the differing levels of injury seen in the literature, the model has been successfully used to conduct neuroprotective studies.

Whilst a degree of variability in IOP profile was evident amongst all treatment groups, we were able to control for this through blinded assessment of IOP profiles to ensure relative consistency and comparability between groups. In our study, an IOP integral of 286.0-306.7mmHg-days and peak IOP of 41.1-42.6mmHg was achieved in the glaucoma groups. A similar IOP integral (318.7-348.7mmHg-days) and peak IOP (38.7-41.9mmHg) were achieved

in the neuroprotection study performed by Ebneter *et.al.*(200). This was also the case for Beirowski *et.al.*(271), who documented an IOP integral of 374.6-414.2mmHg and peak IOP of 44.8-45.3mmHg. Bull *et.al.*(272) conducted their analyses at a later time point at 4 weeks, revealing an IOP integral of 410-430mmHg-days and a somewhat lower peak IOP of 28-33mmHg. Overall, therefore, the IOP profiles measured in the present study are broadly compatible with previous published studies.

In the present study, RGC damage profiles were examined at 2 weeks, which is a relatively early time point. Nevertheless, the time point has been validated in prior neuroprotection studies using the laser model of glaucoma(200,271). Of course, it would have been informative to have examined a later time point, such as 6 weeks after elevation of IOP, which is reported to result in up to 60% axonal loss(86). Such a strategy would help to determine whether the neuroprotective effect of pyruvate is sustained, or whether any apparent protection merely delayed the onset of degeneration. Nevertheless, the use of a second time point would have necessitated doubling the number of animals used, which would have incurred a significant animal ethical cost. Arguably of greater importance would be validating the effect of pyruvate supplementation on glaucomatous progression using different glaucoma models, in different species (such as the DBA/2J mouse model of hereditary glaucoma, which can be likened to human pigmentary glaucoma), and in a glaucoma model with lower pressures (for example, a rodent microbead model of glaucoma). All of these proposed studies would dramatically strengthen the clinical translatability of the data.

Evidence for pyruvate neuroprotection

There is a paucity of research in regard to the effects of pyruvate in the retina, and more specifically in relation to its effect in glaucomatous optic neuropathy. Yet, a more substantial

body of evidence supports a neuroprotective effect of pyruvate in the CNS. For example, following glucose deprivation, pyruvate supplementation has been shown to significantly protect synaptic function against the deleterious effects of hypoglycaemia in brain slices(273). Moreover, in rats subjected to insulin-induced hypoglycaemia, the addition of pyruvate upon restoration of glucose reduced CNS neuron cell death by 70-90% compared to glucose alone(262). Improved neuron survival was also observed when pyruvate delivery was delayed for up to 3 hours(262). One of the key pathophysiological events triggered by severe hypoglycaemia is the activation of poly(ADP-ribose) polymerase-1 (PARP-1). Activated PARP-1 consumes cytosolic NAD+, and because NAD+ is required for glycolysis this may render cells unable to use glucose even when glucose availability is restored following severe hypoglycaemia(262). The advantage of pyruvate is that it can be metabolised in the absence of cytosolic NAD+ and can facilitate glycolysis by recycling of NAD+, produced during the reduction of pyruvate to lactate by LDH(197,262). This finding is of particular relevance to glaucoma, as recent studies have suggested that mitochondrial abnormalities, including the age-dependent decline of retinal NAD+, are an early driver of retinal neuronal dysfunction in glaucoma(182,206,214).

Various *in vivo* studies investigating the effects of pyruvate on cerebral ischaemia have documented marked neuroprotective effects. Lee *et.al.*(258) demonstrated almost no neuronal death following transient forebrain ischaemia in rats administered intraperitoneal pyruvate. Yu *et.al.*(255) and Kim *et.al.*(256) showed that intraperitoneal ethyl pyruvate and intraperitoneal pyruvate, respectively, administered within 30 minutes of focal transient cerebral ischaemia substantially reduced infarct volumes. Given the vascular theory of glaucoma, there is good reason to believe that these findings may be transferrable to glaucoma.

In terms of the retina, Yoo *et al.*(257) showed that pyruvate protected against zinc toxicity in cultured rat retinal cells and reduced ischaemia-induced cell death in rat retinas, although they did not specifically assess RGCs, while *in vivo* experiments by Hegde *et al.*(197,198) demonstrated that pyruvate promoted retinal glycolysis in the face of ROS-induced inhibition. Wood *et al.*(265) documented that pyruvate was partially able to prevent neuron cell death in mixed neuronal-glial rat retinal cultures following treatment with a range of sodium azide concentrations, which pharmacologically inhibits the mitochondrial electron transport chain. As in the brain, it has been proposed that pyruvate functions both as an antioxidant, through inhibition of oxidative inactivation of –SH containing enzymes including GAPDH and pyruvate kinase(274–277), and as an energy substrate for both glycolysis, via the continued regeneration of NAD+(197), and oxidative phosphorylation via its conversion to acetyl CoA, which then enters the Kreb's cycle(202), depending the relative lack or abundance of oxygen respectively. The findings of our study unequivocally show that pyruvate supplementation augments RGC survival in a range of *in vivo* and *in vitro* paradigms of injury. The data provide further support for the bioenergetic theory of glaucomatous neurodegeneration, and the reliance of the retina on substrate bioavailability to augment glycolytic ATP production in the face of metabolic stress.

Mechanism of pyruvate neuroprotection

Our mixed retinal cell culture studies were able to demonstrate pyruvate acting both as a metabolic substrate, and, scavenger of reactive oxygen species, and that these effects were dose-dependent. The protective effect of pyruvate was prevented completely by inclusion of the monocarboxylate transporter (MCT) uptake blocker 4-CIN. As MCTs are required for the entry of pyruvate into cells, this indicates that pyruvate has a direct intracellular protective mechanism of action.

Supporting the role of pyruvate as a direct antioxidant are the findings of Wang *et.al.*(278), showing that pyruvate protected primary neurons in culture by inhibiting the production of hydroxyl radicals generated by cysteine autoxidation catalysed by copper. In fact, pyruvate may arguably provide a greater neuroprotective effect through its antioxidant properties than from an improvement of energy metabolism. This was demonstrated by Desagher *et.al.*(279) in which cultured striatal neurons exposed for 30 minutes to H_2O_2 survived when pyruvate was supplemented. The neuroprotective effect of pyruvate was mimicked by other α-ketoacids, but not by lactate(279). Lactate, like pyruvate, can act as a metabolic neuronal substrate(280), but unlike pyruvate does not have antioxidant properties. Nevertheless, the primary role of pyruvate in neurodegenerative conditions is likely to be related to its role as a neuronal substrate ameliorating bioenergetic insufficiency. Thus, Maus *et.al.*(281) cultured mouse striatal neurons and subjected them to N-Methyl-D-aspartate (NMDA)- or α-amino-3-hydroxy-5-methylisoxazole-4-propionate (AMPA)- induced excitotoxicity. The neuroprotective effect of pyruvate in this case was related to its ability to act as a neuronal substrate supporting ATP production in the face of excitotoxicity, rather than its ability to react with H_2O_2 by a decarboxylation process(281). A third mechanism of action of pyruvate has been proposed that relates to the ability of pyruvate to enhance glutamate efflux. Zlotnik *et.al.* demonstrated in rats(261,282) that intravenously injected pyruvate, following traumatic brain injury, resulted in a short-lived decrease in the level of blood glutamate, and a significant improvement in both neurological outcomes and neuronal survival. On a similar theme, pyruvate decreased the strong accumulation of extracellular glutamate found in both sham and NMDA-treated cultures(281), and lessened the over-activation of poly(ADP-ribose) polymerase (PARP-1), reducing the depletion of cytosolic nicotinamide-adenine dinucleotide (NAD+) in astrocyte-neuron cell cultures(283). *In vivo* models of transient cerebral ischaemia and severe

hypoglycaemia, in which PARP-1 had been shown to be a key mediator of neurotoxicity, also demonstrated neuroprotective effects of pyruvate(284–286). Conceivably, then, pyruvate's neuroprotective effects are manifold(284).

4.5.1. Limitations

Establishing optimal pyruvate dosing and route of administration

In our study, pyruvate was administered orally in the drinking water and dosed at 500mg/kg/day. We have not tested the effect of pyruvate on RGC survival at different oral doses or different routes of administration (e.g. IV or IP dosing). For ease of administration and optimal compliance, oral dosing would be the most favourable route for translation to clinical glaucoma. Of interest would be to ascertain the lowest effective dose of pyruvate required to achieve optimal RGC neuroprotection.

IP injections of ethyl pyruvate have been widely examined in different CNS neuroprotection animal studies of cerebral ischaemia and Parkinson's disease, with dosing ranging from 1mg/kg to 40mg/kg body weight(254,255). Ethyl pyruvate, a derivative of pyruvic acid, is more stable than pyruvate in aqueous solutions and exerts anti-inflammatory as well as anti-oxidant effects(287). Yu *et.al.*(255) demonstrated statistically significant effects of IP ethyl pyruvate at doses >4mg/kg body weight with increasing effects up to a maximal dose of 40mg/kg body weight. In their subsequent study examining the effect of pyruvate in transient focal cerebral ischaemia, pyruvate was administered IP at doses of 250, 500 and 1000mg/kg body weight (Sprague Dawley rats) 30 minutes after 1 hour of middle cerebral artery occlusion(256). Interestingly, IP pyruvate dosed at 500mg/kg body weight had the greatest reduction in infarct volumes(256). IP pyruvate dosed at 500-1000mg/kg has shown CNS neuroprotective effects in animal models of forebrain ischaemia, Huntington's disease and severe

hypoglycaemia(258,260,262), yet lower doses of 250mg/kg were not protective(260). Yoo *et.al.*(257) administered a rather high dose of IV sodium pyruvate at 4.6g/kg (Sprague Dawley rats) within 1 hour of pressure-induced retinal ischaemia, with potent protective effects of retinal neurons.

Neuroprotection studies using the oral route to administer pyruvate were limited on review of the literature. Age-related behavioural changes in mice were counteracted by oral pyruvate supplementation, dosed at 800mg/kg/day in the chow for 2-6 months(288). Oral pyruvate supplementation, dosed at 180mg/kg/day in drinking water for 30 days, in rats was shown to reduce glutamate levels (in cerebral spinal fluid) 24 hours after middle cerebral artery occlusion, improve neurologic recovery (with reduced lesion volume, brain oedema and extent of blood brain barrier permeability) and post-stroke depressive behaviours(289). Popova *et.al.* (290) demonstrated that oral pyruvate treatment via supplemented chow (dosed at 450mg/kg/day in mice for 3.5 months) or oral gavage (110mM sodium pyruvate dosed at 10mL / kg body weight in rats for 6-7 months) provided a strong anti-epileptic effect in three different rodent models of acquired epilepsy.

Timing of pyruvate administration in regard to glaucomatous insult

We have not tested the effect of pyruvate administered at different time intervals. It would be worthwhile exploring whether the neuroprotective efficacy of pyruvate was maintained if supplementation was not commenced until a number of days after elevating IOP. Clinically, this would have relevance in terms of knowing whether commencing pyruvate treatment at the time of, or even after, glaucoma diagnosis may help to 'rescue' vulnerable RGCs whilst attempts are implemented to lower IOP. Yet, the subacute model used herein would not be

ideally suited for this purpose. A slower progressing model, such as the DBA/2J mouse strain or an induced microbead model of glaucoma, would be preferable.

In the CNS, Yu *et. al.*(255) demonstrated that IP administration of ethyl pyruvate at various time points (30 minutes before or at 4 or 12 hours after) middle cerebral artery occlusion in rats reduced the infarct volume, supressed the associated clinical manifestations, suppressed microglial activation, and pro-inflammatory cytokine expression. Pre-treatment with ethyl pyruvate exerted better protection than post-treatment, with reduced efficacy the later it was administered from the time of cerebral insult up to 12 hours(255). When the same experiment was repeated with IP pyruvate, it was shown that treatment 30 minutes prior, or 30 minutes after, the cerebral insult reduced the infarct volume, but any later than 4 hours did not achieve substantial benefit(256). These results suggest that IP ethyl pyruvate has a wider therapeutic window in delayed cerebral ischaemic injury than IP pyruvate. Ryu *et.al.*(260) found that IP pyruvate afforded neuroprotection in a rat model of Huntington's disease if administered from the time of intrastriatal injection of quinolinic acid (QA) to 1 hour post-administration, but no protection was observed if pyruvate was applied 30 minutes prior to or 3 hours after QA injection. In a rat model of severe hypoglycaemia, pyruvate administered 1 hour after hypoglycaemia showed a robust neuroprotective effect in all brain regions, with reduced efficacy when delayed until 3 hours after hypoglycaemia and no effect with a delay of 6 hours(262). Thus, it appears that the timing of pyruvate to confer optimal neuroprotection may vary between CNS injuries.

Limitations in determining retinal bioavailability
We have demonstrated that retinal levels of pyruvate were increased in our pyruvate-supplemented animals. Metabolism is a dynamic and complex biological function, and so a

static measure of function will never provide a truly accurate reflection of these processes. Even from the time of death of an animal to extraction and processing of retinal tissue, there will of course be a period of anoxia and alterations in cellular metabolism. Thus, it could be speculated that whilst an increased abundance of pyruvate was evident in the retinal tissue, a considerable portion of this substrate may have already been metabolised by retinal cells prior to quantification.

Whilst retinal bioavailability was increased by oral pyruvate supplementation, this data does not reflect whether there was a deficit of pyruvate in RGCs subjected to glaucomatous insult. RGCs comprise approximately 50% of the ganglion cell layer in the rodent retina(118), and therefore only represent a tiny fraction of the entire retinal cell population. RGC specific RNA-sequencing studies performed by Williams *et.al.*(182) using the DBA/2J mouse glaucoma model suggest that RGCs are subjected to mitochondrial stress and metabolite depletion during glaucoma, which shifts them toward fatty acid metabolism. Prior rodent studies have demonstrated that elevated IOP, regardless of the mechanism or duration of insult, appears to induce oxidative stress in the retina and optic nerve(177,291–294). More specifically, protein oxidation was localised to the inner retinal layers containing RGCs in a study that used hypertonic saline injection into the episcleral vein to elevate IOP(295). Studies investigating the histologic localisation of mitochondrial activity in the human optic nerve and retina have demonstrated a high level of cytochrome c oxidase (COX) and succinate dehydrogenase (SDH) activity in the unmyelinated laminar and prelaminar portions of the optic nerve (lower levels were seen in myelinated portions of the optic nerve), and moderate to high levels of COX and SDH in the retinal ganglion cell bodies(183). Given that these enzymes are specific to the mitochondria and essential for OXPHOS, these results indicate a high level of oxidative enzyme activity at these sites. Furthermore Chidlow *et.al.* (253) demonstrated a high level of

mitochondrial pyruvate dehydrogenase and mitochondrial pyruvate carrier (MPC 1) in the GCL and inner plexiform layer of vascularised retinas of rat and marmoset, and the avascular retinas of rabbit and guinea pig. RGCs were particularly enriched with mitochondrial proteins(253), inferring that pyruvate-derived OXPHOS is important in RGCs. It may have been useful to investigate the activity of these enzymes, and/or their by-products, of oxidative metabolism in our model of experimental glaucoma and determine the effect of supplemental pyruvate (by Laser capture microdissection).

Disparity between RGC somal vs axonal neuroprotection

The primary outcomes of this study were RGC counts in retinal wholemounts and axon counts in ON cross sections. Whilst pyruvate facilitated statistically significant protection of RGC somas, there was only a trend for axonal protection. There are three general possibilities to account for this disparity: (1) that pyruvate may have caused compartmentalised protection, (2) that pyruvate protected both RGC somas and axons, but the signal-to-noise ratio of axon counts on the ON cross sections was lower than that of the RGC counts in retinal wholemounts, which rendered it a less powerfully tool statistically (i.e. a genuine difference between groups was less able to be detected), and (3) the methodological limitations of toluidine blue staining of resin embedded cross sections, which is well suited to identifying gross abnormalities and axonal loss (16,86) but only provides an estimate of the total axonal counts.

(1) Compartmentalised protection is unlikely. In our prior bioenergetic study using glucose, which used the same limbal laser model of experimental glaucoma in Sprague-Dawley rats over a two-week time period, statistically significant neuroprotection of both RGC axons and somas were demonstrated(200). Other glaucoma neuroprotection studies have also demonstrated both somal and axonal protection(182,215,228,230). Whilst axon degeneration

can initiate from different neuronal compartments (i.e. the soma, terminal boutons, or the axon itself), the initial stages of neurodegeneration often manifest in the axon compartment(296). Axons require up to 70% of all energy used by a neuron, which is primarily generated through oxidative metabolism, making them particularly vulnerable to metabolic stress(296). Conceivably, then, bioenergetic neuroprotection should protect both axons and somas. However, there is evidence that the nature of injury in experimental models of glaucoma dictates the course of axonal degeneration (i.e. anterograde degeneration after ON transection, but retrograde degeneration after crush injury)(296). It is of relevance that the primary site of injury occurs at the ONH in the laser model of glaucoma with resulting anterograde degeneration of axons, and retrograde injury and death of somas(16). Thus, it is conceivable that pyruvate delays retrograde loss of RGC somas more readily than it can delay Wallerian degeneration of their axons. In this regard, it would have been useful to examine the superior colliculus (i.e. the most distal site of the optic projection in rodents) to determine whether optic nerve functionality was improved by pyruvate(297).

(2) It is most likely that pyruvate protected both RGC axons and somas. Firstly, both SMI32 and ED1 did show statistically significant protection. SMI32 is a sensitive marker of ongoing injury to the ON axonal cytoskeleton(16), while ED1 offers a measure of cumulative microglial phagocytic activity(266,269). These complementary markers have previously demonstrated a statistically significant correlation between axonal injury and microglial response(266).

Secondly, while toluidine blue staining of resin embedded ON cross sections are well suited to identifying gross abnormalities and axonal loss(16,86), this method only provides an estimate of the total axonal count and does have genuine methodological limitations. Estimation of axonal loss was achieved by using the 'fixed pattern sampling method' described

by Ebneter *et al.* (268). Whilst full axon manual counting on transmission electron microscopy (TEM) is considered the gold standard, it is exceedingly time consuming and impractical with larger sample sizes(298). Manual counting on TEM is also not without its limitations; with only about 45% of the optic nerve cross section amenable for analysis because the mesh grid used occupies about half the tissue area and thus total nerve counts must be extrapolated(298,299). Even though light microscopy methods can underestimate the total number of axons by up to 20-30% in comparison to EM methods, it has the advantages of lower cost and improved time efficiency(298). Like that of RGC counts on retinal wholemounts, axon counting can also be prone to sampling bias. However, it must be acknowledged that only a small proportion (<10%) of axons in the ON are counted using the sampling technique, unlike in wholemounts. There can be substantial inter-animal variability of axon numbers between individual animals of the same strain(300), the axon density varies within the optic nerve and damage is not uniform(301). Nonetheless, for practical reasons, semi-automated counting of images taken after targeted sampling provides acceptable accuracy(268,272,298). When all of the issues are considered, alongside the fact that the model itself causes a wide inter-animal variability in induced injury in the vehicle treated group, it is not surprising that significance was not reached for the toluidine blue outcome. Indeed, the protection afforded by Brn3a only reached 0.04. Larger sample sizes may have compensated for this.

Other limitations

RGC functional outcomes were not assessed in our study. Clinical and laboratory based studies have confirmed that RGC functional loss, assessed using variants of the electroretinogram technique (ERG), precedes the structural loss of RGCs in glaucoma(302–305). ERGs can non-invasively assess the activity of inner retinal neurons in experimental and genetic models of glaucoma(306), allowing for repeated measures over time to monitor glaucomatous visual

impairment. The scotopic threshold response (STR) of the dark-adapted ERG arises from the inner retina and can provide a sensitive marker of RGC activity(307–310). Pattern ERG (PERG) is, however, regarded as the most sensitive and specific functional marker of RGCs and permits non-invasive monitoring of the electrical responsiveness of RGCs to contrast-reversing visual stimuli in real-time(306,311,312). Given that loss of PERG signal can be partly restored after lowering of IOP(306,313–315), this implies the presence of dysfunctional but potentially viable RGCs(302). Using ERG assessments would therefore be useful in detecting early-stage glaucomatous dysfunction and may provide evidence as to whether pyruvate supplementation can reverse this dysfunction by 'rescuing' compromised, but not yet dead, RGCs.

4.5.2. Future directions

It may be worth investigating whether pyruvate in combination with different compounds may offer additive or synergistic therapeutic benefit. This has been demonstrated in other CNS work using animal models of Huntington's disease and neonatal hypoxic-ischaemic encephalopathy(316,317). Nicotinamide has already been validated in preclinical trials as a strong neuroprotective candidate in experimental glaucoma(182,206) and is therefore ideally positioned to provide synergistic effect when combined with pyruvate. Coenzyme Q10 has demonstrated neuroprotective effects in a high IOP glaucoma model(318), *in vitro* and *in vivo* models of retinal damage(319,320) and other neurodegenerative diseases of the central nervous system (such as Parkinson's and Huntington's disease)(321,322). Creatine has been found to offer neuroprotective effects against intracerebral injection of NMDA in rats(323), *in vivo* models of traumatic brain injury(324) and in rodent models of ischaemic brain injury(325,326). However, to our knowledge, there have been no published studies to date investigating the effects of creatine against retinal or optic nerve neurodegenerative diseases.

4.6. Conclusion

Evidence is accumulating to support the neuroprotective effect of pyruvate in a range of acute and chronic experimental models of neurodegenerative diseases, such as ischaemic brain injury, hypoglycaemic brain injury, Huntington's disease, neuroblastoma, closed head injury, and Parkinson's disease(254–262). Thus, it is not unexpected that we have demonstrated that pyruvate supplementation is similarly beneficial in our experimental rodent model of glaucoma. We have shown that oral pyruvate supplementation increases the retinal bioavailability of pyruvate, that it can act as both as a metabolic substrate and scavenger of reactive oxygen species. Pyruvate is available commercially over the counter, is relatively cost-effective, and causes no significant adverse effects at therapeutic doses. Whilst optimal dosing needs to be further elucidated to ensure satisfactory retinal bioavailability, our results have the potential for translation to clinical trials to evaluate its neuroprotective effect in slowing the rate of visual deterioration in established glaucoma as an adjunct to IOP-lowering therapies.

5. Conclusions and Future Directions

5.1. Overall significance and contribution to the current knowledge

Our automated RGC counting algorithm was highly accurate and reproducible in a variety of RGC and neuronal specific immunolabels in both naïve and diseased retina. This novel approach to automating RGC counts on immunolabelled retinal wholemounts promises to accelerate data acquisition for statistical analysis and improve research productivity. This would, in turn, enable more timely, efficient pre-clinical neuroprotection studies to evaluate promising therapies for glaucoma. There is also potential for wider application of this software to other labelling protocols and tissue mediums (such as immunolabelled cells in culture or on fundoscopy images).

Our pyruvate neuroprotection study further validates that mitochondrial dysfunction may have a critical role in glaucomatous optic neuropathy. Oral pyruvate supplementation increased pyruvate bioavailability in the retina, afforded protection to RGCs, decreased axonal loss and degeneration, and attenuated microglial phagocytic activity in the ONs of pyruvate-supplemented glaucomatous rats. Mixed retinal cell cultures indicated that pyruvate has the potential to act as an energy substrate and antioxidant, which may account for its beneficial activity *in vivo*. These results potentially unveil a novel neuroprotective therapy for glaucoma, to be used as an adjunct to traditional IOP-lowering therapies.

5.2. Future directions

Despite large numbers of laboratory-based reports of successful neuroprotection in animal glaucoma models of glaucoma, clinical translation has been extremely limited. Indeed, at this point in time, all therapies for glaucoma remain limited to lowering IOP. Nevertheless, inherited and experimentally-induced animal models of OHT are proving highly useful to

132

understanding how OHT induces RGC and ON pathology(73). Unfortunately, to date, no single model emulates all aspects of primary open angle glaucoma and each models is not without its limitations(71). Regardless of the inherent difficulties of finding the perfect animal model of glaucoma that mirrors human disease, it should be recognised that glaucoma is a complex and multifactorial disease of which the pathogenesis remains incompletely understood and indeed can be unique to each patient.

5.3. Strategies to Advance Clinical Neuroprotection Studies

Obstacles to clinical neuroprotection studies relating to glaucoma include its slow progression, heterogeneity of pathogenesis, and the fact that evidence of neuroprotection would need to be detectable beyond the therapeutic effect of routine IOP reduction. The chronicity of glaucoma and the general slow rate of progression make clinical neuroprotection studies challenging and potentially prohibitive in terms of the time and cost required to investigate a new therapy. However, there are strategies that could considerably reduce the time and sample size required to obtain a definitive result. Traditionally, the gold standard primary outcome in clinical glaucoma studies has been automated perimetry. However, modern practice incorporates optical coherence tomography (OCT) as a routine clinical tool, with structural changes generally detectable at an earlier stage than visual field changes. Guided Progression Analysis (GPA) on the Cirrus HD-OCT (Carl Zeiss Meditec, Dublin, CA) provides a trend-based statistical analysis that could conceivably replace perimetry as a primary outcome in neuroprotection studies. It may be judicious to initially target "lower hanging fruit" where outcomes could be assessed more rapidly. This could include a randomized controlled trial of neuroprotectant therapy versus placebo in acute glaucoma or situations where IOP may be temporarily poorly controlled. Similarly, it would be advantageous to select a sample of

individuals with chronic glaucoma who were rapidly progressing. Identification of such individuals would be enhanced by large databases at national or international levels.

Thoughtful study design and sophisticated statistical analyses can considerably reduce sample sizes. When obtaining multiple measurements over time comparing rates of progression between two groups (treated and placebo) where individuals have variable starting points and rates of progression, the ideal statistical framework is a linear mixed model incorporating random intercepts and random slopes. This model accounts for the correlated nature of the data and neatly handles inevitable missing numbers. Estimates of intercepts, slopes, and correlations can be obtained relatively easily from existing data. Sample sizes are easily determined using open source software(327). The numbers required can be surprisingly small. As an example, consider a trial in which assessments are taken every three months for 24 months (9 visits) and we estimate a 30% reduction in the rate of progression in the group receiving a novel neuroprotectant compared to the control group. The participants are selected to have a relatively rapid rate of progression (1 dB per year). We estimate the random intercept to have a variance of 0.3, the random slope to have a variance of 0.7, and a residual variance of 0.1. The estimate the correlation between random slope term and random intercept term is 0.7. Using these estimates, for a power of 80% and alpha value of 0.05, only 46 individuals are required in each group(328,329).

5.4. Conclusions

Glaucoma has a multifactorial pathogenesis, broadly categorised into vascular and mechanical theories, which drives progressive optic neurodegeneration and consequent blindness. Whilst IOP lowering therapies generally slow the progress of glaucoma progression, they are of limited effectiveness due to the fact that IOP is not the sole determinant influencing

progression. Thus, there is growing demand for, and investment in, neuroprotection research to provide an adjunct to IOP lowering therapies and prevent visual decline.

Accurately quantifying immunolabelled RGCs on retinal wholemounts is a key histopathological determinant in experimental glaucoma research. Traditionally this has been performed by manual or semi-automated counting of RGCs, which is a labour intensive, time consuming and tedious process subject to inter and intra-observer variability. To solve this cumbersome issue, we have developed an automated software, created to accurately and efficiently count immunolabelled RGCs with the ability to batch process images. Ultimately, this software can help accelerate data acquisition and improve research productivity, expediating translation from the laboratory to the clinic.

Oral pyruvate supplementation has proven to be a potent neuroprotectant in our experimental model of glaucoma. Pyruvate is readily available and safe to administer. It is an ideal candidate to be considered for clinical translation, yet optimal dosing and administration needs to be further elucidated. Whilst there is an ever-increasing abundance of preclinical research, clinical translation remains in early infancy and not without its inherent challenges. Refinement of clinical trial design and the use of validated monitoring techniques may improve the cost burden and efficiency of clinical neuroprotective trials in glaucoma research.

6. References

1. Dirani M, Crowston JG, Taylor PS, Moore PT, Rogers S, Pezzullo ML, et al. Economic impact of primary open-angle glaucoma in Australia. Clin Exp Ophthalmol. 2011;39(7):623–32.

2. Zhang K, Zhang L, Weinreb RN. Ophthalmic drug discovery: novel targets and mechanisms for retinal diseases and glaucoma. Nat Rev Drug Discov. 2012;11:541–59.

3. Tham Y-C, Li X, Wong TY, Quigley HA, Aung T, Cheng C-Y. Global Prevalence of Glaucoma and Projections of Glaucoma Burden through 2040 A Systematic Review and Meta-Analysis. Ophthalmology. 2014;121(11):2081–90.

4. Weih LM, Nanjan M, McCarty CA, Taylor HR. Prevalence and predictors of open-angle glaucoma: Results from the visual impairment project. Ophthalmology. 2001;108(11):1966–72.

5. Mitchell P, Smith W, Attebo K, Healey PR. Prevalence of Open-angle Glaucoma in Australia. Ophthalmology. 1996;103(10):1661–9.

6. Peters D, Bengtsson B, Heijl A. Lifetime Risk of Blindness in Open-Angle Glaucoma. Am J Ophthalmolmol. 2013;156(4):724–30.

7. Brubaker RF. Delayed Functional Loss in Glaucoma LI I Edward Jackson Memorial Lecture. Vol. 121, Am J Ophthalmol. 1996.

8. Altangerel U, Spaeth GL, Rhee DJ. Visual function, disability, and psychological impact of glaucoma. Curr Opin Ophthalmol. 2003;14(2):100–5.

9. Barkan O. Glaucoma: Classification, Causes, and Surgical Control: Results of Microgonioscopic Research. Am J Ophthalmol. 1938;21(10):1099–117.

10. Webers CAB, Beckers HJM, Nuijts RMMA, Schouten JSAG. Pharmacological Management of Primary Open-Angle Glaucoma. Drugs Aging. 2008;25(9):729–59.

11.   deLuise VP, Anderson DR. Primary infantile glaucoma (congenital glaucoma). Surv Ophthalmol. 1983 Jul 1;28(1):1–19.

12.   Kitazawa Y, Yamamoto T. Glaucomatous visual field defects: their characteristics and how to detect them. Clin Neurosci. 1997;4(5):279–83.

13.   Rasker MTE, Enden A van den, Bakker D, Hoyng PFJ. Rate of Visual Field Loss in Progressive Glaucoma. Arch Ophthalmol. 2000 Apr 1;118(4):481–8.

14.   Sommer A, Tielsch JM, Katz J, Quigley HA, Gottsch JD, Javitt J, et al. Relationship Between Intraocular Pressure and Primary Open Angle Glaucoma Among White and Black Americans. Arch Ophthalmol. 1991 Aug 1;109(8):1090–5.

15.   Casson RJ, Chidlow G, Wood JP, Crowston JG, Goldberg I. Definition of glaucoma: clinical and experimental concepts. Clin Exp Ophthalmol. 2012;40(4):341–9.

16.   Chidlow G, Ebneter A, Wood JPM, Casson RJ. The optic nerve head is the site of axonal transport disruption, axonal cytoskeleton damage and putative axonal regeneration failure in a rat model of glaucoma. Acta Neuropathol. 2011;121:737–51.

17.   Quigley HA, Addicks EM, Green WR, Maumenee AE. Optic Nerve Damage in Human Glaucoma. Arch Ophthalmol. 1981 Apr 1;99(4):635–49.

18.   Vrabec F. Glaucomatous cupping of the human optic disk. Albr Von Graefes Arch Klin Exp Ophthalmol. 1976;198(3):223–34.

19.   Quigley H, Dunkelberger G, Green R. Retinal Ganglion Cell Atrophy Correlated With Automated Perimetry in Human Eyes With Glaucoma. Am J Ophthalmol. 1989;107(5):453–64.

20.   Morgan JE. Retinal Ganglion Cell Shrinkage in Glaucoma. J Glaucoma. 2002;11(4):365–70.

21.   Stein JD, Challa P. Mechanisms of action and efficacy of argon laser trabeculoplasty and selective laser trabeculoplasty. Curr Opin Ophthalmol. 2007;18(2):140–5.

22. McIlraith I, Strasfeld M, Colev G, Hutnik CML. Selective laser trabeculoplasty as initial and adjunctive treatment for open-angle glaucoma. J Glaucoma. 2006;15(2):124–30.

23. Melamed S, Simon GJ Ben, Levkovitch-Verbin H. Selective Laser Trabeculoplasty as Primary Treatment for Open-angle Glaucoma. Arch Ophthalmol. 2003;121(7):957–60.

24. Musch DC, Gillespie BW, Lichter PR, Niziol LM, Janz NK, Study C, et al. Visual Field Progression in the Collaborative Initial Glaucoma Treatment Study: The Impact of Treatment and other Baseline Factors. Ophthalmology. 2009;116(2):200–7.

25. Lavia C, Dallorto L, Maule M, Ceccarelli M, Fea AM. Minimally-invasive glaucoma surgeries (MIGS) for open angle glaucoma: A systematic review and meta-analysis. PLoS One. 2017;12(8):1–33.

26. Chang EE, Goldberg JL. Glaucoma 2.0: Neuroprotection, Neuroregeneration, Neuroenhancement. Ophthalmology. 2012;119(5):979–86.

27. Garway-Heath DF, Crabb DP, Bunce C, Lascaratos G, Amalfi F, Anand N, et al. Latanoprost for open-angle glaucoma (UKGTS): a randomised, multicentre, placebo-controlled trial. Lancet. 2015;385:1295–304.

28. Kass MA, Heuer DK, Higginbotham EJ, Johnson CA, Keltner JL, Miller JP, et al. The Ocular Hypertension Treatment Study. Arch Ophthalmol. 2002 Jun 1;120(6):701–13.

29. Heijl A, Leske MC, Bengtsson B, Hyman L, Bengtsson B, Hussein M. Reduction of Intraocular Pressure and Glaucoma Progression. Arch Ophthalmol. 2002;120(10):1268–79.

30. Collaborative Normal-Tension Glaucoma Study Group. The Effectiveness of Intraocular Pressure Reduction in the Treatment of Normal-Tension Glaucoma. Am J Ophthalmol. 1998;126(4):498–505.

31. Casson RJ, Chidlow G, Ebneter A, Wood JPM, Crowston J, Goldberg I. Translational

neuroprotection research in glaucoma: a review of definitions and principles. Clin Exp Ophthalmol. 2012;40:350–7.

32. Yu D-Y, Cringle SJ, Balaratnasingam C, Morgan WH, Yu PK, Su E-N. Retinal ganglion cells: Energetics, compartmentation, axonal transport, cytoskeletons and vulnerability. Prog Retin Eye Res. 2013;36:217–46.

33. Osborne NN. Mitochondria: Their role in ganglion cell death and survival in primary open angle glaucoma. Exp Eye Res. 2010;90(6):750–7.

34. Chidlow G, Melena J, Osborne NN. Betaxolol, a beta(1)-adrenoceptor antagonist, reduces Na(+) influx into cortical synaptosomes by direct interaction with Na(+) channels: comparison with other beta-adrenoceptor antagonists. Br J Pharmacol. 2000;130(4):759–66.

35. Osborne N., Cazevieille C, Carvalho A., Larsen A., DeSantis L. In vivo and in vitro experiments show that betaxolol is a retinal neuroprotective agent. Brain Res. 1997 Mar 14;751(1):113–23.

36. Wood JPM, DeSantis L, Chao H-M, Osborne NN. Topically Applied Betaxolol Attenuates Ischaemia-induced Effects to the Rat Retina and Stimulates BDNF mRNA. Exp Eye Res. 2001;72(1):79–86.

37. Wood JP., Schmidt K-G, Melena J, Chidlow G, Allmeier H, Osborne N. The β-adrenoceptor antagonists metipranolol and timolol are retinal neuroprotectants: comparison with betaxolol. Exp Eye Res. 2003;76(4):505–16.

38. Gross RL, Hensley SH, Gao F, Wu SM. Retinal ganglion cell dysfunction induced by hypoxia and glutamate: Potential nueroprotective effects of β-blockers. Surv Ophthalmol. 1999;43(Supplement 1):162–70.

39. Messmer C, Flammer J, Stümpfig D. Influence of Betaxolol and Timolol on the Visual Fields of Patients With Glaucoma. Am J Ophthalmol. 1991;112(6):678–81.

40.	Kaiser HJ, Flammer J, Stümpfig D, Hendrickson P. Longterm visual field follow-up of glaucoma patients treated with beta-blockers. Surv Ophthalmol. 1994;38(Supplement):S156–60.

41.	Collignon-Brach J. Longterm effect of topical beta-blockers on intraocular pressure and visual field sensitivity in ocular hypertension and chronic open-angle glaucoma. Surv Ophthalmol. 1994;38(Supplement):S149–55.

42.	Drance SM. A comparison of the effects of betaxolol, timolol, and pilocarpine on visual function in patients with open-angle glaucoma. J Glaucoma. 1998;7(4):247–752.

43.	Sorensen SJ, Abel SR. Comparison of the ocular Beta-Blockers. Ann Pharmacother. 1996;30(1):43–54.

44.	Araie M, Mayama C. Use of calcium channel blockers for glaucoma. Prog Retin Eye Res. 2011;30:54–71.

45.	Yamada H, Chen Y-N, Aihara M, Araie M. Neuroprotective effect of calcium channel blocker against retinal ganglion cell damage under hypoxia. Brain Res. 2006;1071(1):75–80.

46.	Takahashi K, Lam TT, Edward DP, Buchi ER, Tso MOM. Protective Effects of Flunarizine on Ischemic Injury in the Rat Retina. Arch Ophthalmol. 1992;110(6):862–70.

47.	Osborne NN, Wood JPM, Cupido A, Melena J, Chidlow G. Topical Flunarizine Reduces IOP and Protects the Retina against Ischemia-Excitotoxicity. Invest Ophthalmol Vis Sci. 2002;43(5):1456–64.

48.	Crosson C, Willis J, Potter D. Effect of the Calcium Antagonist, Nifedipine, on Ischemic Retinal Dysfunction. J Ocul Pharmacol. 1990;6(4):293–9.

49.	Uemura A, Mizota A. Retinal Concentration and Protective Effect against Retinal Ischemia of Nilvadipine in Rats. Eur J Ophthalmol. 2008;18(1):87–93.

50.   Toriu N, Akaike A, Yasuyoshi H, Zhang S, Kashii S, Honda Y, et al. Lomerizine, a Ca2+Channel Blocker, Reduces Glutamate-induced Neurotoxicity and Ischemia/Reperfusion Damage in Rat Retina. Exp Eye Res. 2000;70(4):475–84.

51.   Netland PA, Chaturvedi N, Dreyer EB. Calcium channel blockers in the management of low-tension and open-angle glaucoma. Am J Ophthalmol. 1993;115(5):608–13.

52.   Ishida K, Yamamoto T, Kitazawa Y. Clinical factors associated with progression of normal-tension glaucoma. J Glaucoma. 1998;7(6):372–7.

53.   Liu S, Araujo S V, Spaeth GL, Katz LJ, Smith M. Lack of effect of calcium channel blockers on open-angle glaucoma. J Glaucoma. 1996;5(3):187–90.

54.   Daugeliene L, Kitazawa Y, Yamamoto T. Risk factors for visual field damage progression in normal-tension glaucoma eyes. Graefes Arch Clin Exp Ophthalmol. 1999;237(2):105–8.

55.   Müskens RPHM, de Voogd S, Wolfs RCW, Witteman JCM, Hofman A, de Jong PTVM, et al. Systemic Antihypertensive Medication and Incident Open-angle Glaucoma. Ophthalmology. 2007;114(12):2221–6.

56.   Langman MJS, Lancashire RJ, Cheng KK. Systemic hypertension and glaucoma: mechanisms in common and co-occurrence. Br J Ophthalmol. 2005;89:960–3.

57.   White A, Heller J, Leung J, Tassoni A, Martin K. Retinal ganglion cell neuroprotection by an angiotensin II blocker in an ex vivo retinal explant model. J Renin Angiotensin Aldosterone Syst. 2015;16(4):1193–201.

58.   Semba K, Namekata K, Guo X, Harada C, Harada T, Mitamura Y. Renin–angiotensin system regulates neurodegeneration in a mouse model of normal tension glaucoma. Cell Death Dis. 2014;5:1–11.

59.   Yang H, Hirooka K, Fukuda K, Shiraga F. Neuroprotective Effects of Angiotensin II Type 1 Receptor Blocker in a Rat Model of Chronic Glaucoma. Invest Ophthalmol Vis

Sci. 2009;50(12):5800–4.

60. Wang R-F, Podos SM, Mittag TW, Yokoyoma T. Effect of CS-088, an angiotensin AT 1 receptor antagonist, on intraocular pressure in glaucomatous monkey eyes. Exp Eye Res. 2005;80:629–32.

61. Lopez Sanchez MIG, Crowston JG, Mackey DA, Trounce IA. Emerging Mitochondrial Therapeutic Targets in Optic Neuropathies. Pharmacol Ther. 2016;165:132–52.

62. Khatib T, Martin K. Protecting retinal ganglion cells. Eye. 2017;31:218–24.

63. Sena D, Lindsley K. Neuroprotection for treatment of glaucoma in adults (Review). Cochrane Database Syst Rev. 2017;(1):1–34.

64. Evans DW, Hosking SL, Gherghel D, Bartlett JD, Hosking SL. Contrast sensitivity improves after brimonidine therapy in primary open angle glaucoma: a case for neuroprotection. Br J Ophthalmol. 2003;87:1463–5.

65. Loon SC, Liew G, Fung A, Reid SE, Craig JC. Meta-analysis of randomized controlled trials comparing timolol with brimonidine in the treatment of glaucoma. Clin Exp Ophthalmol. 2008;36(3):281–9.

66. Tsai J-C, Chang H-W. Comparison of the Effects of Brimonidine 0.2% and Timolol 0.5% on Retinal Nerve Fiber Layer Thickness in Ocular Hypertensive Patients: A Prospective, Unmasked Study. J Ocul Pharmacol Ther. 2005;21(6):475–82.

67. Hare W, Woldemussie E, Lai R, Ton H, Ruiz G, Feldmann B, et al. Efficacy and Safety of Memantine, an NMDA-Type Open-Channel Blocker, for Reduction of Retinal Injury Associated with Experimental Glaucoma in Rat and Monkey. Surv Ophthalmol. 2001;45(Supplement 3):S284–9.

68. Yücel YH, Gupta N, Zhang Q, Mizisin AP, Kalichman MW, Weinreb RN. Memantine Protects Neurons From Shrinkage in the Lateral Geniculate Nucleus in Experimental

Glaucoma. Arch Ophthalmol. 2006;124(2):217–25.

69.   Allergan Inc. Allergan reports fourth quarter operating results [press release].
       [Internet]. [cited 2018 Apr 10]. Available from:
       https://www.businesswire.com/news/home/20080130005272/en/Allergan-Reports-
       Fourth-Quarter-Operating-Results

70.   Ishikawa M, Yoshitomi T, Zorumski CF, Izumi Y. Experimentally induced
       mammalian models of glaucoma. Biomed Res Int. 2015;1–12.

71.   Chen S, Zhang X. The Rodent Model of Glaucoma and Its Implications. Asia Pac J
       Ophthalmol. 2015;4(4):236–41.

72.   Bouhenni RA, Dunmire J, Sewell A, Edward DP. Animal models of glaucoma. J
       Biomed Biotechnol. 2012;1–11.

73.   Vidal-Sanz M, Salinas-Navarro M, Nadal-Nicolás FM, Alarcón-Martínez L, Valiente-
       Soriano FJ, Miralles de Imperial J, et al. Understanding glaucomatous damage:
       Anatomical and functional data from ocular hypertensive rodent retinas. Prog Retin
       Eye Res. 2012;31(1):1–27.

74.   Peters LL, Robledo RF, Bult CJ, Churchill GA, Paigen BJ, Svenson KL. The mouse as
       a model for human biology: a resource guide for complex trait analysis. Nat Rev
       Genet. 2007;8(1):58–69.

75.   Zhou Y, Grinchuk O, Tomarev SI. Transgenic Mice Expressing the Tyr437His Mutant
       of Human Myocilin Protein Develop Glaucoma. Invest Ophthalmol Vis Sci.
       2008;49(5):1932–9.

76.   Mabuchi F, Lindsey JD, Aihara M, Mackey MR, Weinreb RN. Optic Nerve Damage in
       Mice with a Targeted Type I Collagen Mutation. Invest Ophthalmol Vis Sci.
       2004;45(6):1841–5.

77.   Ittner LM, Schwerdtfeger K, Kunz TH, Muff R, Husmann K, Grimm C, et al.

Transgenic mice with ocular overexpression of an adrenomedullin receptor reflect human acute angle-closure glaucoma. Clin Sci. 2008;114(1):49–58.

78.   Anderson MG, Smith RS, Savinova O V, Hawes NL, Chang B, Zabaleta A, et al. Genetic modification of glaucoma associated phenotypes between AKXD-28/Ty and DBA/2J mice. BMC Genet. 2001;2(1).

79.   John SW, Smith RS, Savinova O V, Hawes NL, Chang B, Turnbull D, et al. Essential iris atrophy, pigment dispersion, and glaucoma in DBA/2J mice. Invest Ophthalmol Vis Sci. 1998;39(6):951–62.

80.   Anderson MG, Smith RS, Hawes NL, Zabaleta A, Chang B, Wiggs JL, et al. Mutations in genes encoding melanosomal proteins cause pigmentary glaucoma in DBA/2J mice. Nat Genet. 2002;30(1):81–5.

81.   Büchi ER, Suivaizdis I, Fu J. Pressure-Induced Retinal Ischemia in Rats: An Experimental Model for Quantitative Study. Ophthalmologica. 1991;203(3):138–47.

82.   Sellés-Navarro I, Villegas-Pérez MP, Salvador-Silva M, Ruiz-Gómez JM, Vidal-Sanz M, Villegas-Pérez MP, et al. Retinal ganglion cell death after different transient periods of pressure-induced ischemia and survival intervals. A quantitative in vivo study. Invest Ophthalmol Vis Sci. 1996;37(10):2002–14.

83.   Adachi M, Takahashi K, Nishikawa M, Miki H, Uyama M. High intraocular pressure-induced ischemia and reperfusion injury in the optic nerve and retina in rats. Vol. 234, Graefe's Arch Clin Exp Ophthalmol. 1996.

84.   Büchi ER. Cell death in rat retina after pressure-induced ischaemia-reperfusion insult: electron microscopic study. II. Outer nuclear layer. Jpn J Ophthalmol. 1992;36(1):62–8.

85.   Büchi ER. Cell death in the rat retina after a pressure-induced ischaemia-reperfusion insult: An electron microscopic study. I. Ganglion cell layer and inner nuclear layer.

Exp Eye Res. 1992 Oct 1;55(4):605–13.

86.   Levkovitch-Verbin H, Quigley HA, Martin KRG, Valenta D, Baumrind LA, Pease ME. Translimbal laser photocoagulation to the trabecular meshwork as a model of glaucoma in rats. Invest Ophthalmol Vis Sci. 2002;43(2):402–10.

87.   WoldeMussie E, Ruiz G, Wijono M, Wheeler LA. Neuroprotection of retinal ganglion cells by brimonidine in rats with laser-induced chronic ocular hypertension. Invest Ophthalmol Vis Sci. 2001;42(12):2849–55.

88.   Aihara M, Lindsey JD, Weinreb RN. Experimental Mouse Ocular Hypertension: Establishment of the Model. Invest Ophthalmol Vis Sci. 2003;44(10):4314–20.

89.   Gross RL, Ji J, Chang P, Pennesi ME, Bs Y, Zhang J, et al. A mouse model of elevated intraocular pressure: retina and optic nerve findings. Trans Am Ophthalmol Soc. 2003;101:163–72.

90.   Grozdanic SD, Betts DM, Sakaguchi DS, Allbaugh RA, Kwon YH, Kardon RH. Laser-Induced Mouse Model of Chronic Ocular Hypertension. Invest Ophthalmol Vis Sci. 2003 Oct;44(10):4337–46.

91.   Chen H, Wei X, Cho K-S, Chen G, Sappington R, Calkins DJ, et al. Optic Neuropathy Due to Microbead-Induced Elevated Intraocular Pressure in the Mouse. Invest Ophthalmol Vis Sci. 2011;52(1):36–44.

92.   Sappington RM, Carlson BJ, Crish SD, Calkins DJ. The Microbead Occlusion Model: A Paradigm for Induced Ocular Hypertension in Rats and Mice. Invest Ophthalmol Vis Sci. 2010;51(1):207–16.

93.   Samsel PA, Kisiswa L, Erichsen JT, Cross SD, Morgan JE. A Novel Method for the Induction of Experimental Glaucoma Using Magnetic Microspheres. Invest Ophthalmol Vis Sci. 2011;52(3):1671–5.

94.   Fortune B, Bui B V., Morrison JC, Johnson EC, Dong J, Cepurna WO, et al. Selective

Ganglion Cell Functional Loss in Rats with Experimental Glaucoma. Invest Ophthalmol Vis Sci. 2004;45(6):1854–62.

95.   Nissirios N, Chanis R, Johnson E, Morrison J, Cepurna WO, Jia L, et al. Comparison of Anterior Segment Structures in Two Rat Glaucoma Models: An Ultrasound Biomicroscopic Study. Invest Ophthalmol Vis Sci. 2008;49(6):2478–82.

96.   Chauhan B, Pan J, Archibald ML, LeVatte TL, Kelly MEM, Tremblay F. Effect of intraocular pressure on optic disc topography, electroretinography, and axonal loss in a chronic pressure-induced rat model of optic nerve damage. Invest Ophthalmol Vis Sci. 2002;43(9):2969–76.

97.   Liu HH, Bui B V., Nguyen CTO, Kezic JM, Vingrys AJ, He Z. Chronic ocular hypertension induced by circumlimbal suture in rats. Invest Ophthalmol Vis Sci. 2015;56(2):2811–20.

98.   Daniel S, Clark AF, Mcdowell CM. Subtype-specific response of retinal ganglion cells to optic nerve crush. Cell Death Discov. 2018;4:1–16.

99.   Berkelaar M, Clarke DB, Wang Y-C, Bray GM, Aguayo AJ. Axotomy Results in Delayed Death and Apoptosis of Retinal Ganglion Cells in Adult Rats. J Neurosci. 1994;14(7):4368–74.

100. Levkovitch-Verbin H, Harris–Cerruti C, Groner Y, Wheeler LA, Schwartz M, Yoles E. RGC Death in Mice after Optic Nerve Crush Injury: Oxidative Stress and Neuroprotection. Vol. 41, Invest Ophthalmol Vis Sci. 2000. 4169–4174 p.

101. Solomon AS, Lavie V, Hauben U, Monsonego A, Yoles E, Schwartz M. Complete transection of rat optic nerve while sparing the meninges and the vasculature: an experimental model for optic nerve neuropathy and trauma. J Neurosci Methods. 1996;70:21–5.

102. Lotery AJ. Glutamate excitotoxicity in glaucoma: truth or fiction? Eye.

2005;19(4):369–70.

103. Lam TT, Abler AS, Kwong JMK, Tso MOM. N-Methyl-D-Aspartate (NMDA)–Induced Apoptosis in Rat Retina. Invest Ophthalmol Vis Sci. 1999 Sep;40(10):2391–7.

104. Sisk DR, Kuwabara T. Histologic changes in the inner retina of albino rats following intravitreal injection of monosodium L-glutamate. Graefe's Arch Clin Exp Ophthalmol. 1985;223:250–8.

105. Turner AJ, Vander Wall R, Gupta V, Klistorner A, Graham SL. DBA/2J mouse model for experimental glaucoma: pitfalls and problems. Clin Exp Ophthalmol. 2017;45(9):911–22.

106. Buckingham BP, Inman DM, Lambert W, Oglesby E, Calkins DJ, Steele MR, et al. Progressive Ganglion Cell Degeneration Precedes Neuronal Loss in a Mouse Model of Glaucoma. Neurobiol Dis. 2008;28(11):2735–44.

107. Mead B, Thompson A, Scheven BA, Logan A, Berry M, Leadbeater W. Comparative Evaluation of Methods for Estimating Retinal Ganglion Cell Loss in Retinal Sections and Wholemounts. Badea TC, editor. PLoS One. 2014;9(10):1–9.

108. Nadal-Nicola´s FM, Jime´nez-Lo´pez M, Sobrado-Calvo P, Nieto-Lo´pez L, Ca´novas-Martínez I, Salinas-Navarro M, et al. Brn3a as a Marker of Retinal Ganglion Cells: Qualitative and Quantitative Time Course Studies in Naïve and Optic Nerve–Injured Retinas. Invest Ophthalmol Vis Sci. 2009;50(8):3860–8.

109. Rodriguez AR, de Sevilla Müller LP, Brecha NC. The RNA binding protein RBPMS is a selective marker of ganglion cells in the mammalian retina. J Comp Neurol. 2014;522(6):1411–43.

110. Kwong JMK, Quan A, Kyung H, Piri N, Caprioli J. Quantitative Analysis of Retinal Ganglion Cell Survival with Rbpms Immunolabeling in Animal Models of Optic Neuropathies. Invest Ophthalmol Vis Sci. 2011;52(13):9694–702.

111. Surgucheva I, Weisman AD, Goldberg JL, Shnyra A, Surguchov A. γ-Synuclein as a marker of retinal ganglion cells. Mol Vis. 2008;14:1540–8.

112. Leung CK-S, Weinreb RN. Experimental detection of retinal ganglion cell damage in vivo. Exp Eye Res. 2009;88(4):831–6.

113. Smith CA, Chauhan BC. In vivo imaging of adeno-associated viral vector labelled retinal ganglion cells. Sci Rep. 2018;8(1):1490.

114. Peinado-Ramon P, Salvador M, Villegas-Pérez MP, Vidal-Sanz M. Effects of axotomy and intraocular administration of NT-4, NT-3, and brain derived neurotrophic factor on the survival of adult rat retinal ganglion cells: A quantitative in vivo study. Invest Ophthalmol Vis Sci. 1996;37(4):489–500.

115. Thanos S. Specific transcellular carbocyanine-labelling of rat retinal microglia during injury-induced neuronal degeneration. Neurosci Lett. 1991;127:108–12.

116. Thanos S. The Relationship of Microglial Cells to Dying Neurons During Natural Neuronal Cell Death and Axotomy-induced Degeneration of the Rat Retina. Eur J Neurosci. 1991;3:1189–207.

117. Danias J, Lee KC, Zamora M-F, Chen B, Shen F, Filippopoulos T, et al. Quantitative Analysis of Retinal Ganglion Cell (RGC) Loss in Aging DBA/2NNia Glaucomatous Mice: Comparison with RGC Loss in Aging C57/BL6 Mice. Invest Ophthalmol Vis Sci. 2003;44(12):5151–62.

118. Schlamp CL, Montgomery AD, Mac Nair CE, Schluart C, Willmer DJ, Nickells RW. Evaluation of the percentage of ganglion cells in the ganglion cell layer of the rodent retina. Mol Vis. 2013;19:1387–96.

119. Geeraerts E, Dekeyster E, Gaublomme D, Salinas-Navarro M, De Groef L, Moons L. A freely available semi-automated method for quantifying retinal ganglion cells in entire retinal flatmounts. Exp Eye Res. 2016;147:105–13.

120. Nadal-Nicolás FM, Jiménez-López M, Salinas-Navarro M, Sobrado- Calvo P, Alburquerque-Bejar JJ, Vidal-Sanz M, et al. Whole Number, Distribution and Co-Expression of Brn3 Transcription Factors in Retinal Ganglion Cells of Adult Albino and Pigmented Rats. PLoS One. 2012;7(11):1–16.

121. Danias J, Shen F, Goldblum D, Chen B, Ramos-Esteban J, Podos SM, et al. Cytocarchitecture of the Retinal Ganglion Cells in the Rat. Invest Ophthalmol Vis Sci. 2002;43(3):587–94.

122. Inman DM, Sappington RM, Horner PJ, Calkins DJ. Quantitative Correlation of Optic Nerve Pathology with Ocular Pressure and Corneal Thickness in the DBA/2 Mouse Model of Glaucoma. Invest Ophthalmol Vis Sci. 2006;47(3):986–96.

123. Kerrison JB, Buchanan K, Rosenberg ML, Clark R, Andreason K, Alfaro D V., et al. Quantification of Optic Nerve Axon Loss Associated With a Relative Afferent Pupillary Defect in the Monkey. Arch Ophthalmol. 2001;119(9):1333–41.

124. Yücel Y, Kalichman M, Mizisin A, Powell H, Weinreb R. Histomorphometric analysis of optic nerve changes in experimental glaucoma. J Glaucoma. 1999;8(1):38–45.

125. Mabuchi F, Aihara M, Mackey MR, Lindsey JD, Weinreb RN. Optic Nerve Damage in Experimental Mouse Ocular Hypertension. Invest Ophthalmol Vis Sci. 2003;44(10):4321–30.

126. Li Y, Schlamp CL, Nickells RW. Experimental induction of retinal ganglion cell death in mice. Invest Ophthalmol Vis Sci. 1999;40(5):1004–8.

127. Salinas-Navarro M, Mayor-Torroglosa S, Jiménez-López M, Avilés-Trigueros M, Holmes TM, Lund RD, et al. A computerized analysis of the entire retinal ganglion cell population and its spatial distribution in adult rats. Vision Res. 2009;49:115–26.

128. Dordea AC, Bray M-A, Allen K, Logan DJ, Fei F, Malhotra R, et al. An open-source computational tool to automatically quantify immunolabeled retinal ganglion cells.

Exp Eye Res. 2016;147:50–6.

129. Chidlow G, Osborne NN. Rat retinal ganglion cell loss caused by kainate, NMDA and ischemia correlates with a reduction in mRNA and protein of Thy-1 and neurofilament light. Brain Res. 2003;963:298–306.

130. Hoffman PN, Pollock SC, Striph GG. Altered Gene Expression after Optic Nerve Transection: Reduced Neurofilament Expression as a General Response to Axonal Injury. Exp Neurol. 1993;119:32–6.

131. Huang W, Fileta J, Guo Y, Grosskreutz CL. Downregulation of Thy1 in Retinal Ganglion Cells in Experimental Glaucoma. Curr Eye Res. 2006;313(31):265–71.

132. Nash MS, Osborne NN. Assessment of Thy-1 mRNA levels as an index of retinal ganglion cell damage. Invest Ophthalmol Vis Sci. 1999;40(6):1293–8.

133. Schlamp CL, Johnson EC, Li Y, Morrison JC, Nickells RW. Changes in Thy1 gene expression associated with damaged retinal ganglion cells. Mol Vis. 2001;7:192–201.

134. Yang J, Tezel G, Patil R V, Wax MB. Flow cytometry for quantification of retrogradely labeled retinal ganglion cells by Fluoro-Gold. Curr Eye Res. 2000;21(6):981–5.

135. Higashide T, Kawaguchi I, Ohkubo S, Takeda H, Sugiyama K. In Vivo Imaging and Counting of Rat Retinal Ganglion Cells Using a Scanning Laser Ophthalmoscope. Invest Ophthalmol Vis Sci. 2006;47(7):2943–50.

136. Rovere G, Nadal-Nicolás FM, Agudo-Barriuso M, Sobrado-Calvo P, Nieto-López L, Nucci C, et al. Comparison of Retinal Nerve Fiber Layer Thinning and Retinal Ganglion Cell Loss After Optic Nerve Transection in Adult Albino Rats. Invest Ophthalmol Vis Sci. 2015;56(8):4487–98.

137. Yi J, Puyang Z, Feng L, Duan L, Liang P, Backman V, et al. Optical Detection of Early Damage in Retinal Ganglion Cells in a Mouse Model of Partial Optic Nerve

Crush Injury. Invest Ophthalmol Vis Sci. 2016;57(13):5665–71.

138. Burgoyne CF, Morrison JC. The anatomy and pathophysiology of the optic nerve head in glaucoma. J Glaucoma. 2001;10(5):S16–8.

139. Yablonski ME, Asamoto A. Hypothesis concerning the pathophysiology of optic nerve damage in open angle glaucoma. J Glaucoma. 1993;2(2):119–27.

140. Calkins DJ. Critical pathogenic events underlying progression of neurodegeneration in glaucoma. Prog Retin Eye Res. 2012;31(6):702–19.

141. Fechtner RD, Weinreb RN. Mechanisms of Optic Nerve Damage in Primary Open Angle Glaucoma. Surv Ophthalmol. 1994;39(1):23–42.

142. Hayreh SS. Blood supply of the optic nerve head and its role in optic atrophy, glaucoma, and oedema of the optic disc. Br J Ophthalmol. 1969;53(11):721–48.

143. Cherecheanu AP, Garhofer G, Schmidl D, Werkmeister R, Schmetterer L. Ocular perfusion pressure and ocular blood flow in glaucoma. Curr Opin Pharmacol. 2013;13:36–42.

144. Luo X, Shen Y-M, Jiang M-N, Lou X-F, Shen Y. Ocular Blood Flow Autoregulation Mechanisms and Methods. J Ophthalmol. 2015;1–7.

145. Schmidl D, Garhofer G, Schmetterer L. The complex interaction between ocular perfusion pressure and ocular blood flow - Relevance for glaucoma. Exp Eye Res. 2011;93:141–55.

146. Gherghel D, Orgul S, Gugleta K, Gekkieva M, Flammer J. Relationship Between Ocular Perfusion Pressure and Retrobulbar Blood Flow in Patients With Glaucoma With Progressive Damage. Am J Ophthalmol. 2000;130(5):597–605.

147. Fuchsjager-Mayrl G, Wally B, Georgopoulos M, Rainer G, Kircher K, Buehl W, et al. Ocular Blood Flow and Systemic Blood Pressure in Patients with Primary Open-Angle Glaucoma and Ocular Hypertension. Invest Ophthalmol Vis Sci. 2004;45(3):834–9.

148. Garhöfer G, Fuchsjäger-Mayrl G, Vass C, Pemp B, Hommer A, Schmetterer L. Retrobulbar blood flow velocities in open angle glaucoma and their association with mean arterial blood pressure. Invest Ophthalmol Vis Sci. 2010;51(12):6652–7.

149. Polak K, Luksch A, Berisha F, Fuchsjaeger-Mayrl G, Dallinger S, Schmetterer L. Altered Nitric Oxide System in Patients With Open-Angle Glaucoma. Arch Ophthalmol. 2007;125(4):494–8.

150. Resch H, Garhofer G, Fuchsjäger-Mayrl G, Hommer A, Schmetterer L. Endothelial dysfunction in glaucoma. Acta Ophthalmol. 2009;87(1):4–12.

151. Shibata M, Sugiyama T, Kurimoto T, Oku H, Okuno T, Kobayashi T, et al. Involvement of Glial Cells in the Autoregulation of Optic Nerve Head Blood Flow in Rabbits. Invest Ophthalmol Vis Sci. 2012;53(7):3726–32.

152. Hernandez MR. The Optic Nerve Head in Glaucoma: Role of Astrocytes in Tissue Remodeling. Prog Retin Eye Res. 2000;19(3):297–321.

153. Song BJ, Aiello LP, Pasquale LR. Presence and Risk Factors for Glaucoma in Patients with Diabetes. Curr Diab Rep. 2016;16(12):124.

154. Bae HW, Lee N, Sun Lee H, Hong S, Je Seong G, Yun Kim C. Systemic Hypertension as a Risk Factor for Open-Angle Glaucoma: A Meta-Analysis of Population-Based Studies. PLoS One. 2014;9(9):1–9.

155. Gramer G, Weber BHF, Gramer E. Migraine and Vasospasm in Glaucoma: Age-Related Evaluation of 2027 Patients With Glaucoma or Ocular Hypertension. Invest Ophthalmol Vis Sci. 2015;56(13):7999–8007.

156. Mercieca K, Cain J, Hansen T, Steeples L, Watkins A, Spencer F, et al. Primary Open Angle Glaucoma is Associated with MR Biomarkers of Cerebral Small Vessel Disease. Nat Sci Reports. 2016;6(22160):1–6.

157. Casson RJ. Possible role of excitotoxicity in the pathogenesis of glaucoma. Clin Exp

Ophthalmol. 2006 Jan;34(1):54–63.

158. Jonas JB, Mardin CY, Schlotzer-Schrehardt U, Naumann GOH. Morphometry of the human lamina cribrosa surface. Invest Ophthalmol Vis Sci. 1991;32(2):401–5.

159. Abe RY, Gracitelli CPB, Diniz-Filho A, Tatham AJ, Medeiros FA. Lamina Cribrosa in Glaucoma: Diagnosis and Monitoring. Curr Ophthalmol Rep. 2015;3(2):74–84.

160. Hayreh S. Blood Flow in the Optic Nerve Head and Factors that may Influence it. Prog Retin Eye Res. 2001;20(5):595–624.

161. Yan DB, Coloma FM, Metheetrairut A, Trope GE, Heathcote JG, Ethier CR. Deformation of the lamina cribrosa by elevated intraocular pressure. Br J Ophthalmol. 1994;78(8):643–8.

162. Park SC, Kiumehr S, Dorairaj S, Teng CC, Tello C, Liebmann JM, et al. In-vivo, 3-dimensional imaging of the lamina cribrosa horizontal central ridge in normals and lamina cribrosa deformation in glaucoma. Invest Ophthalmol Vis Sci. 2011;52(14):3063–3063.

163. Park H-YL, Jeon SH, Park CK. Enhanced Depth Imaging Detects Lamina Cribrosa Thickness Differences in Normal Tension Glaucoma and Primary Open-Angle Glaucoma. Ophthalmology. 2012;119(1):10–20.

164. Quigley HA, Hohman RM, Addicks EM, Massof RW, Green WR. Morphologic changes in the lamina cribrosa correlated with neural loss in open-angle glaucoma. Am J Ophthalmol. 1983;95(5):673–91.

165. Jonas JB, Berenshtein E, Holbach L. Anatomic Relationship between Lamina Cribrosa, Intraocular Space, and Cerebrospinal Fluid Space. Invest Ophthalmol Vis Sci. 2003;44(12):5189–95.

166. Morgan WH, Yu DY, Alder VA, Cringle SJ, Cooper RL, House PH, et al. The correlation between cerebrospinal fluid pressure and retrolaminar tissue pressure.

Invest Ophthalmol Vis Sci. 1998;39(8):1419–28.

167. The AGIS Investigators. The advanced glaucoma intervention study (AGIS): 7. the relationship between control of intraocular pressure and visual field deterioration. Am J Ophthalmol. 2002;130(4):429–40.

168. Yang H, Downs JC, Girkin C, Sakata L, Bellezza A, Thompson H, et al. 3-D Histomorphometry of the Normal and Early Glaucomatous Monkey Optic Nerve Head: Lamina Cribrosa and Peripapillary Scleral Position and Thickness. Invest Ophthalmol Vis Sci. 2007;48(10):4597–607.

169. Roberts MD, Grau V, Grimm J, Reynaud J, Bellezza AJ, Burgoyne CF, et al. Remodeling of the Connective Tissue Microarchitecture of the Lamina Cribrosa in Early Experimental Glaucoma. Invest Ophthalmol Vis Sci. 2009;50(2):681–90.

170. Downs JC, Roberts MD, Sigal IA. Glaucomatous cupping of the lamina cribrosa: A review of the evidence for active progressive remodeling as a mechanism. Exp Eye Res. 2011;93:133–40.

171. Wang B, Nevins JE, Nadler Z, Wollstein G, Ishikawa H, Bilonick RA, et al. In Vivo Lamina Cribrosa Micro-Architecture in Healthy and Glaucomatous Eyes as Assessed by Optical Coherence Tomography. Invest Ophthalmol Vis Sci. 2013;54(13):8270–4.

172. Susanna R. The lamina cribrosa and visual field defects in open-angle glaucoma. Can J Ophthalmol. 1983;18(3):124–6.

173. Miller KM, Quigley HA. The clinical appearance of the lamina cribrosa as a function of the extent of glaucomatous optic nerve damage. Ophthalmology. 1988;95(1):135–8.

174. Akagi T, Hangai M, Takayama K, Nonaka A, Ooto S, Yoshimura N. In Vivo Imaging of Lamina Cribrosa Pores by Adaptive Optics Scanning Laser Ophthalmoscopy. Invest Ophthalmol Vis Sci. 2012;53(7):4111–9.

175. Radius RL, Gonzales M. Anatomy of the Lamina Cribrosa in Human Eyes. Arch

Ophthalmol. 1981;99(12):2159–62.

176. Quigley HA, Addicks EM. Regional Differences in the Structure of the Lamina Cribrosa and Their Relation to Glaucomatous Optic Nerve Damage. Arch Ophthalmol. 1981;99(1):137–43.

177. Chrysostomou V, Rezania F, Trounce IA, Crowston JG. Oxidative stress and mitochondrial dysfunction in glaucoma. Curr Opin Pharmacol. 2013;13(1):12–5.

178. Kong GYX, Van Bergen NJ, Trounce IA, Crowston JG. Mitochondrial dysfunction and glaucoma. J Glaucoma. 2009;18(2):93–100.

179. Levkovitch-Verbin H. Chapter 2 – Retinal ganglion cell apoptotic pathway in glaucoma: Initiating and downstream mechanisms. In: Progress in Brain Research. Elsevier B.V.; 2015. p. 37–57.

180. Anderson DR. Ultrastructure of Human and Monkey Lamina Cribrosa and Optic Nerve Head. Arch Ophthalmol. 1969;82(6):800–14.

181. Willermain F, Libert S, Motulsky E, Salik D, Caspers L, Perret J, et al. Origins and consequences of hyperosmolar stress in retinal pigmented epithelial cells. Front Physiol. 2014;5:1–8.

182. Williams PA, Harder JM, Foxworth NE, Cochran KE, Philip VM, Porciatti V, et al. Vitamin B3 modulates mitochondrial vulnerability and prevents glaucoma in aged mice. Science (80-). 2017;355(6326):756–60.

183. Andrews RM, Griffiths PG, Johnson MA, Turnbull DM. Histochemical localisation of mitochondrial enzyme activity in human optic nerve and retina. Br J Ophthalmol. 1999;83(2):231–5.

184. Bristow EA, Griffiths PG, Andrews RM, Johnson MA, Turnbull DM. The Distribution of Mitochondrial Activity in Relation to Optic Nerve Structure. Arch Ophthalmol. 2002;120(6):791–6.

185. Laughlin SB, de Ruyter van Steveninck RR, Anderson JC. The metabolic cost of neural information. Nat Neurosci. 1998;1(1):36–41.

186. Osborne N, Casson RJ, Wood JPM, Chidlow G, Graham M, Melena J. Retinal ischemia: mechanisms of damage and potential therapeutic strategies. Prog Retin Eye Res. 2004;23(1):91–147.

187. Casson RJ, Chidlow G, Wood JPM, Osborne NN. The Effect of Hyperglycemia on Experimental Retinal Ischemia. Arch Ophthalmol. 2004;122(3):361–6.

188. Yu D-Y, Cringle SJ. Oxygen Distribution and Consumption within the Retina in Vascularised and Avascular Retinas and in Animal Models of Retinal Disease. Prog Retin Eye Res. 2001;20(2):175–208.

189. Casson RJ, Chidlow G, Wood JPM. Estimate of the adenosine triphosphate requirement of human retinal ganglion cells. Clin Exp Ophthalmol. 2019;47(5):683–4.

190. Noell WK. Studies on the electrophysiology and metabolism of the retina. Sch Aviat Med Rep no1 Randolf Field, Texas. 1953;1–122.

191. Barron MJ, Griffiths P, Turnbull DM, Bates D, Nichols P. The distributions of mitochondria and sodium channels reflect the specific energy requirements and conduction properties of the human optic nerve head. Br J Ophthalmol. 2004;88(2):286–90.

192. Lee S, Sheck L, Crowston JG, Van Bergen NJ, O'Neill EC, O'Hare F, et al. Impaired Complex-I-Linked Respiration and ATP Synthesis in Primary Open-Angle Glaucoma Patient Lymphoblasts. Invest Ophthalmol Vis Sci. 2012;53(4):2431–7.

193. Ju W-K, Liu Q, Kim K-Y, Crowston JG, Lindsey JD, Agarwal N, et al. Elevated Hydrostatic Pressure Triggers Mitochondrial Fission and Decreases Cellular ATP in Differentiated RGC-5 Cells. Invest Ophthalmol Vis Sci. 2007;48(5):2145–51.

194. Lee S, Van Bergen NJ, Kong GY, Chrysostomou V, Waugh HS, Neill ECO', et al.

Mitochondrial dysfunction in glaucoma and emerging bioenergetic therapies. Exp Eye Res. 2011;93:204–12.

195. Abu-Amero KK, Morales J, Bosley TM. Mitochondrial Abnormalities in Patients with Primary Open-Angle Glaucoma. Invest Ophthalmol Vis Sci. 2006;47(6):2533–41.

196. Lascaratos G, Chau K-Y, Zhu H, Gkotsi D, King R, Gout I, et al. Resistance to the most common optic neuropathy is associated with systemic mitochondrial efficiency. Neurobiol Dis. 2015;82:78–85.

197. Hegde KR, Kovtun S, Varma SD. Inhibition of glycolysis in the retina by oxidative stress: Prevention by pyruvate. Mol Cell Biochem. 2010;343:101–5.

198. Hegde KR, Varma SD. Prevention of Oxidative Stress to the Retina by Pyruvate A Preliminary Report. Ophthalmologica. 2008;222:194–8.

199. Dong X-X, Wang Y, Qin Z-H. Molecular mechanisms of excitotoxicity and their relevance to pathogenesis of neurodegenerative diseases. Acta Pharmacol Sin. 2009;30(4):379–87.

200. Ebneter A, Chidlow G, Wood JPM, Casson RJ. Protection of Retinal Ganglion Cells and the Optic Nerve During Short-term Hyperglycemia in Experimental Glaucoma. Arch Ophthalmol. 2011;129(10):1337–44.

201. Winkler BS. Glycolytic and Oxidative Metabolism in Relation to Retinal Function. J Gen Physiol. 1981;77(6):667–92.

202. Ng SK, Wood JPM, Chidlow G, Han G, Kittipassorn T, Peet DJ, et al. Cancer-like metabolism of the mammalian retina. Clin Exp Ophthalmol. 2015;43(4):367–76.

203. Holman MC, Chidlow G, Wood JPM, Casson RJ. The Effect of Hyperglycemia on Hypoperfusion-Induced Injury. Invest Ophthalmol Vis Sci. 2010;51(4):2197–207.

204. Casson RJ, Han G, Ebneter A, Chidlow G, Glihotra J, Newland H, et al. Glucose-Induced Temporary Visual Recovery in Primary Open-Angle Glaucoma: A Double-

Blind, Randomized Study. Ophthalmology. 2014;121(6):1203–11.

205. Zilberter Y, Gubkina O, Ivanov AI, Magistretti PJ, Schurr A. A unique array of neuroprotective effects of pyruvate in neuropathology. Front Neurosci. 2015;9(17):1–5.

206. Williams PA, Harder JM, John SWM. Glaucoma as a Metabolic Optic Neuropathy: Making the Case for Nicotinamide Treatment in Glaucoma. J Glaucoma. 2017;26(12):1161–8.

207. Revollo JR, Grimm AA, Imai S. The NAD Biosynthesis Pathway Mediated by Nicotinamide Phosphoribosyltransferase Regulates Sir2 Activity in Mammalian Cells. J Biol Chem. 2004;279(49):50754–63.

208. Avalos JL, Bever KM, Wolberger C. Mechanism of sirtuin nhibition by nicotinamide: Altering the NAD + cosubstrate specificity of a Sir2 enzyme. Mol Cell. 2005;17(6):855–68.

209. Bitterman KJ, Anderson RM, Cohen HY, Latorre-Esteves M, Sinclair DA. Inhibition of silencing and accelerated aging by nicotinamide, a putative negative regulator of yeast sir2 and human SIRT1. J Biol Chem. 2002;277(47):45099–107.

210. Whitmore A V, Libby RT, John SWM. Glaucoma: Thinking in new ways—a roîe for autonomous axonal self-destruction and other compartmentalised processes? Prog Retin Eye Res. 2005;24:639–62.

211. Kaushik S, Pandav SS, Ram J. Neuroprotection in glaucoma. J Postgrad Med. 2003;49(1):90–5.

212. Pasquale LR. Vascular and Autonomic Dysregulation in Primary Open-Angle Glaucoma. Curr Opin Ophthalmol. 2016;27(2):94–101.

213. Mokudai T, Ayoub IA, Sakakibara Y, Lee EJ, Ogilvy CS, Maynard KI. Delayed treatment with nicotinamide (Vitamin B(3)) improves neurological outcome and

reduces infarct volume after transient focal cerebral ischemia in Wistar rats. Stroke. 2000;31(7):1679–85.

214. Verdin E. NAD$^+$ in aging, metabolism, and neurodegeneration. Science (80-). 2015;350(6265):1208–13.

215. Williams PA, Harder JM, Foxworth NE, Cardozo BH, Cochran KE, John SWM. Nicotinamide and WLDS act together to prevent neurodegeneration in glaucoma. Front Neurosci. 2017;11:1–10.

216. Conforti L, Gilley J, Coleman MP. Wallerian degeneration: an emerging axon death pathway linking injury and disease. Nat Rev Neurosci. 2014;15:394–409.

217. Hui F, Tang J, Williams PA, McGuinness MB, Hadoux X, Casson RJ, et al. Improvement in inner retinal function in glaucoma with nicotinamide (vitamin B3) supplementation: A crossover randomized clinical trial. Clin Exp Ophthalmol. 2020 Sep 28;48(7):903–14.

218. Pellerin L. Lactate as a pivotal element in neuron–glia metabolic cooperation. Neurochem Int. 2003;43:331–8.

219. Castillo X, Rosafio K, Wyss MT, Drandarov K, Buck A, Pellerin L, et al. A probable dual mode of action for both L-and D-lactate neuroprotection in cerebral ischemia. J Cereb Blood Flow Metab. 2015;35:1561–9.

220. Tekkök SB, Brown AM, Westenbroek R, Pellerin L, Ransom BR. Transfer of glycogen-derived lactate from astrocytes to axons via specific monocarboxylate transporters supports mouse optic nerve activity. J Neurosci Res. 2005;81(5):644–52.

221. Poitry-Yamate CL, Poitry S, Tsacopoulos M. Lactate released by Müller glial cells is metabolized by photoreceptors from mammalian retina. J Neurosci. 1995;15(7):5179–91.

222. Poitry S, Poitry-Yamate C, Ueberfeld J, MacLeish PR, Tsacopoulos M. Mechanisms

of glutamate metabolic signaling in retinal glial (Müller) cells. J Neurosci. 2000;20(5):1809–21.

223. Hurley JB, Lindsay KJ, Du J. Glucose, Lactate, and Shuttling of Metabolites in Vertebrate Retinas. J Neurosci Res. 2015;93(7):1079–92.

224. Kanow MA, Giarmarco MM, Jankowski CS, Tsantilas K, Engel AL, Du J, et al. Biochemical adaptations of the retina and retinal pigment epithelium support a metabolic ecosystem in the vertebrate eye. Elife. 2017;6:1–25.

225. Vecino E, Rodriguez FD, Ruzafa N, Pereiro X, Sharma SC. Glia-neuron interactions in the mammalian retina. Prog Retin Eye Res. 2016;51:1–40.

226. Shirley Ding S, Leow S, Munisvaradass R, Koh E, Bastion M, Then K, et al. Revisiting the role of erythropoietin for treatment of ocular disorders. Eye. 2016;30:1293–309.

227. Szabo A, Vegvari D, Deak G, Lukats A, Berta A, Szel A. The Expression of Erythropoietin and Its Receptor in the Developing Rat Retina. Invest Ophthalmol Vis Sci. 2008;49(13):5896.

228. Zhong L, Bradley J, Schubert W, Ahmed E, Adamis AP, Shima DT, et al. Erythropoietin Promotes Survival of Retinal Ganglion Cells in DBA/2J Glaucoma Mice. Invest Ophthalmol Vis Sci. 2007;48(3):1212–8.

229. Zhong Y-S, Liu X-H, Cheng Y, Min Y-J. Erythropoietin with Retrobulbar Administration Protects Retinal Ganglion Cells from Acute Elevated Intraocular Pressure in Rats. J Ocul Pharmacol Ther. 2008;24(5):453–9.

230. King CE, Rodger J, Bartlett C, Esmaili T, Dunlop SA, Beazley LD. Erythropoietin is both neuroprotective and neuroregenerative following optic nerve transection. Exp Neurol . 2007;205:48–55.

231. Borhani-Haghighi A, Ghodsi M, Razeghinejad MR, Mardani S, Mardani M,

Nikseresht AR, et al. Erythropoietin for acute multiple sclerosis in patients with optic neuritis as a first demyelination event. Neurosciences. 2012;17(2):151–5.

232. Sühs K-W, Hein K, Sättler MB, Görlitz A, Ciupka C, Scholz K, et al. A randomized, double-blind, phase 2 study of erythropoietin in optic neuritis. Ann Neurol. 2012;72(2):199–210.

233. Shayegannejad V, Shahzamani S, Dehghani A, Dast Borhan Z, Rahimi M, Mirmohammadsadeghi A. A double-blind, placebo-controlled trial of adding erythropoietin to intravenous methylprednisolone for the treatment of unilateral acute optic neuritis of unknown or demyelinative origin. Graefes Arch Clin Exp Ophthalmol. 2015;253(5):797–801.

234. Kashkouli MB, Pakdel F, Sanjari MS, Haghighi A, Nojomi M, Homaee MH, et al. Erythropoietin: a novel treatment for traumatic optic neuropathy—a pilot study. Graefes Arch Clin Exp Ophthalmol. 2011;249(5):731–6.

235. Burmester T, Gerlach F, Hankeln T. Hypoxia and the Circulation. Chapter 13: Regulation and Role of Neuroglobin and Cytoglobin under Hypoxia. Roach R, et. al., editors. New York: Springer; 2007. 169–180 p.

236. Ostojić J, Grozdanić SD, Syed NA, Hargrove MS, Trent JT, Kuehn MH, et al. Patterns of Distribution of Oxygen-Binding Globins, Neuroglobin and Cytoglobin in Human Retina. Arch Ophthalmol. 2008;126(11):1530–6.

237. Lechauve C, Augustin S, Roussel D, Sahel J-A, Corral-Debrinski M. Neuroglobin involvement in visual pathways through the optic nerve. Biochim Biophys Acta. 2013;1834(9):1772–8.

238. Chan ASY, Saraswathy S, Rehak M, Ueki M, Rao NA. Neuroglobin Protection in Retinal Ischemia. Invest Ophthalmol Vis Sci. 2012;53(2):704–11.

239. Wei X, Yu Z, Cho K-S, Chen H, Taimur M, Malik A, et al. Neuroglobin Is an

Endogenous Neuroprotectant for Retinal Ganglion Cells against Glaucomatous Damage. Am J Pathol. 2011;179(6):2788–97.

240.   Cwerman-Thibault H, Lechauve C, Augustin S, Roussel D, Reboussin E, Mohammad A, et al. Neuroglobin Can Prevent or Reverse Glaucomatous Progression in DBA/2J Mice. Mol Ther Methods Clin Dev. 2017;5:200–20.

241.   Sugitani K, Koriyama Y, Sera M, Arai K, Ogai K, Wakasugi K. A novel function of neuroglobin for neuroregeneration in mice after optic nerve injury. Biochem Biophys Res Commun. 2017;493:1254–9.

242.   Kruger NJ, Von Schaewen A. The oxidative pentose phosphate pathway: structure and organisation. Curr Opin Plant Biol. 2003;6:236–46.

243.   Almeida A, Cidad P, Delgado-Esteban M, Fernández E, García-Nogales P, Bolaños JP. Inhibition of mitochondrial respiration by nitric oxide: Its role in glucose metabolism and neuroprotection. J Neurosci Res. 2005;79:166–71.

244.   Hsus S-C, Molday RS. Glucose Metabolism in Photoreceptor Outer Segments. Its role in phototransduction and in NADPH-requiring reactions. J Biol Chem. 1994;269(27):17954–9.

245.   Han G, Wood JPM, Chidlow G, Mammone T, Casson RJ. Mechanisms of Neuroprotection by Glucose in Rat Retinal Cell Cultures Subjected to Respiratory Inhibition. Invest Ophthalmol Vis Sci. 2013;54(12):7567–77.

246.   Winkler BS, Arnold MJ, Brassell MA, Sliter DR. Glucose dependence of glycolysis, hexose monophosphate shunt activity, energy status, and the polyol pathway in retinas isolated from normal (nondiabetic) rats. Invest Ophthalmol Vis Sci. 1997;38(1):62–71.

247.   Shibeeb O, Chidlow G, Han G, Wood JP, Casson RJ. Effect of subconjunctival glucose on retinal ganglion cell survival in experimental retinal ischaemia and contrast sensitivity in human glaucoma. Clin Exp Ophthalmol. 2016;44(1):24–32.

248.	Yuen HK, Princen J, Lllingworth J, Kittler J. Comparative study of Hough Transform methods for circle finding. Image Vis Comput. 1990;8(1):71–7.

249.	Davies ER. Machine vision : theory, algorithms, practicalities. Third Edition, Chapter 10. Morgan Kauffman Publishers; 2005.

250.	Deroulers C, Ameisen D, Badoual M, Gerin C, Granier A, Lartaud M. Analyzing huge pathology images with open source software. Diagn Pathol. 2013;8:92.

251.	Onakpoya I, Hunt K, Wider B, Ernst E. Pyruvate Supplementation for Weight Loss: A Systematic Review and Meta-Analysis of Randomized Clinical Trials. Crit Rev Food Sci Nutr. 2014;54(1):17–23.

252.	Casson RJ, Wood JPM, Han G, Kittipassorn T, Peet DJ, Chidlow G. M-Type Pyruvate Kinase Isoforms and Lactate Implications. Invest Ophthalmol Vis Sci. 2016;57:66–80.

253.	Chidlow G, Wood JPM, Sia PI, Casson RJ. Distribution and Activity of Mitochondrial Proteins in Vascular and Avascular Retinas: Implications for Retinal Metabolism. Invest Ophthalmol Vis Sci. 2019;60:331–44.

254.	Choi J-S, Lee MS, Jeong J-W. Ethyl pyruvate has a neuroprotective effect through activation of extracellular signal-regulated kinase in Parkinson's disease model. Biochem Biophys Res Commun. 2010;394:854–8.

255.	Yu YM, Kim J Bin, Lee KW, Kim SY, Han PL, Lee JK. Inhibition of the cerebral ischemic injury by ethyl pyruvate with a wide therapeutic window. Stroke. 2005;36(10):2238–43.

256.	Kim J-B, Yu Y-M, Kim S-W, Lee J-K. Anti-inflammatory mechanism is involved in ethyl pyruvate-mediated efficacious neuroprotection in the postischemic brain. Brain Res. 2005;1060:188–92.

257.	Yoo MH, Lee J-Y, Lee SE, Koh J-Y, Yoon YH. Protection by Pyruvate of Rat Retinal Cells against Zinc Toxicity In Vitro, and Pressure-Induced Ischemia In Vivo. Invest

Ophthalmol Vis Sci. 2004;45(5):1523–30.

258. Lee J-Y, Kim Y-H, Koh J-Y. Protection by Pyruvate against Transient Forebrain Ischemia in Rats. J Neurosci. 2001;21:1–6.

259. Wang X, Perez E, Liu R, Yan L-J, Mallet RT, Yang S-H. Pyruvate protects mitochondria from oxidative stress in human neuroblastoma SK-N-SH cells. Brain Res. 2007;1132:1–9.

260. Ryu JK, Kim SU, Mclarnon JG. Neuroprotective effects of pyruvate in the quinolinic acid rat model of Huntington's disease. Exp Neurol. 2003;183:700–4.

261. Zlotnik A, Gurevich B, Cherniavsky E, Tkachov S, Matuzani-Ruban A, Leon A, et al. The Contribution of the Blood Glutamate Scavenging Activity of Pyruvate to its Neuroprotective Properties in a Rat Model of Closed Head Injury. Neurochem Res. 2008;33(6):1044–50.

262. Suh SW, Aoyama K, Matsumori Y, Liu J, Swanson RA. Pyruvate administered after severe hypoglycemia reduces neuronal death and cognitive impairment. Diabetes. 2005;54(5):1452–8.

263. Varma SD, Hegde K, Henein M. Oxidative damage to mouse lens in culture. Protective effect of pyruvate. Biochim Biophys Acta. 2003;1621:246–52.

264. Varma SD, Devamanoharan PS, Rutzen AR, Ali AH, Henein M. Attenuation of galactose-induced cataract by pyruvate Attenuation by Pyruvate of Galactose-Induced Cataract. Free Rad Res. 1999;30:253–63.

265. Wood JPM, Mammone T, Chidlow G, Greenwell T, Casson RJ. Mitochondrial Inhibition in Rat Retinal Cell Cultures as a Model of Metabolic Compromise: Mechanisms of Injury and Neuroprotection. Invest Ophthalmol Vis Sci. 2012;53(8):4897–909.

266. Ebneter A, Casson RJ, Wood JPM, Childow G. Microglial activation in the visual

pathway in experimental glaucoma: Spatiotemporal characterization and correlation with axonal injury. Invest Ophthalmol Vis Sci. 2010;51(12):6448–60.

267.   Peng L, Gu L, Zhang H, Huang X, Hertz E, Hertz L. Glutamine as an energy substrate in cultured neurons during glucose deprivation. J Neurosci Res. 2007;85(3):3480–6.

268.   Ebneter A, Casson RJ, Wood JPM, Chidlow G. Estimation of axon counts in a rat model of glaucoma: Comparison of fixed-pattern sampling with targeted sampling. Clin Exp Ophthalmol. 2012;40(6):626–33.

269.   Meller D, Eysel U, Schmidt-Kastner R. Transient immunohistochemical labelling of rat retinal axons during Wallerian degeneration by a monoclonal antibody to neurofilaments. Brain Res. 1994;648:162–6.

270.   Salinas-Navarro M, Alarcó N-Martínez L, Valiente-Soriano FJ, Jimé Nez-Ló Pez M, Mayor-Torroglosa S, Avilé S-Trigueros M, et al. Ocular hypertension impairs optic nerve axonal transport leading to progressive retinal ganglion cell degeneration. Exp Eye Res. 2009;90:168–83.

271.   Beirowski B, Babetto E, Coleman MP, Martin KR. The WldS gene delays axonal but not somatic degeneration in a rat glaucoma model. Eur J Neurosci. 2008;28(6):1166–79.

272.   Bull ND, Irvine K-A, Franklin RJM, Martin KR. Transplanted Oligodendrocyte Precursor Cells Reduce Neurodegeneration in a Model of Glaucoma. Invest Ophthalmol Vis Sci. 2009;50(9):4244–53.

273.   Shetty PK, Sadgrove MP, Galeffi F, Turner DA. Pyruvate incubation enhances glycogen stores and sustains neuronal function during subsequent glucose deprivation. Neurobiol Dis. 2011;45:177–87.

274.   Little C, O'Brien PJ. Mechanism of Peroxide-Inactivation of the Sulphydryl Enzyme G1 yceraldehyde-3-Phosphate Dehydrogenase. Eur J Biochem. 1969;10:533–8.

275. Axelsson K, Mannervik B. An essential role of cytosolic thioltransferase in protection of pyruvate kinase from rabbit liver against oxidative inactivation. FEBS Lett. 1983;152(1):114–8.

276. Wentzel P, Ejdesjö A, Eriksson UJ. Maternal Diabetes In Vivo and High Glucose In Vitro Diminish GAPDH Activity in Rat Embryos. Diabetes. 2003;52:1222–8.

277. Zhao W, Devamanoharan PS, Varma SD. Fructose induced deactivation of antioxidant enzymes: Preventive effect of pyruvate. Free Radic Res. 2000;33(1):23–30.

278. Wang XF, Cynader MS. Pyruvate Released by Astrocytes Protects Neurons from Copper-Catalyzed Cysteine Neurotoxicity. J Neurosci. 2001;21(10):3322–31.

279. Desagher S, Glowinski J. Pyruvate Protects Neurons against Hydrogen. J Neurosci. 1997;17(23):9060–7.

280. Berthet C, Lei H, Thevenet J, Gruetter R, Magistretti PJ, Hirt L. Neuroprotective role of lactate after cerebral ischemia. J Cereb Blood Flow Metab. 2009;29:1780–9.

281. Maus M, Marin P, Israël M, Glowinski J, Prémont J. Pyruvate and lactate protect striatal neurons against N-methyl-D-aspartate-induced neurotoxicity. Eur J Neurosci. 1999;11(9):3215–24.

282. Zlotnik A, Sinelnikov I, Gruenbaum BF, Gruenbaum SE, Dubilet M, Dubilet E, et al. Effect of Glutamate and Blood Glutamate Scavengers Oxaloacetate and Pyruvate on Neurological Outcome and Pathohistology of the Hippocampus after Traumatic Brain Injury in Rats. Anesthesiology. 2012;116(1):73–83.

283. Ying W, Chen Y, Alano CC, Swanson RA. Tricarboxylic Acid Cycle Substrates Prevent PARP-Mediated Death of Neurons and Astrocytes. J Cereb blood flow Metab. 2002;22:774–9.

284. Zilberter Y, Gubkina O, Ivanov AI. A unique array of neuroprotective effects of pyruvate in neuropathology. Front Neurosci. 2015;9(17):1–5.

285. Suh SW, Aoyama K, Chen Y, Garnier P, Matsumori Y, Gum E, et al. Hypoglycemic Neuronal Death and Cognitive Impairment Are Prevented by Poly(ADP-Ribose) Polymerase Inhibitors Administered after Hypoglycemia. J Neurosci. 2003;23(33):10681–90.

286. Moroni F, Chiarugi A. Post-ischemic brain damage: Targeting PARP-1 within the ischemic neurovascular units as a realistic avenue to stroke treatment. FEBS J. 2009;276:36–45.

287. Yang R, Zhu S, Tonnessen TI. Ethyl pyruvate is a novel anti-inflammatory agent to treat multiple inflammatory organ injuries. J Inflamm. 2016;13(37):1–11.

288. Koivisto H, Leinonen H, Puurula M, Hafez HS, Barrera GA, Stridh MH, et al. Chronic Pyruvate Supplementation Increases Exploratory Activity and Brain Energy Reserves in Young and Middle-Aged Mice. Front Aging Neurosci. 2016;8:1–14.

289. Frank D, Kuts R, Tsenter P, Gruenbaum BF, Grinshpun Y, Zvenigorodsky V, et al. The effect of pyruvate on the development and progression of post-stroke depression: A new therapeutic approach. Neuropharmacology. 2019;155:173–84.

290. Popova I, Malkov A, Ivanov AI, Samokhina E, Buldakova S, Gubkina O, et al. Metabolic correction by pyruvate halts acquired epilepsy in multiple rodent models. Neurobiol Dis. 2017;106:244–54.

291. Kong Y, Van Bergen N, Bui B, Chrysostomou V, Vingrys AJ, Trounce IA, et al. Impact of aging and diet restriction on retinal function during and after acute intraocular pressure injury. Neurobiol Aging. 2012;33:1126.e15-1126.e25.

292. Moreno M, Campanelli J, Sande P, Sáenz DA, Sarmiento M, Rosenstein RE. Retinal oxidative stress induced by high intraocular pressure. Free Radic Biol Med. 2004;37(6):803–12.

293. Ferreira SM, Lerner SF, Brunzini R, Reides CG, Evelson PA, Llesuy SF. Time Course

Changes of Oxidative Stress Markers in a Rat Experimental Glaucoma Model. Invest Ophthalmol Vis Sci. 2010 Sep;51(9):4635–40.

294. Ko M-L, Peng P-H, Ma M-C, Ritch R, Chen C-F, Kong S, et al. Dynamic changes in reactive oxygen species and antioxidant levels in retinas in experimental glaucoma. Free Radic Biol Med. 2005;39:365–73.

295. Tezel G, Yang X, Cai J. Proteomic Identification of Oxidatively Modified Retinal Proteins in a Chronic Pressure-Induced Rat Model of Glaucoma. Invest Ophthalmol Vis Sci. 2005;46(9):3177–87.

296. Inman DM, Harun-Or-Rashid M. Metabolic Vulnerability in the Neurodegenerative Disease Glaucoma. Front Neurosci. 2017;11(146):1–19.

297. Lambert WS, Carlson BJ, Formichella CR, Sappington RM, Ahlem C, Calkins DJ. Oral Delivery of a Synthetic Sterol Reduces Axonopathy and Inflammation in a Rodent Model of Glaucoma. Front Neurosci. 2017;11:1–21.

298. Marina N, Bull ND, Martin KR. A semiautomated targeted sampling method to assess optic nerve axonal loss in a rat model of glaucoma. Nat Protoc. 2010;5(10):1642–51.

299. Chauhan BC, LeVatte TL, Garnier KL, Tremblay F, Pang IH, Clark AF, et al. Semiquantitative optic nerve grading scheme for determining axonal loss in experimental optic neuropathy. Invest Ophthalmol Vis Sci. 2006;47(2):634–40.

300. Cepurna WO, Kayton RJ, Johnson EC, Morrison JC. Age related optic nerve axonal loss in adult Brown Norway rats. Exp Eye Res. 2005;80:877–84.

301. Soto I, Pease ME, Son JL, Shi X, Quigley HA, Marsh-Armstrong N. Retinal Ganglion Cell Loss in a Rat Ocular Hypertension Model Is Sectorial and Involves Early Optic Nerve Axon Loss. Invest Ophthalmol Vis Sci. 2011;52(1):434–41.

302. Banitt MR, Ventura LM, Feuer WJ, Savatovsky E, Luna G, Shif O, et al. Progressive Loss of Retinal Ganglion Cell Function Precedes Structural Loss by Several Years in

Glaucoma Suspects. Invest Ophthalmol Vis Sci. 2013;54(3):2346–52.

303. Ventura LM, Sorokac N, Santos RDL, Feuer WJ, Porciatti V. The Relationship between Retinal Ganglion Cell Function and Retinal Nerve Fiber Thickness in Early Glaucoma. Invest Ophthalmol Vis Sci. 2006;47(9):3904–11.

304. Saleh M, Nagaraju M, Porciatti V. Longitudinal Evaluation of Retinal Ganglion Cell Function and IOP in the DBA/2J Mouse Model of Glaucoma. Invest Ophthalmol Vis Sci. 2007;48(10):4564–72.

305. Crowston J, Fahy E, Fry L, Trounce I, Van Wijngaarden P, Petrou S, et al. Targeting retinal ganglion cell recovery. Eye. 2017;31.

306. Porciatti V. Electrophysiological assessment of retinal ganglion cell function. Exp Eye Res . 2015;141:164–70.

307. Holcombe DJ, Lengefeld N, Gole GA, Barnett NL. Selective inner retinal dysfunction precedes ganglion cell loss in a mouse glaucoma model. Br J Ophthalmol. 2008;92:683–8.

308. Saszik SM, Robson JG, Frishman LJ. The scotopic threshold response of the dark-adapted electroretinogram of the mouse. J Physiol. 2002;543(3):899–916.

309. Bui B V, Fortune B. Ganglion cell contributions to the rat full-field electroretinogram. J Physiol. 2003;555(1):153–73.

310. Frishman LJ, Shen FF, Du L, Robson JG, Harwerth RS, Smith EL, et al. The scotopic electroretinogram of macaque after retinal ganglion cell loss from experimental glaucoma. Invest Ophthalmol Vis Sci. 1996;37(1):125–41.

311. Wilsey LJ, Fortune B. Electroretinography in glaucoma diagnosis. Curr Opin Ophthalmol. 2016;27(2):118–24.

312. Porciatti V, Saleh M, Nagaraju M. The Pattern Electroretinogram as a Tool to Monitor Progressive Retinal Ganglion Cell Dysfunction in the DBA/2J Mouse Model of

Glaucoma. Invest Ophthalmol Vis Sci. 2007;48(2):745–51.

313. Ventura LM, Porciatti V, Bascom F. Restoration of Retinal Ganglion Cell Function in Early Glaucoma after Intraocular Pressure Reduction A Pilot Study. Ophthalmology. 2005;112:20–7.

314. Sehi M, Grewal DS, Goodkin ML, Greenfield DS. Reversal of Retinal Ganglion Cell Dysfunction after Surgical Reduction of Intraocular Pressure. Ophthalmology. 2010;117(12):2329–36.

315. Ventura LM, Feuer WJ, Porciatti V. Progressive Loss of Retinal Ganglion Cell Function Is Hindered with IOP-Lowering Treatment in Early Glaucoma. Invest Ophthalmol Vis Sci. 2012;53(2):659–63.

316. Ryu JK, Choi HB, McLarnon JG. Combined minocycline plus pyruvate treatment enhances effects of each agent to inhibit inflammation, oxidative damage, and neuronal loss in an excitotoxic animal model of Huntington's disease. Neuroscience. 2006;141(4):1835–48.

317. Rong Z, Pan R, Chang L, Lee W. Combination treatment with ethyl pyruvate and IGF-I exerts neuroprotective effects against brain injury in a rat model of neonatal hypoxic-ischemic encephalopathy. Int J Mol Med. 2015;36(1):195–203.

318. Lee D, Shim MS, Kim K-Y, Noh YH, Kim H, Kim SY, et al. Coenzyme Q10 Inhibits Glutamate Excitotoxicity and Oxidative Stress–Mediated Mitochondrial Alteration in a Mouse Model of Glaucoma. Invest Ophthalmol Vis Sci. 2014;55:993–1005.

319. Noh YH, Kim K-Y, Shim MS, Choi S-H, Choi S, Ellisman MH, et al. Inhibition of oxidative stress by coenzyme Q10 increases mitochondrial mass and improves bioenergetic function in optic nerve head astrocytes. Cell Death Dis. 2013;4:1–12.

320. Nakajima Y, Inokuchi Y, Nishi M, Shimazawa M, Otsubo K, Hara H. Coenzyme Q 10 protects retinal cells against oxidative stress in vitro and in vivo. Brain Res .

2008;1226:226–33.

321. Müller T, Büttner T, Gholipour A-F, Kuhn W. Coenzyme Q 10 supplementation provides mild symptomatic benefit in patients with Parkinson's disease. Neurosci Lett. 2003;341:201–4.

322. Yang L, Calingasan NY, Wille EJ, Cormier K, Smith K, Ferrante RJ, et al. Combination therapy with Coenzyme Q and creatine produces additive neuroprotective effects in models of Parkinson's and Huntington's Diseases. J Neurochem. 2009;109:1427–39.

323. Malcon C, Kaddurah-Daouk R, Flint Beal M. Neuroprotective effects of creatine administration against NMDA and malonate toxicity. Brain Res. 2000;860:195–8.

324. Scheff SW, Dhillon HS. Creatine-Enhanced Diet Alters Levels of Lactate and Free Fatty Acids After Experimental Brain Injury. Neurochem Res. 2004;29(2):469–79.

325. Adcock KH, Nedelcu J, Loenneker T, Martin E, Wallimann T, Wagner BP. Neuroprotection of Creatine Supplementation in Neonatal Rats with Transient Cerebral Hypoxia-Ischemia. Dev Neurosci. 2002;24(5):382–8.

326. Lensman M, Korzhevskii DE, Mourovets VO, Kostkin VB, Izvarina N, Perasso L, et al. Intracerebroventricular administration of creatine protects against damage by global cerebral ischemia in rat. Brain Res. 2006;1114(1):187–94.

327. R: A language and environment for statistical computing. Vienna, Austria: R Foundation for Statistical Computing; 2015.

328. Diggle P, Heagerty P, Liang K, Zeger S. Analysis of longitudinal data: Oxford Statistical Science Series. Second Edition. Oxford, UK: Oxford University Press; 2002.

329. Donohue MC, Gamst AC, Edland SD. Longpower: Power and sample size calculators for linear mixed models. 2016.